Reliability Assessment of Electronics Under Drop-Impact Using Cohesive Zone and XFEM Models

by

Mandar Nilkanth Kulkarni

A thesis submitted to the Graduate Faculty of
Auburn University
in partial fulfillment of the
Requirements for the Degree of
Master of Science

Auburn, Alabama
August 6, 2011

Keywords: XFEM, cohesive, line spring, drop, shock, SIF, reliability, Pb-free, solder, Electronic Packaging

Approved by

Pradeep Lall, Chair, Thomas Walter Professor of Mechanical Engineering
George T. Flowers, Professor of Mechanical Engineering
Barton C. Prorok, Associate Professor of Materials Engineering

Abstract

The evolution of complexity in the handheld portable electronics accompanied with the miniaturization due to advancement in technology has contributed to their vulnerability under shock and drop conditions. Drop reliability of electronics has been addressed using various experimental and analytical techniques. Material characterization of Pb-free alloys at high strain rates typical of drop and shock is performed using these techniques. These transient dynamic phenomenons are addressed using advanced finite element methods such as extended finite element method, cohesive zone modeling and line spring element method to model crack/flaw initiation and propagation. The transient dynamic behavior of leadfree and leaded solder-interconnects have been studied in ball-grid array, copper-reinforced solder column and high lead column package architectures. Four interconnect types have been modeled using XFEM including Sn3Ag0.5Cu, 90Pb10Sn, Cu-Reinforced column, and 63Sn37Pb interconnects on ceramic ball-grid arrays. In addition, Sn3Ag0.5Cu on plastic ball-grid arrays has also been modeled. Extended finite element models have been correlated with cohesive-zone models along with experimental results. The board assemblies have been tested at 1,500g and 12,500g. The failed assemblies have been cross-sectioned and the failure modes correlated with model predictions. The predicted failure modes for all four interconnect types correlate well with the observed locations for failure. In an initial part of this thesis, damage and

life prediction of transient dynamics in electronics interconnects is presented using XFEM in conjunction with digital image correlation and explicit submodeling.

The second part of this thesis deals with measurement of fracture properties of Pb-free alloys at high strain rate conditions using FE modeling techniques. For this purpose, bimaterial and single material copper-solder specimens are tested using uniaxial tensile testing machine. Models for crack/flaw initiation and propagation are developed using Line spring method and extended finite element method (XFEM). Critical stress intensity factor for leadfree alloys such as Sn3Ag0.5Cu and Sn1Ag0.5Cu are extracted from line spring models. Stress intensity factor at Copper pad and bulk solder interface is also evaluated in ball grid array packages. Specimens are tested at various strain rates and events are monitored using high speed data acquisition system as well as high speed cameras operating more than 50,000 fps. In this work, fracture properties such as SIF and J integral are measured using simulation techniques and correlated with experimental results. The solder deformation and damage thresholds at the copper-solder interface have been measured at strain-rates representative of shock and vibration. These high strain rate properties of solder alloys are used to define the material models in all finite element simulations which run based on a technique of node based sub-modeling.

Acknowledgments

I would like to express my deep gratitude to my research advisor Dr. Pradeep Lall for giving me the opportunity to work under his guidance and mentorship at the NSF Center for Advanced Vehicle and Extreme Environment Electronics ($CAVE^3$) as a Graduate Research Assistant at Auburn University. I would also like to thank my other committee members, Dr. George T. Flowers and Dr. Barton C. Prorok, for their support and guidance while completing this thesis.

I would like to thank my parents, Mr. Nilkanth M. Kulkarni and Mrs. Smita N. Kulkarni, as well as my elder brother Manoj and sister in law Pallavi, for having faith in me and providing endearing love, encouragement and moral support. I would also like to thank all my friends and colleagues for their priceless friendship and support.

Table of Contents

List of Figures

List of Tables

CHAPTER 1

INTRODUCTION

1.1 Electronic Packaging

Packaging of electronic systems refers to the placement and connection of many electronic and electro-mechanical components in an enclosure which protects the system from the environment and provides easy access for routine maintenance. It is an inter-disciplinary field of study which begins at the first level where a chip is housed in its carrier and then extends to higher levels. To carry out the desired tasks with electronic systems, various mechanical aspects such as shock and vibration, thermo-mechanical deformation, reliability, cost, manufacturing, performance, thermal management, maintenance, connections, and ergonomics needs to be addressed. Analytical, experimental and numerical methods are used to assess the reliability of these electronic systems which are exposed to harsh environments such as shock, drop, and thermal loadings [Dally 2008].

There are two main types of packaging techniques: through-hole technology and surface mount technology. Through-hole technology is no longer used because of its bulkiness. The electronic industry is trying to develop smaller chips with more dense circuits that require increasing amount of power. Semiconductor technology has been generally following Moore's law. This law predicts the rate of scaling of the minimum

feature size on a semiconductor chip. With a smaller feature size, more devices and more functions can be fabricated on a specific chip for each succeeding generation of semiconductor. With this advancement there are several challenges faced by the packaging industry. Human scale peripheral devices must be able to handle numerous numbers of external input/output connections. Reduction in cross section of circuit lines increases the line resistance degrading the signal. It increases the amount of heat that must be dissipated. More advanced I/O techniques such as flip chip solder balls need to be used, which increases overall packaging cost. To deal with these issues, electronic industry has come up with surface mount technology. Figure 1 shows the schematic, depicting the evolution of electronic packaging chip carriers over the years.

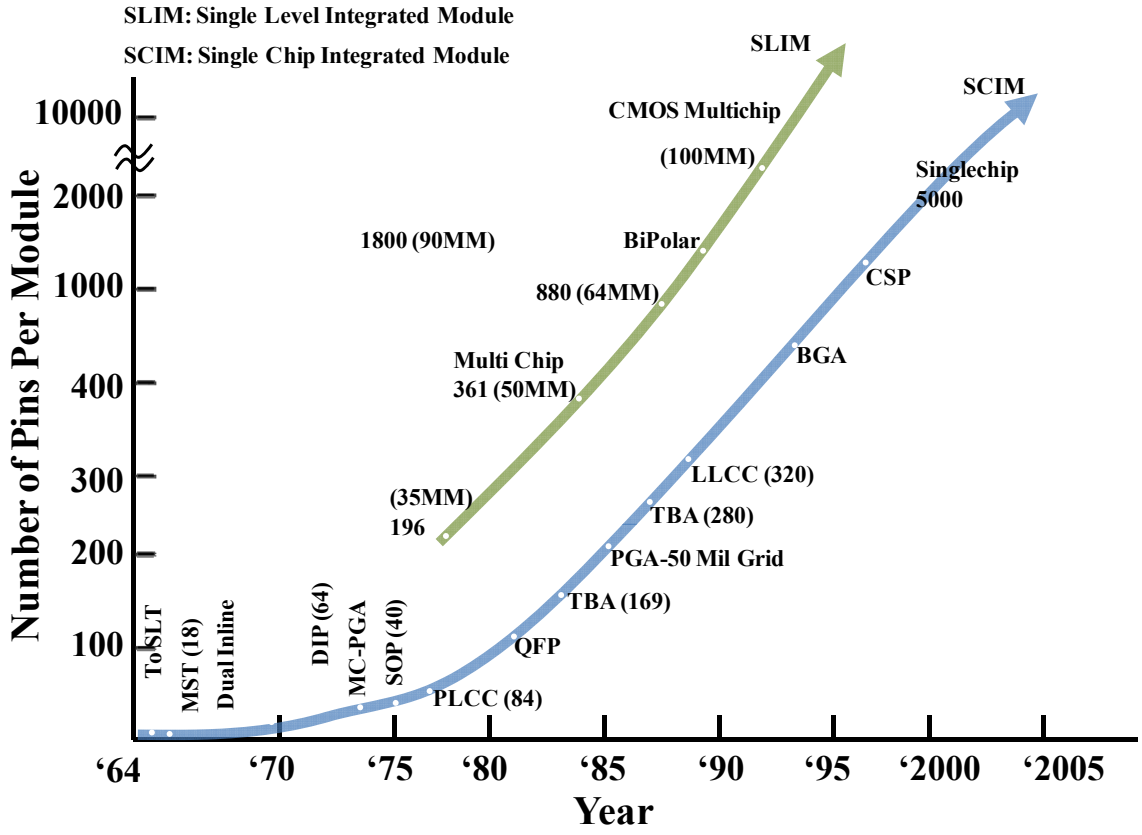

Figure 1: I/O count increasing with respect to time resulting in enhanced system performance [Dally 2008 Page #12]

There are various levels of hierarchy in the packaging of electronic systems as shown in Figure 2. A chip housed in a chip carrier comes under first level of packaging. The chip is diced from a wafer of silicon and fabricated using a photolithographic process. Several packages or chip carriers mounted on a printed wire board or substrate constitute the second level of electronic packaging. Edge connectors on PCB which are inserted into back panel contacts form third level of packaging.

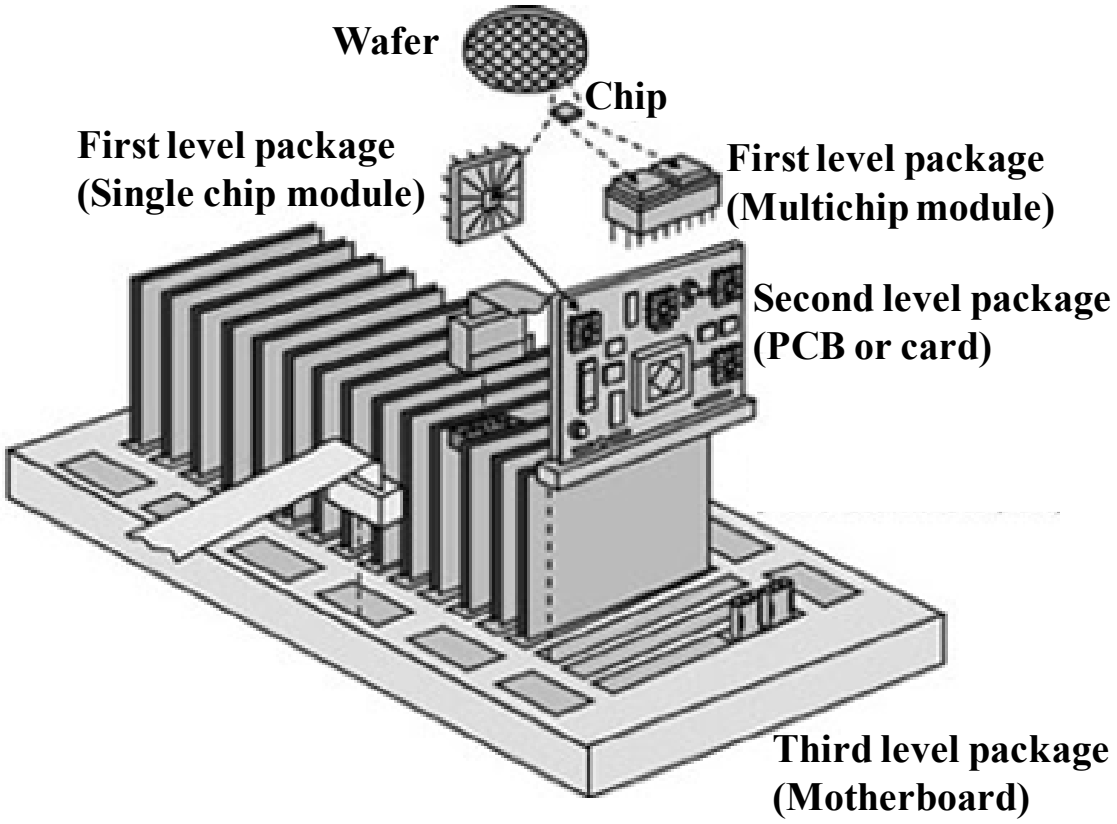

Figure 2: Electronic packaging Hierarchy [Lau 1995 Page #2]

1.2 Reliability Under Shock and Vibration

Electronic systems may be subjected to shock environments during three times in its life cycle [Dally 2008].

1. During manufacturing and assembly when the product is being transferred from one manufacturing station to another station
2. Incorrect handling of an electronic system through the distribution chain until the installation location.
3. Shock and vibration environment encountered during service of product.

Abusive handlings of electronic devices are detrimental because very high accelerations will deform or may fracture the device. Use of a shock proof box will

limit the acceleration (g-levels) and transient forces (g-loads) transmitted through the box to the product. But for hostile conditions of operation such as military applications and modern handheld consumer electronics, products are exposed to severe vibrations and shocks on repeated occasions and for longer periods of time. Therefore, a design approach in such applications to construct stiff structures which sustain dynamic loadings is specified.

During product development of microelectronic systems after completion of a prototype of a system, the product is subjected to controlled qualification testing where it is exposed to a specified shock and/or vibration environment. Failure modes investigated include solder joint failure due to fatigue, pin breakage in connectors, cable chafing and shear of bolts and pins due to shock loads. Thus, design of portable, military, automobile electronic hardware with demanding shock and/or vibration requirement is a challenging problem.

During shock, transient input results in application of time dependent velocity to the body supporting electronic device. Shock is defined as a transient condition where a single impulse of energy is transformed to a system in a short period of time with large acceleration.

1.3 Finite Element Modeling of a Shock Phenomenon

Finite element modeling approach can be used to understand the dynamic phenomenon of electronic systems. It is an effective tool which is computationally efficient and its accuracy can be verified with data obtained from actual drop tests.

Various modeling approaches have been pursued previously to address these issues, including [Dally 2008]:

1. Equivalent layer models to represent the solder joints and simulate their behavior under drop impact.
2. Solid-to-solid sub-modeling techniques to analyze BGA reliability for drop impact using half the PCB board.
3. Shell-to-solid sub-modeling using a beam-shell-based quarter symmetry model to reduce the computational time.
4. Symmetry of load and boundary conditions used to obtain computational efficiency and decrease the model size.

Transient dynamic deformation of PCBs is a wave propagation problem and hence an explicit time integration scheme can be implemented to simulate the drop phenomenon. The governing equation for a dynamic system can be expressed as:

$$[M]\{\ddot{D}\}_n + [C]\{\dot{D}\}_n + \{R^{int}\}_n = \{R^{ext}\}_n \tag{1.1}$$

For a linear problem, $\{R^{int}\}_n = [K]\{D\}_n$, where $[M]$, $[C]$ and $[K]$ are the mass, damping and stiffness matrices, respectively, and $\{D\}_n$ is the nodal displacement vector as each time step. Methods of explicit direct integration calculate the dynamic response at the time step (n+1) from the equation of motion, the central difference formulation and known conditions at one or more preceding time steps as shown below:

$$\left[\frac{1}{\Delta t^2}M + \frac{1}{2\Delta t}C\right]\{D\}_{n+1} = \{R^{ext}\}_n - \{R^{int}\}_n + \frac{2}{\Delta t^2}[M]\{D\}_n - \left[\frac{1}{\Delta t^2}M - \frac{1}{2\Delta t}C\right]\{D\}_{n-1} \tag{1.2}$$

Equation (1.1) is combined with equation (1.2) at time step n. In the implicit method, the dynamic response at time step (n+1) has been calculated from known conditions at present time step, in addition to one or more preceding time-steps.

Element size in the explicit model is limited due to the conditional stability of the explicit time integration. Explicit time integration is well suited for propagation problems that occur in the impact events, because dynamic response of the board decays within a few multiples of its longest period. It is also better suited to accommodate material and geometric nonlinearity without any global matrix manipulation. Reduced integration elements are employed in modeling of printed circuit board assemblies, because they require fewer integration points to form element stiffness matrices.

The following crack/flaw analysis techniques can be used to analyze discontinuities in finite element approach [Abaqus 2009a,b,c]:

(a) Extended Finite Element Method

(b) Cohesive Zone Modeling

(c) Line Spring Method

XFEM is an extension of the conventional finite element method based on the concept of partition of unity. It allows presence of discontinuities in finite element by adding degrees of freedom with special displacement functions. It does not require the mesh to match the geometry of crack. Material and geometric nonlinear modeling is possible with XFEM analysis. XFEM can be used with the surface based cohesive behavior approach or the virtual crack closure technique, which are best suited for modeling interfacial delamination.

Enrichment definition *ENRICHMENT is associated with the possible region of failure in the model. Only degrees of freedom in elements within these regions are potentially enriched with special functions. The region should consist of elements which are presently intersected with crack or which are likely to be intersected by crack when crack propagates. Cohesive segment and phantom node based XFEM approach in FE tool simulates crack initiation and propagation. It simulates the crack nucleation and propagation along arbitrary solution dependent path in the bulk material, since the crack propagation is not tied to the element boundaries in a mesh. The formulae and laws that govern the crack propagation analysis using XFEM technique are very similar to those used for cohesive elements with traction separation behavior. For the linear elastic traction separation model, damage initiation criteria and damage evolution laws are defined.

In Abaqus, the traction separation law assumes initially linear elastic behavior followed by the initiation and evolution of the damage. Elastic constitutive matrix is written for elastic behavior that relates the normal and shear stresses to normal and shear separations of a cracked element.

If,

t	Nominal traction stress vector
t_n	Normal component of traction
t_s and t_t	Two shear components of traction
δ_n	Normal component of separation
δ_s and δ_t	Two shear components of separation

The elastic behavior can be written as

$$t = \begin{Bmatrix} t_n \\ t_s \\ t_t \end{Bmatrix}$$

$$t = \begin{bmatrix} K_{nn} & 0 & 0 \\ 0 & K_{ss} & 0 \\ 0 & 0 & K_{tt} \end{bmatrix} \begin{Bmatrix} \delta_n \\ \delta_s \\ \delta_t \end{Bmatrix}$$

$$t = K\delta$$

K_{nn}, K_{ss} and K_{tt} are calculated based on material properties of enriched elements.

Damage modeling allows the simulation of the degradation and eventual failure of an enriched element. The failure mechanism consists of two ingredients, namely damage initiation criterion and damage evolution law. However, once a damage initiation criterion is met, damage can occur according to a user-defined damage evolution law. Figure 3 shows a typical linear traction separation response with failure mechanism.

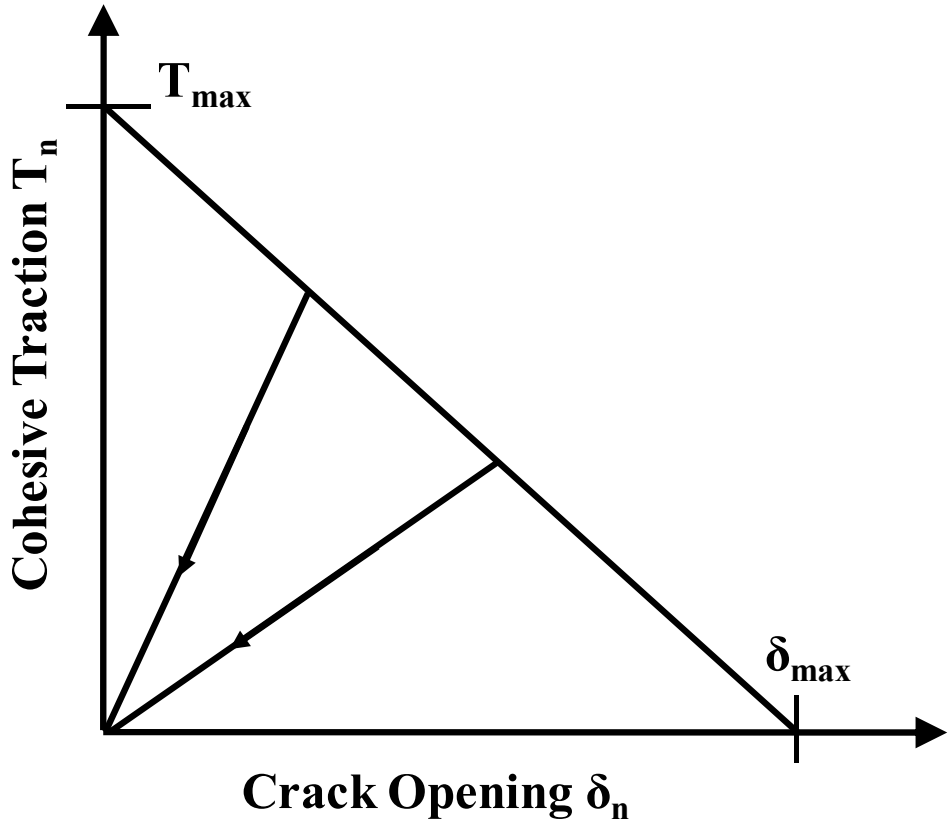

Figure 3: Typical Linear Traction Separation behavior with failure mechanism

Only first order solid continuum stress/displacement elements can be associated with the *ENRICHMENT definition. In the case of propagating cracks, these elements include bilinear plane strain and plane stress elements, linear brick elements, and linear tetrahedron elements.

In case of cohesive zone modeling, cohesive elements can be used to model the behavior of adhesive interface, interfaces in composites and other cases where integrity and strength are of importance. Cohesive zone modeling involves the following steps for model building [Abaqus 2009a]:

1. Choosing appropriate element type for a cohesive element set

2. Including these cohesive elements in the FE model and understanding typical modeling issues that arise
3. Defining the initial geometry of cohesive elements
4. Defining the mechanical properties and constitutive behavior of the cohesive elements

The constitutive response of cohesive elements requires knowledge of the specific application and involves certain assumptions about the deformation and stress state that is applicable to this specific application. In abaqus, the available constitutive responses include:

- A continuum description of the material (Continuum based constitutive model)
- A traction separation description of the interface (Constitutive model specified directly in terms of traction versus separation)
- A uniaxial stress state (Uniaxial stress based constitutive model useful in modeling gaskets and/or single adhesive patches)

In the case of macroscopic material properties, the amount of energy released to create a new surface is used for fracture analysis. Based on the traction separation law, cohesive elements model the initial loading, initiation of damage, and the propagation of damage leading to eventual failure at the bonded interface. Prior to the initiation of damage, interface behavior is described as linear elastic. Cohesive elements are modeled in areas where the cracks are expected to develop. The model need not have any crack to begin with, because as a part of solution model locates precise location where crack initiates. Cohesive zone analysis can be carried out for two dimensional, three dimensional and

axisymmetric cases. Figure 4 shows the generalized form of naming convention for cohesive element.

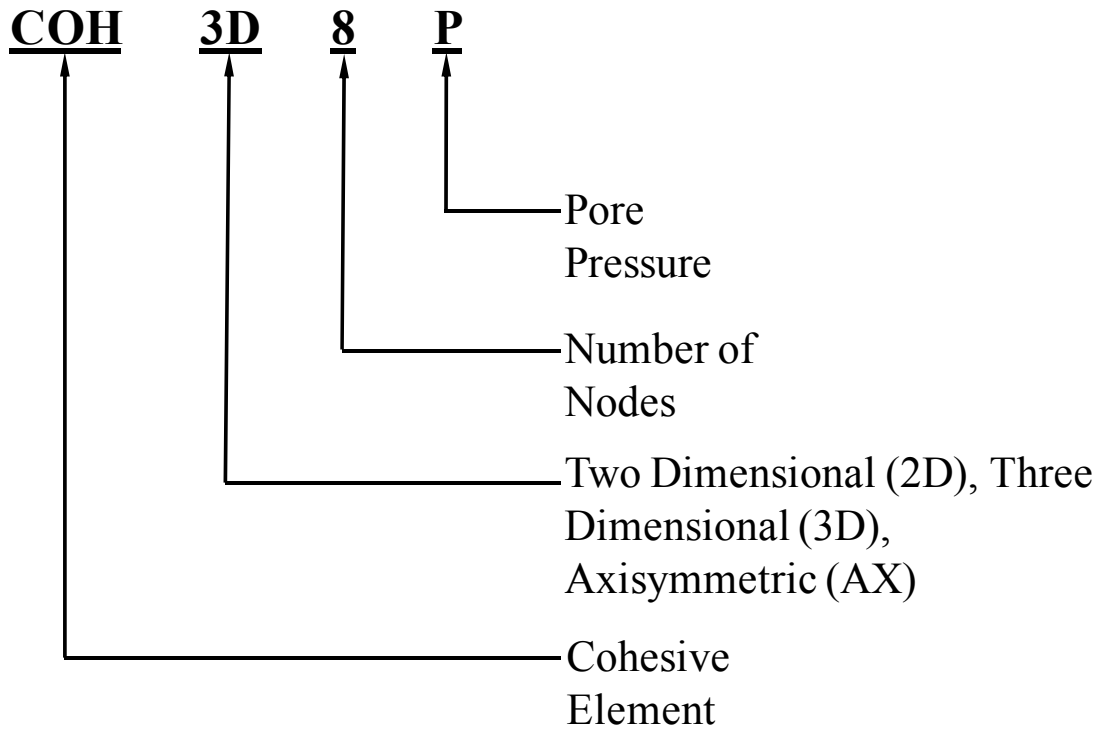

Figure 4: General form of naming convention for cohesive element

To define initial geometry of the cohesive elements, following aspects are taken into consideration:

1. The nodal connectivity of elements and position of these nodes.
2. Stack direction which identifies the top and bottom faces of cohesive elements independent of the nodal connectivity.
3. The magnitude of the initial constitutive thickness which corresponds to the geometric thickness implied by the position of nodes and stack direction or be specified directly.

Element thickness direction is important because element behavior is different in the thickness and the in-plane direction. Default thickness direction of cohesive elements is as shown in Figure 5.

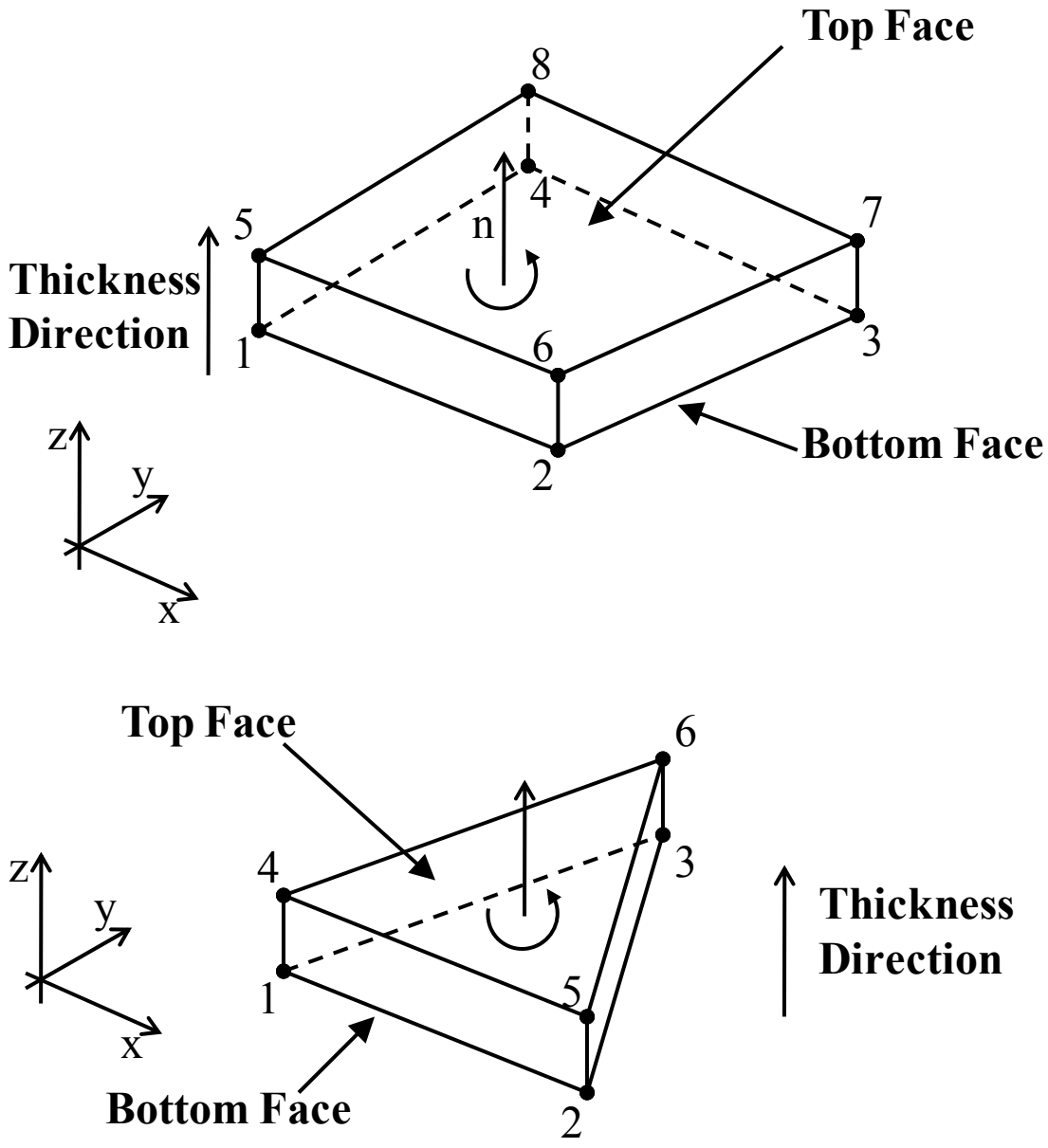

Figure 5: Thickness direction for three-dimensional cohesive elements.

Using line spring models, fracture properties such as stress intensity factor and J integral are determined. Figure 6 shows an element near the tip of a crack in an elastic

material. Each stress component is proportional to a single constant K_I. Entire stress distribution of the crack tip can be evaluated using equation given below if this single constant K_I in known. This constant is called as stress intensity factor which completely characterizes the crack-tip conditions in a material. If one assumes that the material fails locally at some critical combination of stress and strain, then it follows that fracture must occur at critical stress intensity K_{IC}. Therefore K_{IC} is an alternate measure of toughness which is s size independent material property [Anderson 2005].

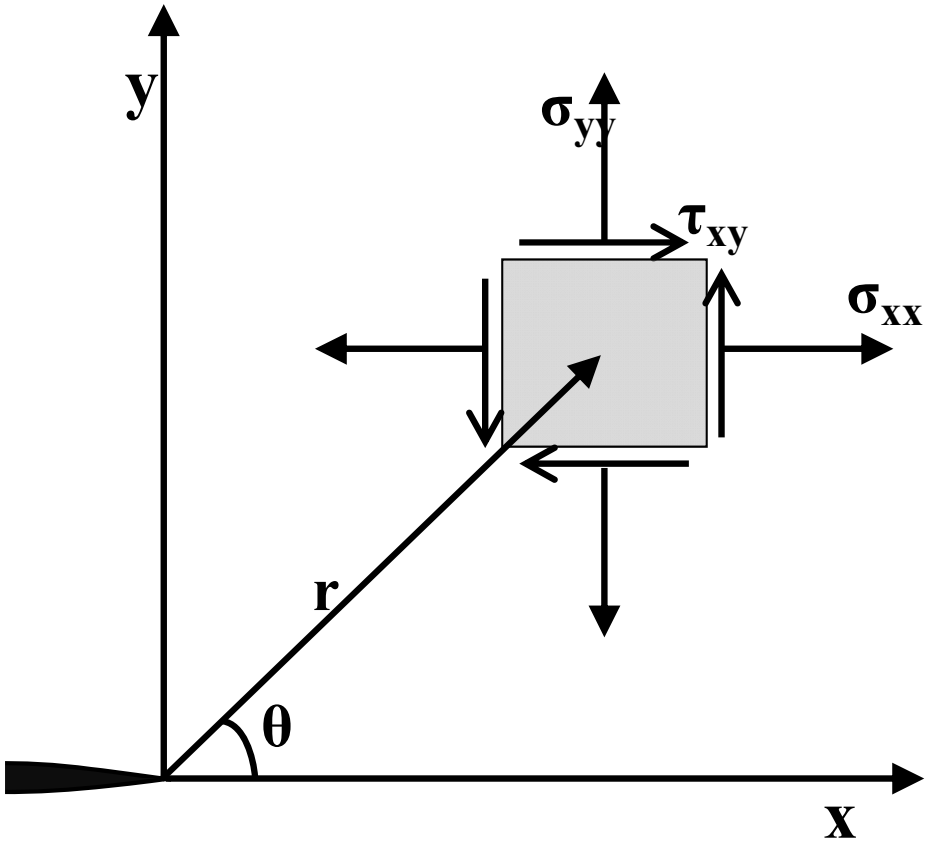

Figure 6: Element near a crack tip showing state of stress

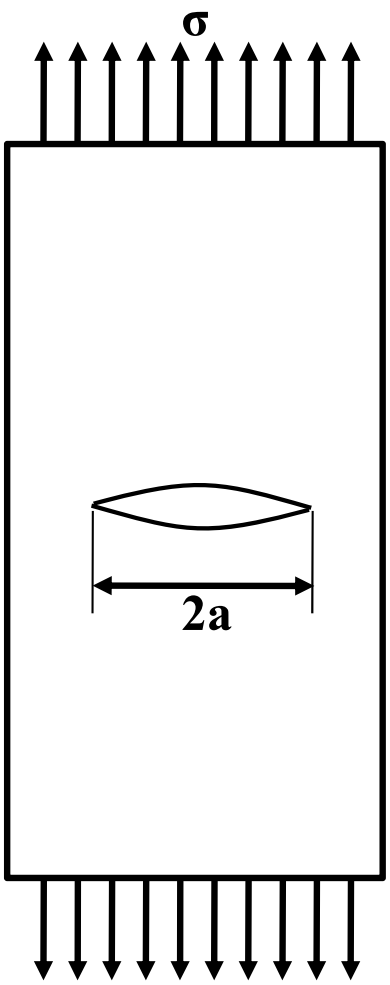

Figure 7: Crack in infinite plate subjected to a remote tensile stress

For plate as shows in Figure 7, Stress intensity factor is given by,

$$K_I = \sigma\sqrt{\pi a} \tag{1.3}$$

And stress field near the crack tip is,

$$\sigma_{xx} = \frac{K_I}{\sqrt{2\pi r}}\cos\left(\frac{\theta}{2}\right)\left[1-\sin\left(\frac{\theta}{2}\right)\sin\left(\frac{3\theta}{2}\right)\right] \tag{1.4}$$

$$\sigma_{yy} = \frac{K_I}{\sqrt{2\pi r}}\cos\left(\frac{\theta}{2}\right)\left[1+\sin\left(\frac{\theta}{2}\right)\sin\left(\frac{3\theta}{2}\right)\right] \tag{1.5}$$

$$\tau_{xy} = \frac{K_I}{\sqrt{2\pi r}}\cos\left(\frac{\theta}{2}\right)\sin\left(\frac{\theta}{2}\right)\sin\left(\frac{3\theta}{2}\right) \tag{1.6}$$

Failure occurs when $K_I=K_{IC}$. In this case, K_I is the driving force for fracture and K_{IC} is a measure of material resistance.

1.4 Thesis Layout

Chapter 1 starts with an introduction to electronic packaging stating important functions of packaging in microelectronic systems. Different types of packaging technologies are discussed with evolution from DIP to multi chip modules and grid arrays over the period of time. Shock and drop related issues are described which are addressed during entire product life cycle. Finite element techniques for global models and various advanced fracture analysis techniques for submodels are explained.

Chapter 2 encompasses literature survey on experimental and analytical methods which include FE methods used to simulate issues involved in drop and shock. Use of digital image correlation for various applications of full field strain measurements is discussed in this chapter. An overview of crack propagation models in FE such as extended finite element models, cohesive zone models has been provided. Theory and application of these methods in various other fields is explained. This chapter will give a better understanding of modeling recipes of PCB assemblies used for better computational output. IMC compound properties are very critical considering solder joint reliability. Past literature is discussed where fracture analysis of intermetallics is addressed using various test methods.

During the failure analysis and reliability assessment of electronic components, the thesis will enable (a) modeling of leadfree and advanced interconnects using sub-modeling and global modeling approach (b) identification of exact crack location in the

enrichment domain (c) evaluation of stress intensity factor and J integral at critical location of failure. Several leadfree alloys will be investigated including SnAgCu alloys.

Chapter 3 describes various crack and flaw initiation and propagation techniques used in this work for analysis of discontinuities in solder alloys during material characterization and actual drop conditions. These techniques include the extended finite element method, cohesive zone modeling and line spring method. XFEM have advantages over other fracture analysis methods including cohesive zone method as it models a crack in arbitrary solution dependent path and predicts the failure location. Line spring method introduces a local solution dominated by singularity at the crack tip which is predicted by XFEM.

Chapter 4 addresses issues of drop/shock reliability of advanced and learfree electronics using these crack propagation techniques. Three test vehicles and experimental set up of shock tower is explained in this section. Nonlinear explicit and implicit models are created for global drop analysis and substructure drop analysis of printed circuit board assemblies. Analytical FE approach is validated with actual experimental testing and failure analysis. Sectioning, polishing and microscopic analysis of interconnects show good correlation with predicted failure locations.

Chapter 5 explains the SIF and J integral measurement procedure using line spring technique. Material characterization at strain rates representative of shock and drop of electronics is carried out using tensile testing of solder alloys. Section describes the detailed procedure of bimaterial copper-solder specimen fabrication with single and double notch at interface. Simulation and experimental results of these tests at two

different strain rates at 20 /sec and 55 /sec are presented. Findings of this study from analytical FE method show good correlation with experimental output.

CHAPTER 2

LITERATURE REVIEW

Considering mechanical aspects of electronic systems, the integrity of solder joints remains most important for ensuring quality of the product. A perfect joint is the one showing complete wetting of solder to pad and this is a universal requirement that applies to surface mount as well as through-hole components. Acceptable solder joint criterions are suggested for a perfect interconnect [Woodgate 1987]. In the pursuit of device shrinkage and circuit miniaturization, surface mount technology in itself has vastly evolved over the last couple of decades.

2.1 Shock Testing for Electronics

Solder interconnects in handheld electronics are prone to accidental drops. Therefore, mechanical analysis of the devices is essential to improve their reliability against impact loadings. Standards established by JEDEC are most frequently used drop testing standards. The JEDEC standard JESD22-B111 specifies that the test vehicle should be mounted with the package side facing downwards to create a more critical loading condition [Yeh 2004]. JEDEC drop test is considered as a common ground for an assortment of semiconductor component manufacturers to compare the solder joint reliability under impact. This standard has been widely accepted and used by researchers to compare their reliability results. It also states that the drop orientation should be

horizontal or at zero degrees during the drop test. Figure 8 shows the schematic of drop test of a printed circuit assembly as per JEDEC JESD-B111. Product level drop tests are conducted on cell phones and other consumer electronics to show that angle of impact is a critical parameter in reliability of product [Liu 2005], [Seah 2002], [Lall 2006b].

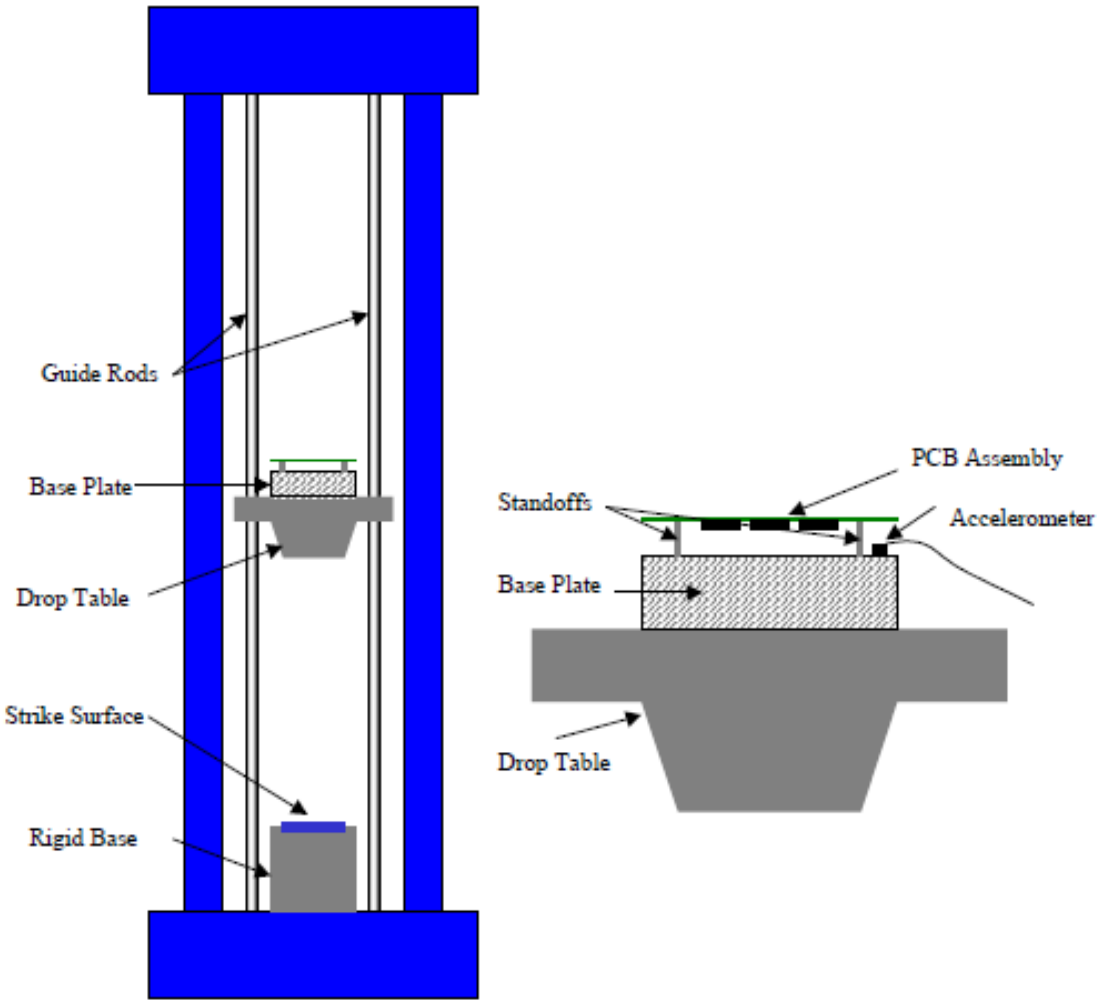

Figure 8: Typical drop test apparatus and mounting scheme for PCB assembly (Source: Board Level Drop Test Method of Components for Handheld Electronic Products JESD22-B111)

2.2 Digital Image Correlation (DIC)

In this thesis, area-array plastic and ceramic packages assembled with JEDEC form-factor printed circuit boards have been subjected to various g-loadings. Transient dynamic deformation of the board assemblies has been measured with strain gages in addition to optical measurements using high-speed cameras in conjunction with digital image correlation. DIC has been previously used to calculate full field displacement and deformation gradient in electronics [Lall 2007c, 2008b-d, 2009, Miller 2007, Park 2007a,b, 2008]. High speed imaging has been used in the measurement of impact speed, force, deformation due to shock and thermal loading. Application of high speed photography includes quantitative evaluation of in-plane deformation characteristics of geo-materials [Watanabe 2005] and assessment of local failure of bone by implementing mechanical compression testing of bone samples in medical fields [Thurner 2005].

The application of digital speckle correlation in reliability of microelectronic packages and determination of mechanical properties of polyurethane foam plastics has been studied [Lu 1998, Zhang 1999]. Other optical methods used for optical measurement in electronic include speckle photography [Smith 1993], Moiré Interferometry [Ho 1997, Wang 2002], holographic [Petrov 1996] and speckle interferometry [Cote 2001].

Previously, the feasibility of using DIC for transient strain measurement in electronic assemblies, in the presence of rigid body motion has been demonstrated [Lall 2007a-e, 2008a-d]. Digital image correlation also been used in printed circuit assemblies of mobile devices [Lall 2007, Miller 2007, Park 2007a], material characterization [Jin 2007, Park 2007b, Thompson 2007], stresses and strain in flip-chip die under thermal

loading [Kehoe 2006], stresses in solder interconnects of BGA packages under thermal loading [Zhou 2001, Yogel 2001, Zhang 2004a, Zhang 2005, Sun 2006]. In this technique, displacement field quantities are obtained by tracking a geometric point before and after deformation [Zhou 2001, Amodio 2003, Srinivasan 2005, Kehoe 2006, Lall 2007c, 2008c,d].

2.3 Finite Element Modeling for Transient Dynamic Loadings

In this work, the transient dynamic behavior of leadfree and leaded solder-interconnects has been studied in ball-grid array and copper-reinforced solder column package architectures using advanced FE techniques such as extended finite element method (XFEM) and cohesive zone modeling (CZM) for ceramic and plastic packages. Previous researchers have used various modeling methods to simulate shock and vibration including smeared property models [Lall 2004, 2005], Timoshenko beam models with conventional and continuum shell [Lall 2006a,b, 2007a-e, 2008a-d], global-local submodels [Tee 2003, Wong 2003, Zhu 2003, 2004], Implicit transient analysis with Input-G Method [Luan 2004]. [Yeh 2004] used an implicit solver by translating the input acceleration pulse into effective support excitation load on the test vehicle. Cohesive zone models are previously investigated to study failure at IMC layer [Lall 2007f, 2009].

Previously, the authors have developed explicit finite element models, cohesive-zone models, and global-local models for prediction of transient dynamics and life prediction of electronics [Lall 2004, 2005, 2006a-c, 2007a-e, 2008a-d]. Previous researchers have applied XFEM in various other fields such as concrete, composite

materials [Unger 2007, Hettich 2008]. XFEM technique has been previously used in various other applications including shock and detonation loaded thin walled structures [Cirak 2007], thin films and nanotubes [Oswald 2009]. Delamination of composites and brittle fracture in polycrystalline microstructures are studied using this enrichment approach of XFEM [Sun 2009, Sukumar 2003]. The use of XFEM to predict leadfree interconnect survivability in electronics subjected to dynamic environments is new. Finite element simulations of bimaterial copper-solder specimens under tensile testing conditions fetch fracture properties such as SIF, J integral suing line spring method.

2.4 Solder and Intermetallic Properties

Previously constitutive behavior of solder alloys has been studied under range of strain rates by use of Split Hopkinson Pressure Bar test and Double lap shear test. [Nie 2008, Ong 2004]. Leadfree stress strain curves have been plotted at low to intermediate strain rates using nano-indentation tests where elastic modulus and yield stress is measure from hardness [Xu 2008]. Intermetallic compounds of Cu_6Sn_5 and Cu_3Sn are commonly found at the interface of copper pad and solder in case of interconnects. These intermetallics affect the solder joint fatigue life and therefore the reliability of the system [Lall 2010[a], Limaye 2008]. The viscoplastic constitutive behavior of Pb-free alloy versus leaded alloy has been studied where thin layer solder joint is constructed between two copper pads on thermo-mechanical-microscale test system. Intermetallic compound characterization is carried out at low strain loading conditions [Zhang 2004]. Sn3.8Ag0.7Cu solder has been tested using tensile test and shear test at low strain loading to study formation of needle rod like Ag_3Sn intermetallics and complex intermetallic compound of $(CuAuNi)_6Sn_5$. Nickel and gold coating was provided as surface finish on

copper pads of FR4 test specimen. It was shown that mechanical properties of tensile and shear tests are highly strain rate dependent [Pang 2003]. Sn-Ag leadfree alloy system with pure copper wires is shear tested on MTS 858 MiniBionix microtester to investigate interfacial intermetallic compound. It was shown that fracture initiates and propagates within the Cu_6Sn_5 layer [Lee 2003]. Very minute size of these IMC layers in BGAs makes characterization of these compounds difficult.

Fracture analysis of IMC compound has been addressed using FE methods. [Alam 2008]. Fracture resistance of leadfree alloys has been studied at high strain rate conditions [Suha 2007]. [Lau 2002] studied crack propagation analysis of WLCSPs under thermal cycling condition. However, the use of line spring method to characterize Pb-free solder alloys for drop/shock environment is new. Mode I fracture analysis of Sn-Pb has previously been carried out to determine stress intensity factor using standard ASTM methods [Pratt 1994]. Cyclic dependent behavior of both Sn-Pb and leadfree materials has been investigated in servo-hydraulic fatigue testing machine in accord with ASTM standard test methods [Zhao 2003].

CHAPTER 3

FRACTURE ANALYSIS USING FINITE ELEMENT METHODS

3.1 Extended Finite Element Method (XFEM)

The extended finite element method was originally introduced by Belytschko and Black for solving the problems involving crack growth with minimum re-meshing [Belytschko 1999]. The method is implemented by addition of a discontinuous enrichment function to the standard approximation function using partition of unity. In classical finite element method crack tip singularity needs to be defined accurately by approximation function and discretization along the crack needs to conform the path of element edges. Remeshing of mesh topology which is done at each step affects the quality of the results and is computationally inefficient in FEM [Abdelaziz 2008]. XFEM allows the crack to propagate along an arbitrary solution dependent path with no requirement for remeshing of the mesh topology [Abaqus2009b]. The near-tip asymptotic singularity is not needed, and only the displacement jump across a cracked element is considered. For solder interconnects in portable electronics which are subjected to shock and impact conditions, additional degrees of freedom are provided to the nodes in the entire bulk corner solder because the corner interconnects are most vulnerable to failure under drop conditions [Lall 2009]. The Cohesive Segment method proposed by Remmers [2008] in conjunction with phantom nodes [Song 2006] has been used to address time

dependent dynamic fracture in the solder interconnects under a drop and shock environment. The method uses cohesive constitutive relationship to govern the debonding process enabling nucleation and growth of crack. Instead of embedding the crack tip in the bulk solder this method allows introduction of new cohesive segment when critical cohesive traction is reached. Cracks are introduced as jumps in the displacement fields. The magnitude of this jump is governed by the Cohesive Traction Separation Constitutive law. For domain with m discontinuities Γ_{dj}, with each divided into Ω_j^- and Ω_j^+ [Remmers 2008] (Figure 9),

$$\Omega_j^- \cup \Omega_j^+ = \Omega \forall j = 1,2....m$$

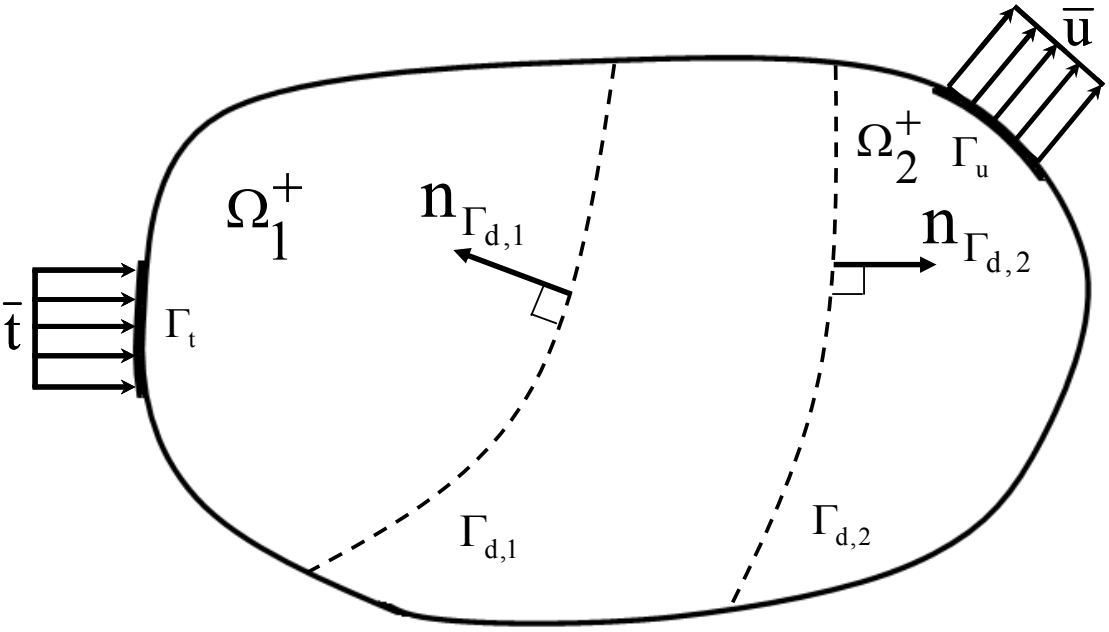

Figure 9: Multiple Cohesive Segments in enrichment domain [Remmers 2008]

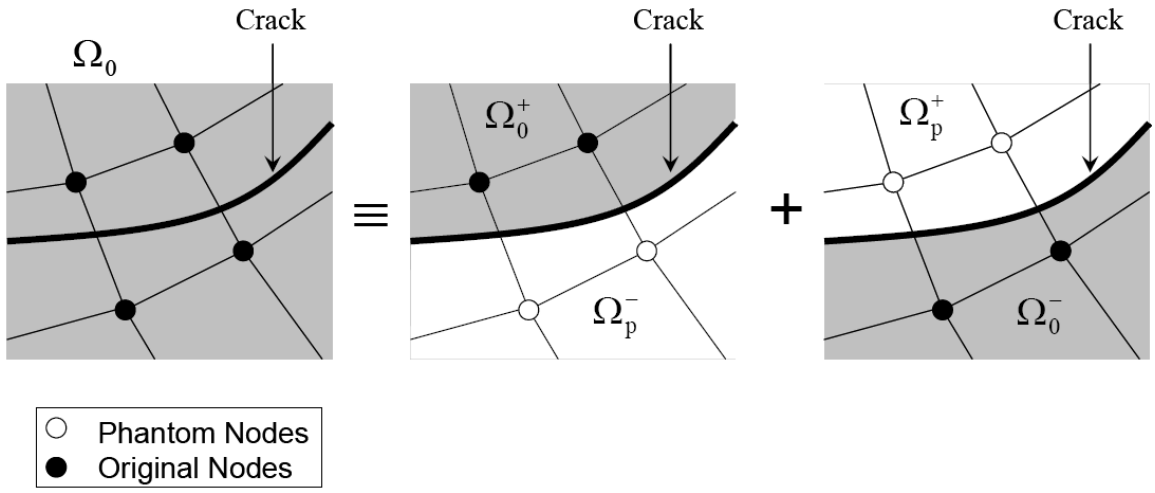

Figure 10: Phantom nodes across a discontinuity in the structure. [Song 2006, Abaqus 2009b]

Phantom nodes are superposed on the original real nodes to represent the discontinuity of the cracked elements. In an uncracked element, each phantom node is completely constrained to the corresponding real node. When the crack splits the element into two parts, each part is formed by a combination of some real and phantom nodes depending on the orientation of the crack. Each phantom node and its corresponding real node are no longer tied together and can move independantly (Figure 10) [Song 2006, Abaqus 2009b]. Displacement in the real domain is interpolated by using the degrees of freedom for the nodes in the phantom domain. The jump in the displacement field is accommodated by integrating over the area from the real nodes up to the crack. The displacement field (Equation (3.1)), strain (Equation (3.2)) and acceleration (Equation (3.3)) at material point are given by [Belytschko 1999; Daux 2000, Remmers 2008]

$$u(x,t) = \hat{u}(x,t) + \sum_{j=1}^{m} H_{\Gamma dj}(x)\tilde{u}_j(x,t) \tag{3.1}$$

$$\varepsilon(x,t) = \nabla^s \hat{u}(x,t) + \sum_{j=1}^{m} H_{\Gamma dj}(x)\nabla^s \hat{u}_j(x,t)\ x \notin \Gamma_{dj}, \tag{3.2}$$

$$\ddot{u}(x,t) = \ddot{\hat{u}}(x,t) + \sum_{j=1}^{m} H_{\Gamma dj}(x)\ddot{\tilde{u}}_j(x,t) \tag{3.3}$$

$$H_{\Gamma dj} = \begin{cases} H^+ \text{ if } x \in \Omega_j^+ \\ H^- \text{ if } x \in \Omega_j^- \end{cases} \tag{3.4}$$

where H is a jump function (heavyside, symmetric or unit symmetric), ' $\tilde{u}$ ' is continuous displacement field for 'm' additional possible discontinuities. This displacement field corresponds to the enrichment nodes in enrichment domain. $v_j(x,t) = h\tilde{u}_j(x,t)$ is magnitude of jump in displacement

$$h = H^+ - H^- \tag{3.5}$$

Thus the finite element form of the approximation field with cohesive segment approach is [Remmers 2008]:

$$u = Na + \sum_{j=1}^{m} H_{\Gamma dj} Nb_j \tag{3.6}$$

where 'a' are the regular nodal degrees of freedom, and ' b_j ' are the additional degrees of freedom associated with the discontinuity Γ_{dj}. The matrix N contains conventional finite element shape functions. Discretized acceleration is found by differentiating the differentiating the discretized displacement field:

$$\ddot{u} = N\ddot{a} + \sum_{j=1}^{m} H_{\Gamma dj} N\ddot{b}_j \tag{3.7}$$

When the stress in the element reaches the critical value, the crack nucleates and crossing the integration point extends into neighboring element. Maximum principal stress criterion is used to represent damage initiation. Damage is said to initiate when the maximum principal stress ratio shown in expression below reaches unity.

$$f = \left\{ \frac{\langle \sigma_{max} \rangle}{\sigma^{0}_{max}} \right\} \tag{3.8}$$

Crack travels until it reaches the boundaries of elements. High stresses occurred in the bulk material does not get reduced as soon as the crack is initiated. So in dynamic conditions such as drop and shock, stress in the vicinity of the crack is locally increased for small period of time and depending on the toughness of the solder material these stresses slowly fade away.

3.2 Cohesive Zone Models

Electronic products may encounter damage during shock and vibration at various interfaces including solder ball and copper pad. Damage progression is accompanied by crack initiation and propagation. Modern day portable electronic products are subjected to shock loads during handling and operation. Miniaturization of electronic components increases their vulnerability to shocks and vibration. Thus, transient dynamics of their solder joints are difficult to capture in Impact loading. This leads to the requirement of Numerical prediction of failure and crack propagation through solder interconnects. In this chapter, cohesive zone based models for prediction of crack initiation and propagation are discussed. Cohesive zone models have been previously applied to various other applications involving concrete and cement based materials, glassy polymer, steels and so on [Elices 2002]. Crack path propagation and delamination are simulated in these applications. In electronics industry this methodology has been used to determine reliability of solder interconnects subjected to thermal loadings due to temperature fluctuations [Abdul-Baqi 2005].

Let A and B be the points on the opposite faces of an interface. Nominal traction field T has both normal and tangential directional components. Consider u, t and b be three orthogonal directions. u_n denotes the separation displacement in normal direction and u_t and u_b represent opening distances in two tangential directions. When object undergoes normal loading, the u_n produced will be positive with increasing interfacial separation while negative with decreasing separation. The opening displacement at the interface be Δ_{AB}, therefore at each point on the interface [Needleman 1987]

$$u_n = n.\Delta_{AB} \qquad u_t = t.\Delta_{AB} \qquad u_b = b.\Delta_{AB} \tag{3.9}$$

And corresponding nominal traction field in u,t and b direction is given by

$$T_n = n.T \qquad T_t = t.T \qquad T_b = b.T \tag{3.10}$$

Therefore, displacement and traction vector be

$$T = \begin{Bmatrix} T_n \\ T_t \\ T_b \end{Bmatrix} \qquad u = \begin{Bmatrix} u_n \\ u_t \\ u_b \end{Bmatrix} \tag{3.11}$$

Constitutive relationship between traction and opening displacement field is described by potential function ϕ.

$$\phi(u_n, u_t, u_b) = -\int_0^u [T_n du_n + T_t du_t + T_b du_b] \tag{3.12}$$

As normal loading is applied during impact loading, the magnitude of normal traction goes high. Fracture strength of the ductile solder material goes on increasing with increase in the strain rate but that of Inter-metallic compound decreases as strain rate goes high [Lall 2007]. When the traction force reaches its maximum value, the interface separation occurs as the material loses its stiffness completely and ultimately falls to zero

causing complete interfacial separation. Relative shearing across interface leads to the development of shear traction, but the dependence of the shear traction on opening displacements in u and b directions is taken as linear. Expression for specific potential function is obtained as:

$$\phi(u_n, u_t, u_b) = \frac{27}{4}\sigma_{max}\delta\left\{\begin{array}{l}\frac{1}{2}\left(\frac{u_n}{\delta}\right)^2\left[1-\frac{4}{3}\left(\frac{u_n}{\delta}\right)+\frac{1}{2}\left(\frac{u_n}{\delta}\right)^2\right] \\ +\frac{1}{2}\alpha\left(\frac{u_t}{\delta}\right)^2\left[1-2\left(\frac{u_n}{\delta}\right)+\left(\frac{u_n}{\delta}\right)^2\right]+ \\ \frac{1}{2}\alpha\left(\frac{u_b}{\delta}\right)^2\left[1-2\left(\frac{u_n}{\delta}\right)+\left(\frac{u_n}{\delta}\right)^2\right]\end{array}\right\} \tag{3.13}$$

Here, σ_{max} is maximum traction at interface due to normal loading only. Opening displacements in b and t direction are assumed to be zero. δ is characteristic length corresponding to maximum displacement of u_n and α specifies the ratio of shear to normal stiffness of the interface. The traction forces at the interface for $u_n \le \delta$,

$$T_n = -\frac{27}{4}\sigma_{max}\left\{\begin{array}{l}\left(\frac{u_n}{\delta}\right)\left[1-2\left(\frac{u_n}{\delta}\right)+\left(\frac{u_n}{\delta}\right)^2\right]+\alpha\left(\frac{u_t}{\delta}\right)^2\left[\left(\frac{u_n}{\delta}\right)-1\right]+ \\ \alpha\left(\frac{u_b}{\delta}\right)^2\left[\left(\frac{u_n}{\delta}\right)-1\right]\end{array}\right\} \tag{3.14}$$

$$T_t = -\frac{27}{4}\sigma_{max}\left\{\alpha\left(\frac{u_t}{\delta}\right)\left[1-2\left(\frac{u_n}{\delta}\right)+\left(\frac{u_n}{\delta}\right)^2\right]\right\} \tag{3.15}$$

$$T_b = -\frac{27}{4}\sigma_{max}\left\{\alpha\left(\frac{u_b}{\delta}\right)\left[1-2\left(\frac{u_n}{\delta}\right)+\left(\frac{u_n}{\delta}\right)^2\right]\right\} \tag{3.16}$$

And when the characteristic length at interface exceeds opening displacement u_n, all traction forces go to zero.

$$T_n = 0$$

$$T_t = 0 \qquad (3.17)$$

$$T_b = 0$$

Cohesive zone methodology can be used as a leading indicator of failure and in order to study crack propagation. To define the behavior of material and the crack formation at the failure location, four different types of cohesive laws can be used as shown in Figure 11 [van den Bosch 2006].

a) Polynomial Cohesive Zone Law

b) Piece-wise linear Cohesive Zone Law

c) Exponential Cohesive Zone Law

d) Rigid-linear Cohesive Zone Law

These laws govern the constitutive relation of traction and characteristic opening length in both normal and tangential direction. Δ_n and Δ_t are opening displacements and T_n and T_t are traction forces in normal and tangential directions respectively.

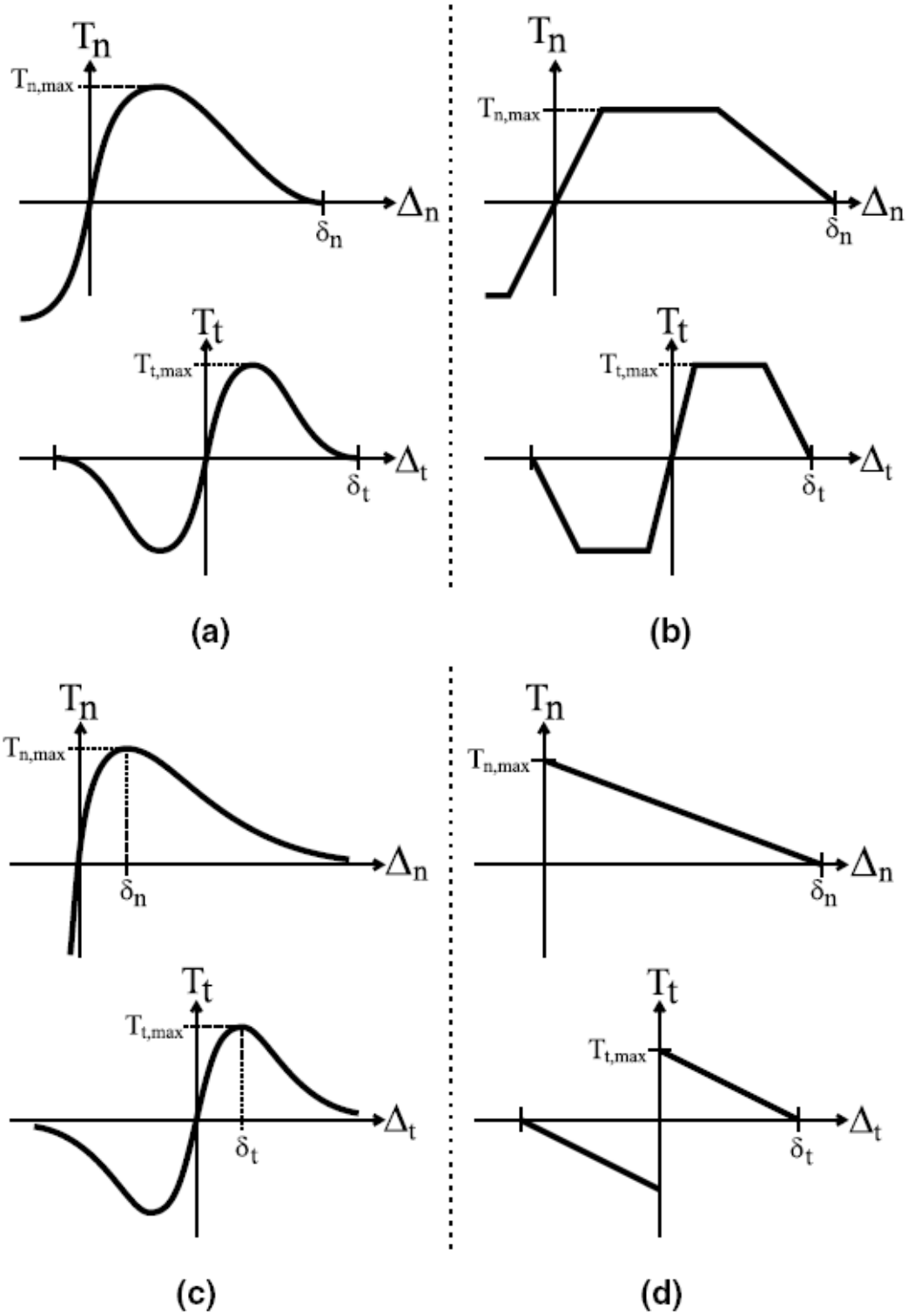

Figure 11: Four types of cohesive zone laws (a) Polynomial (b) Piece-wise Linear (c) Exponential (d) Rigid Linear

δn and δt are the characteristic openings created when the normal and tangential tractions reaches maximum values of $T_{n,max}$ and $T_{t,max}$. Characteristic behavior of materials can be coupled or uncoupled depending on the relationship between normal traction and tangential opening displacement or tangential traction and normal opening displacement. For uncoupled cohesive law, normal traction force T_n is independent of tangential displacement Δ_t and the tangential traction force, T_t does not depend on normal displacement, Δ_n in the direction of applied impact loading. In case of coupled cohesive zone law, both displacement openings are controlled by both traction forces. The areas under tractions versus corresponding opening displacement curves physically represent separation work φn and φt [van den Bosch 2006].

In uncoupled cohesive law, the failure is dominated by either normal loading or tangential loading. During drop event with JEDEC orientation, failure of the solder interconnect occurs mainly due to the normal loading caused by the shock wave. Normal traction T_n mainly produces the normal opening displacement Δ_n. Debonding of the surfaces occurs thus due to Uncoupled cohesive zone law.

For polynomial cohesive law, the partial coupling between normal and tangential direction is produced either by use of effective opening displacement and/or some coupling parameter (α). The general expression of effective opening parameter is given by

$$\lambda = \sqrt{\left(\frac{\Delta_n}{\delta_n}\right)^2 + \left(\frac{\Delta_t}{\delta_t}\right)^2} \qquad (3.18)$$

And the tractions in normal and tangential directions are having general form,

$$T_n = T_{n,max}\frac{\Delta_n}{\delta_n} f(\lambda) \qquad T_t = T_{t,max}\frac{\Delta_t}{\delta_t} f(\lambda) = \alpha T_{n,max}\frac{\Delta_t}{\delta_t} f(\lambda) \quad (3.19)$$

Here α varies from $0 \leq 1$. When traction exceeds its maximum value, α becomes greater than 1. The piecewise linear cohesive zone law as shown in Figure 11 ((b) uses the coupling parameter α to relate the traction forces. The curve of traction versus opening displacement shows the trapezoidal shape with middle flat region. In bilinear curve middle region is not present as proposed by [Geubelle 1998].

q and r are the two parameters which control the exponential cohesive law proposed by Xu and Needleman. Normal and tangential tractions are functions of both normal and tangential opening displacements.

$$T_n = T_n(\Delta_n, \Delta_t) \qquad (3.20)$$

And in the same way,

$$T_t = T_t(\Delta_n, \Delta_t) \qquad (3.21)$$

$$\text{And} \quad q = \frac{\phi_t}{\phi_n} \qquad (3.22)$$

The expressions for both tractions are given as:

$$T_n = \frac{\phi_n}{\delta_n}\exp\left(-\frac{\Delta_n}{\delta_n}\right)\left\{\frac{\Delta_n}{\delta_n}\exp\left(-\frac{\Delta_t^2}{\delta_t^2}\right) + \frac{1-q}{r-1}\left[1-\exp\left(-\frac{\Delta_t^2}{\delta_t^2}\right)\right]\left[r-\frac{\Delta_n}{\delta_n}\right]\right\} \qquad (3.23)$$

$$T_t = 2\frac{\phi_n}{\delta_t}\frac{\Delta_t}{\delta_t}\left\{q+\left(\frac{r-q}{r-1}\right)\frac{\Delta_n}{\delta_n}\right\}\exp\left(-\frac{\Delta_n}{\delta_n}\right)\exp\left(-\frac{\Delta_t^2}{\delta_t^2}\right) \qquad (3.24)$$

[Falk 2001], [Rahulkumar 2000] and [Yuan 2003] have assumed the coupling parameter α as unity, while [Araki 2005],[Benzeggagh 1996],[Dollhofer 2000],[Pang 1995],[Warrior 2003],[Yang 2001] have shown experimentally that potential energy

functions for normal and tangential directions are not equal. Several other authors have altered and extended the initial exponential cohesive law by Xu and Needleman.

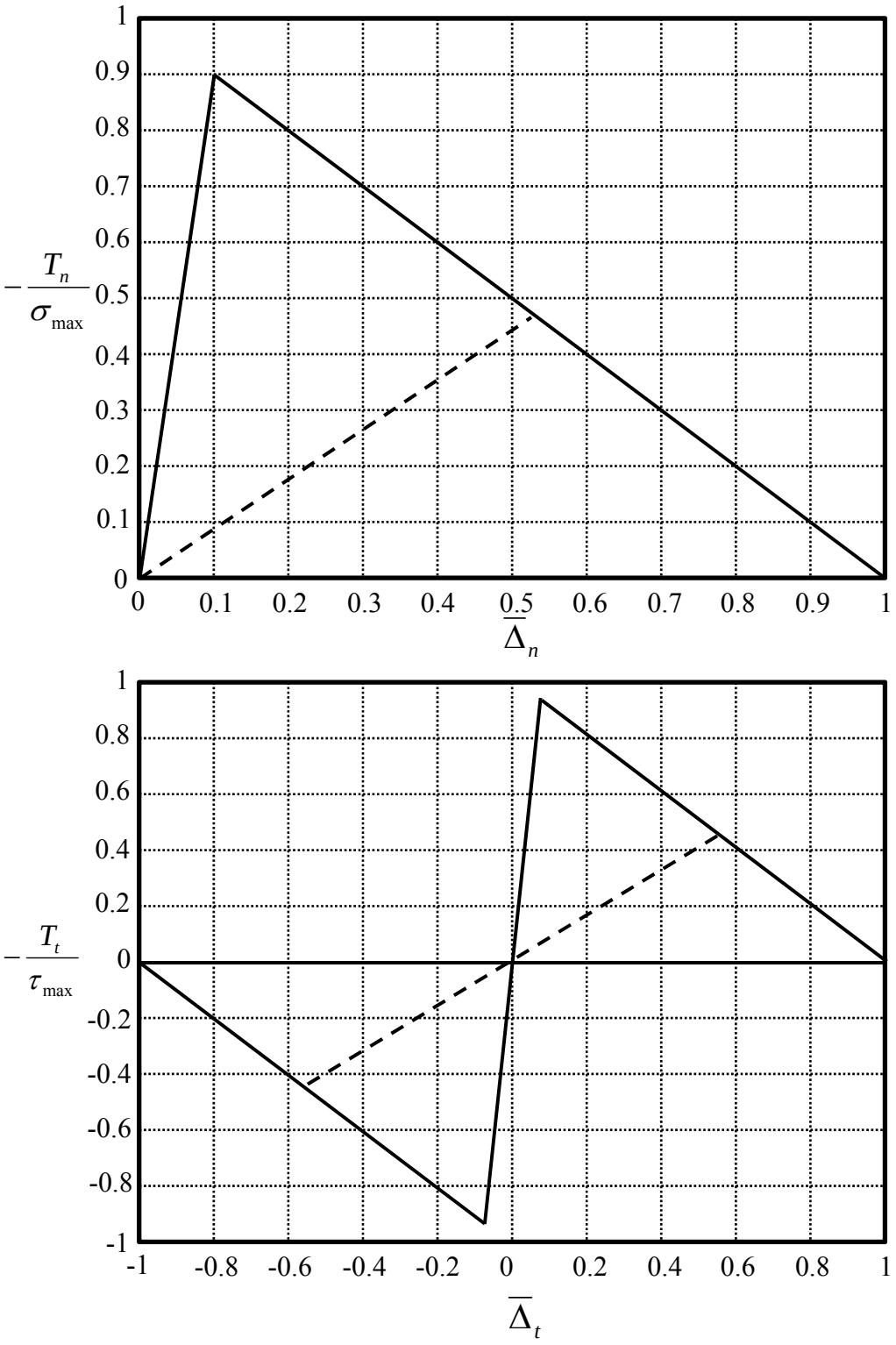

Figure 12: Quasi linear cohesive zone model in pure tension and pure shear [Falk 2001]

Bilinear cohesive zone law is shown in the above Figure 12 with linear increase followed by linear decrease in the traction. The dashed line shows the unloading and loading paths of traction. The model proposed by Xu and Needleman generates healing of the fracture surface during unloading.

In this thesis, the results from XFEM have been benchmarked against cohesive zone models to study the predicted crack propagation path. Cohesive elements have been embedded at the solder ball and copper pad interface at the component side. The constitutive behavior of the cohesive elements is characterized by the traction-separation law which accounts for the amount of the energy required to create new surface or an interfacial crack. The CZM model simulates the initial loading, damage initiation, damage propagation of the crack at the layer between solder ball and copper pad leading to eventual failure. Progression of the stiffness degradation variable to unity causes failure of interconnects. The cohesive elements have been modeled to possess linear elastic traction and separation behavior, as shown in Figure 13.

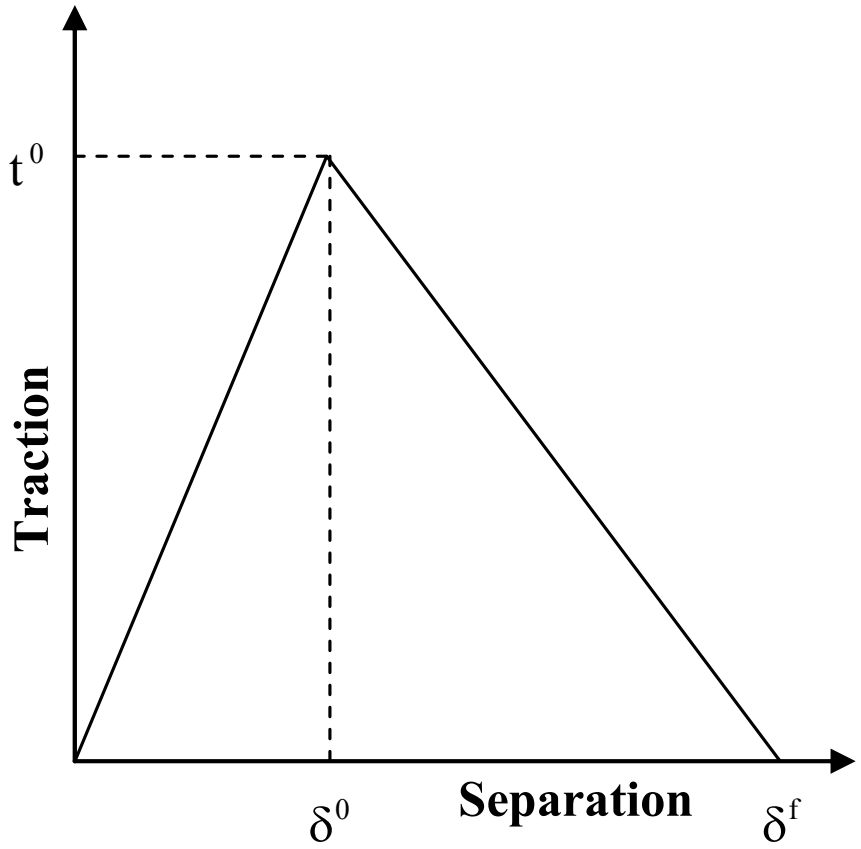

Figure 13: Linear Traction-Separation response for cohesive elements

Softening behavior of cohesive zone after the damage initiation has been prescribed using the damage evolution law. Maximum nominal stress criterion is used to identify the locations for damage initiation:

$$\max\left\{\frac{\langle t_n \rangle}{t_n^0}, \frac{t_s}{t_s^0}, \frac{t_t}{t_t^0}\right\} = 1 \qquad (3.25)$$

where t_n, t_s and t_t are the peak values of the nominal stress. The evolution of damage under a combination of normal and shear deformations can be expressed in terms of an effective displacement. Damage due to a combination of normal and shear deformations expressed in terms of δ_n, δ_s and δ_t gives the displacement.

3.3 Line Spring Models

Fracture properties of a material such as stress intensity factor and J integral can be calculated using Line spring models. Introduced by Rice and Levy [Rice 1972[a-b]], these models calculate SIFs computationally inexpensively. SIF for Pb-free alloys under high strain rate environment are measured using line spring elements attached to shell elements. Fracture properties are extracted at inter metallic component layer between bulk solder and copper in ball grid array packages. Variation of stress intensity factor at interface of Copper-Solder bimaterial specimen for different alloys under varying strain rates during tensile testing condition is plotted.

Line spring elements are modeled as one dimensional elements LS6 in a series along the flaw edge. LS6 is a 6 node general second order line spring element. This element incorporates the local solution dominated by a singularity at the crack tip into shell elements in un-cracked state. Relative displacements and rotations are calculated across this interface section of bimaterial specimen for tensile test and IMC layer for BGA drop test. These properties are used to calculate local strain field, J integral and SIF at integration points of elements. In case of high speed uniaxial tensile test, Bimaterial copper-solder specimens are seem to fail at the notched interface. The crack initiates at the root of a 30° notch and propagates along the interface of two different materials. For this reason, line spring 1D elements are inserted at this interface.

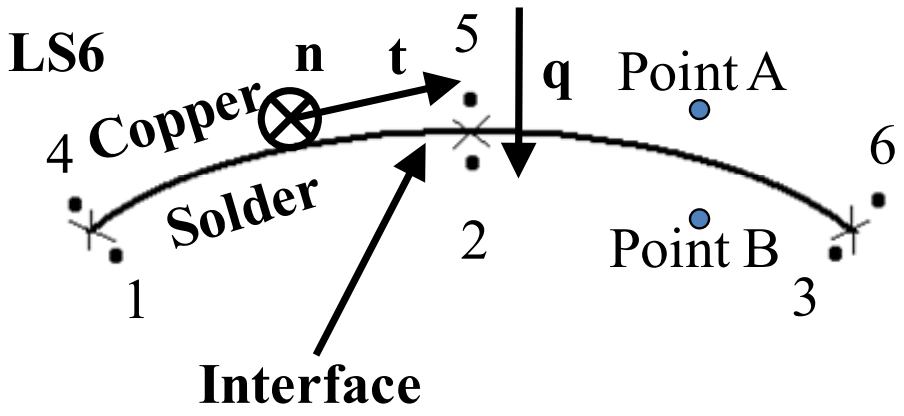

Figure 14: Line spring element LS6 node numbering

If t, n, q represent orthonormal system with t tangential to the specimen along the flaw, n as normal to the specimen surface giving q as [Gonalves 1999]

$$q = t \times n \tag{3.26}$$

Figure 14 shows line spring modeling geometry of Bimaterial copper solder specimen with a LS6 element. Node 1, 2, 3 are on solder side of the specimen and node 4, 5, 6 are on copper side. As shown in the Figure 14, point A and B are placed at the same place but on opposite side of the flaw. The relative motion between these two points can be given by three displacement and three rotation strains for mode I, II and III.

Mode 1

Opening Displacement $\Delta u_I = (u_B - u_A) \cdot q$ (3.27)

Opening Rotation $\Delta \phi_I = (\phi_B - \phi_A) \cdot t$ (3.28)

Mode 2 – Through thickness shear

Relative Displacement $\Delta u_{II} = (u_B - u_A) \cdot n$ (3.29)

Here, deformation does not take place due to relative rotation $\Delta \phi_{II} = (\phi_B - \phi_A) \cdot n$

(3.30)

Mode 3

Relative Displacement $\Delta u_{III} = (u_B - u_A) \cdot t$ (3.31)

Relative Rotation $\Delta\phi_{III} = (\phi_B - \phi_A) \cdot q$ (3.32)

The compliance equation of mode I line spring model for a single notched specimen with far field loading is given as

$$\begin{Bmatrix} u \\ \theta \end{Bmatrix} = [G] \begin{Bmatrix} N \\ M \end{Bmatrix} \tag{3.33}$$

N is axial force and M is bending moment. Energy compliance calibration gives matrix G [Tada 1973]. The compliance are obtained by modeling springs as plain strain single-edge notched specimen of width t and crack depth a, subjected to axial force N and bending moment M per unit thickness. The additional displacement δ_c and rotation θ_c at the load points due to presence of crack are given by [Gonalves 1999]

$$\begin{bmatrix} \delta_c \\ \theta_c \end{bmatrix} = \begin{bmatrix} P_{11} & P_{12} \\ P_{21} & P_{22} \end{bmatrix} \begin{bmatrix} N \\ M \end{bmatrix} \tag{3.34}$$

The matrix P can be obtained from SIF calibration of single-edge notched specimen using energy compliance relations [Rice 1972c].

$$P_{11} = \frac{2\pi(1-\nu^2)}{E}\gamma_{11} \tag{3.35}$$

$$P_{12} = P_{21} = \frac{2\pi(1-\nu^2)}{Et}\gamma_{12} \tag{3.36}$$

$$P_{22} = \frac{2\pi(1-\nu^2)}{E}\gamma_{22} \tag{3.37}$$

Therefore, at the interface stress intensity factor and J integral can be calculated by

$$K_I = \frac{(\pi a)^{1/2}}{t^2}\left[F_1\left(\frac{a}{t}\right)N_I t + F_2\left(\frac{a}{t}\right)M_I\right] \tag{3.38}$$

$$J = \frac{K_I^2}{E'} + \frac{K_{II}^2}{E'} + \frac{K_{III}^2}{2G} \tag{3.39}$$

F_1 and F_2 are approximate expressions given by [Tada 1973]. E' and υ are calculated as

$$E' = \frac{E}{(1-\nu^2)},\ G = \frac{E}{2(1+\nu)} \tag{3.40}$$

CHAPTER 4

XFEM AND CZM BASED SHOCK-RELIABILITY MODELS FOR LEADFREE AND ADVANCED INTERCONNECTS

4.1 Introduction

Electronic systems may often be subjected to drop and shock environments during manufacturing, shipping and operational conditions. The presented work helps in assessment of drop reliability of electronics in advanced and leadfree interconnects. Various experimental and finite element methods are implemented to study dynamic behavior of solder interconnects. Models for crack initiation and propagation in leadfree solder interconnects are developed. Implicit and explicit finite element methods are implemented to model non linear dynamic environment. Extended finite element method is used which enables the modeling the solder interconnect without explicitly meshing the crack surface. The crack propagated in crack domain along the solution dependent path with no requirement of remeshing the model. Interface damage properties of the copper-solder interface have been characterized at high strain rate on a bi-material specimen using high-speed imaging in conjunction with digital image correlation. Damage properties have been used as input to the XFEM models. The XFEM sub-models have been developed using node-based sub-modeling, transient displacement and velocity

histories from digital image correlation measurements with high-speed imaging of board assemblies during shock.

4.2 Test Vehicle

Three different configurations of test vehicles are used for this study. Test Board-A has ceramic packages while Test Board-B is with plastic packages. All test vehicles are daisy chained. Test Boards A and C were subjected to JEDEC standard JESD-B211 drop test. Test Board-B was subjected to 12,500g, 0.2ms pulse. Solder alloys include copper reinforced solder column grid array (CCGA), Eutectic tin lead solder (63Sn37Pb), high lead solder joint (90Pb10Sn), and SAC305 solder (Sn3Ag0.5Cu).

Table 1: Configuration A Package Architecture (Ceramic Packages)

Parameter	CCGA Solder Columns	CBGA 63Sn37Pb	CBGA (Hi-Pb Column)	CBGA Sn3Ag0.5Cu
Length (mm)	21	21	21	21
Width (mm)	21	21	21	21
Thickness (mm)	2.4	2.4	2.4	2.4
I/O	400	400	400	400
Pitch (mm)	1	1	1	1
Ball Diameter (mm)	0.6	0.6	0.6	0.6
Joint Height	2	0.6	0.6	0.6

Figure 15 shows test board A with copper reinforced solder column grid array packages. All the packages on this test board experience different strain pulse because of

the different geometric location. Figure 16 shows array configuration of the CBGA ceramic package with 400 I/Os.

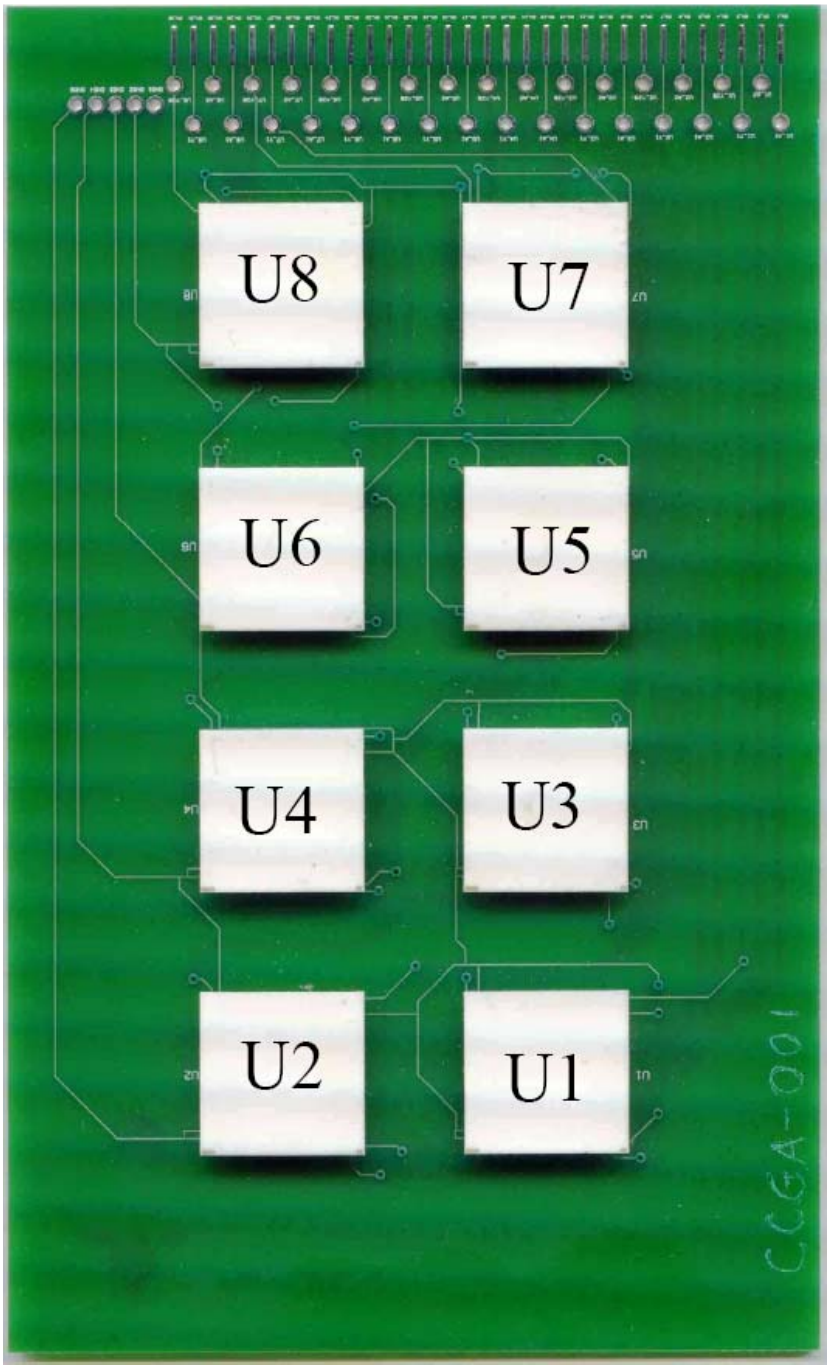

Figure 15: Configuration A Test Board (Ceramic Packages)

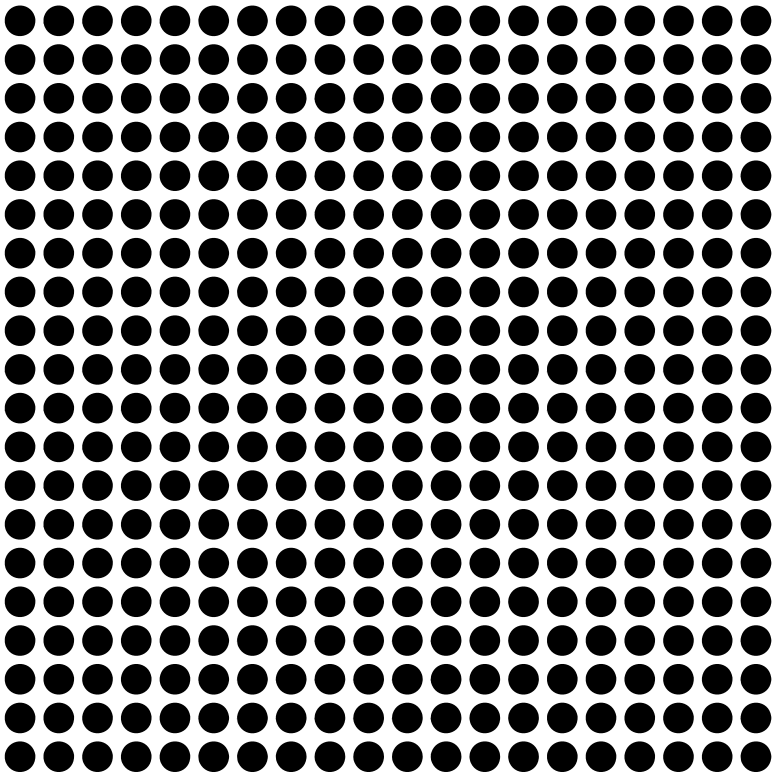

Figure 16: Interconnect array configuration for Test Board A, 400 I/O CBGA/CCGA

It has eight packages with same interconnect type on all the eight. These boards have ceramic packages with 400 I/O each. The board dimension are 106mm x173mm x 2mm. Package Architecture is shown in Table 1. Test- Board B is a single package centrally located on board designed as per JEDEC specifications with dimensions as 132mm x 77mm x 1.5mm as shown in Figure 17. Plastic package with 324 I/O is mounted on board for which array configuration is as shown in Figure 18. The solder interconnects are SAC305 solder (Sn3Ag0.5Cu).

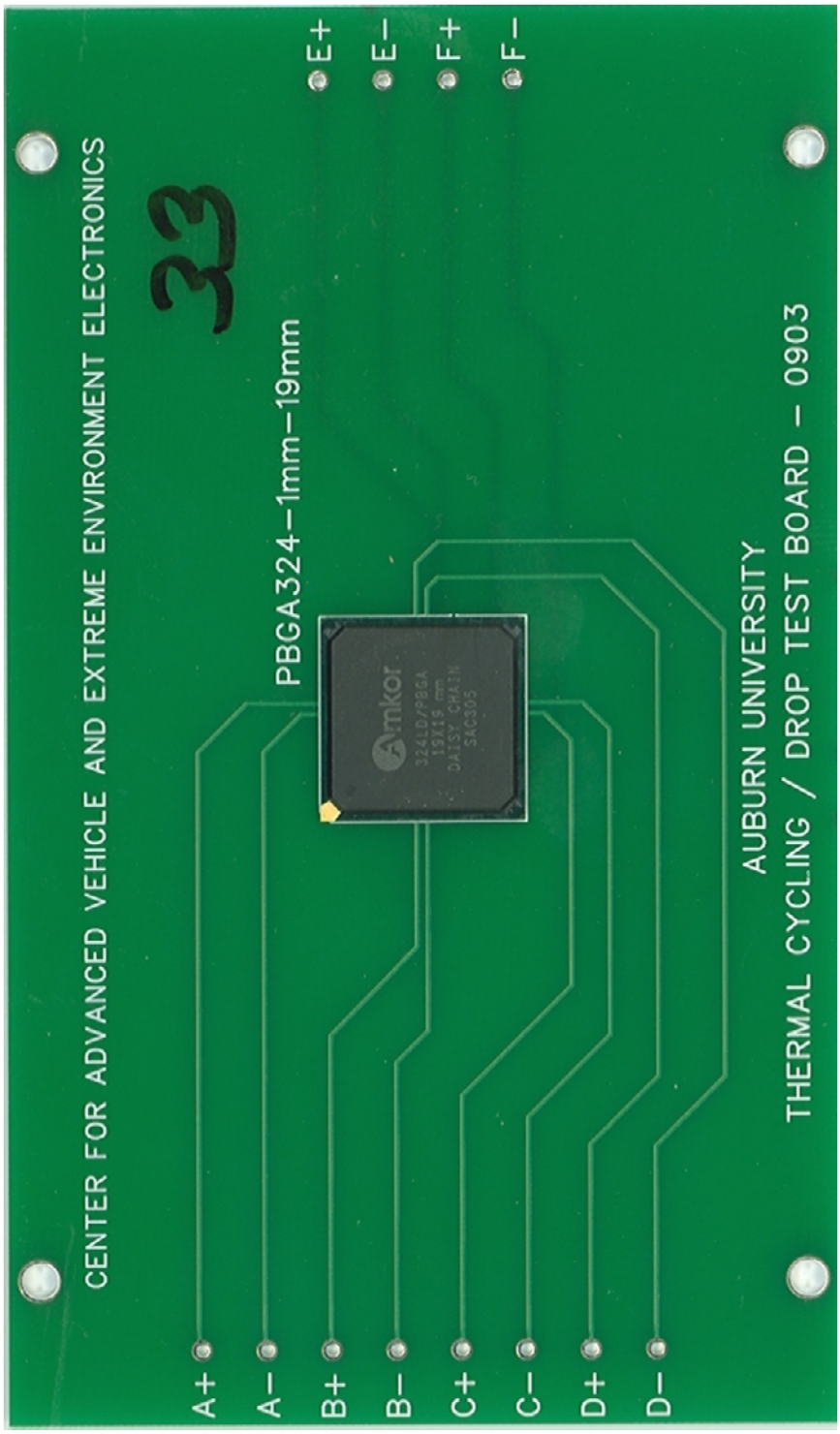

Figure 17: Configuration B Test Board (Plastic Package)

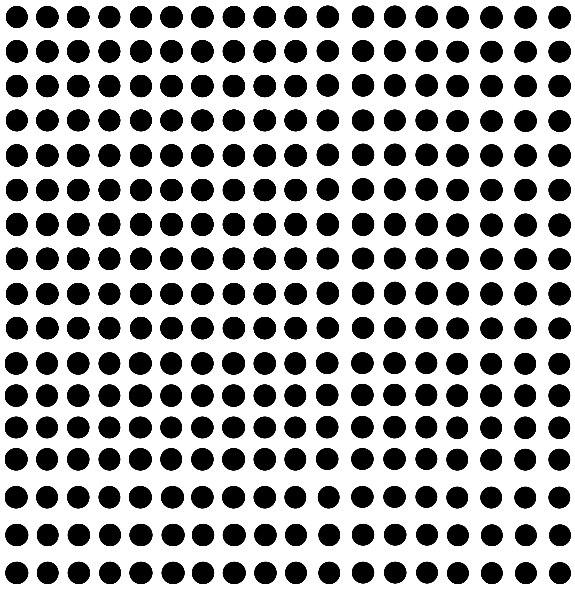

Figure 18: Interconnect array configuration for Test Board B, 324 I/O PBGA

Figure 19 shows test Board-C which is a JEDEC test board with dimensions 132mm X 77mm X 1mm. The test board has 15 chip-array ball-grid array packages (CABGA) populated on one side in a three-row, five-column format. The packages have an I/O count of 100 and pitch of 0.8mm full-array configuration as shown in Figure 20. The printed circuit board is made up of FR4-06. Package architecture of test board B and C are shown in Table 2.

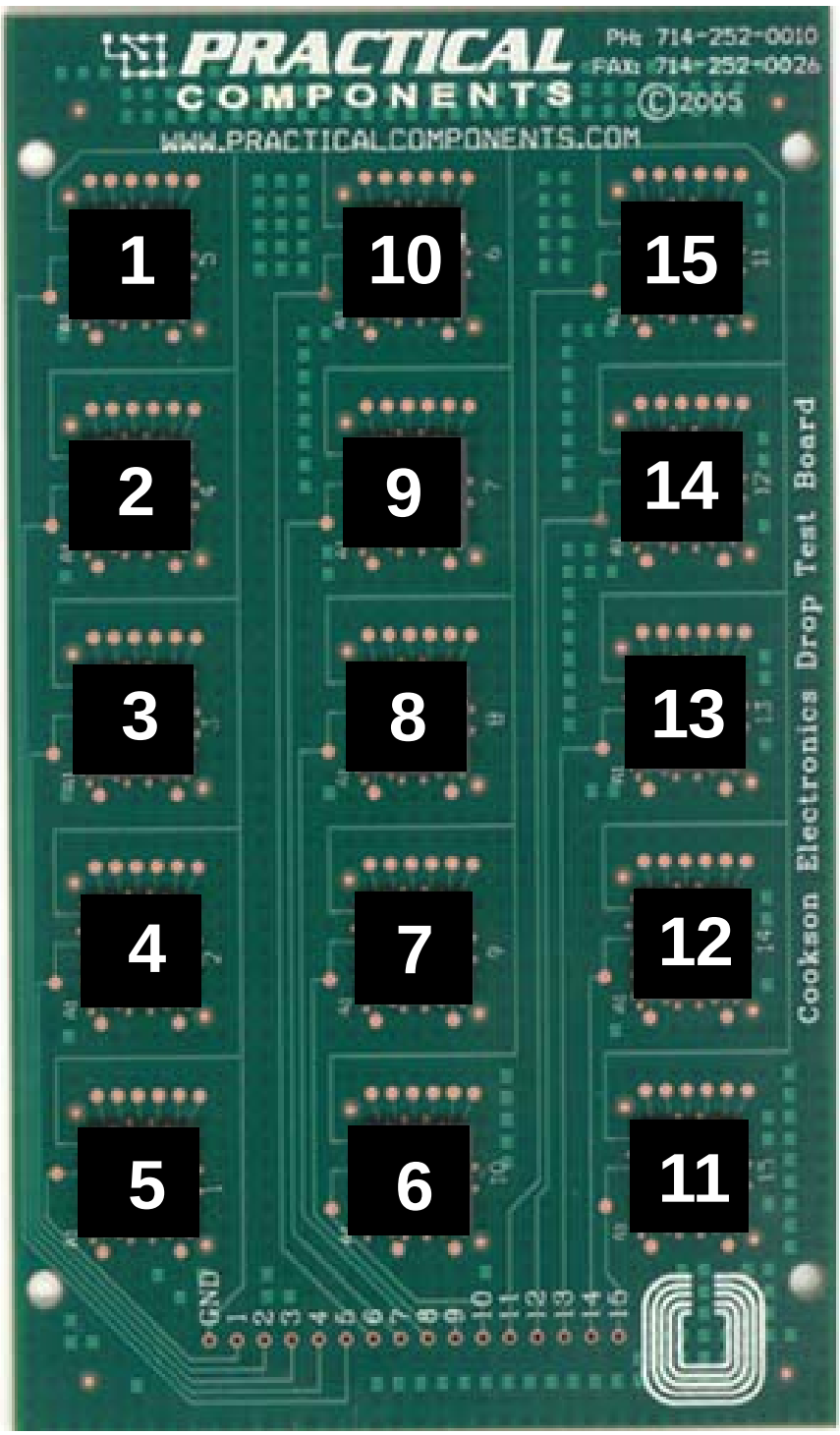

Figure 19: Configuration C Test Board (Plastic Package)

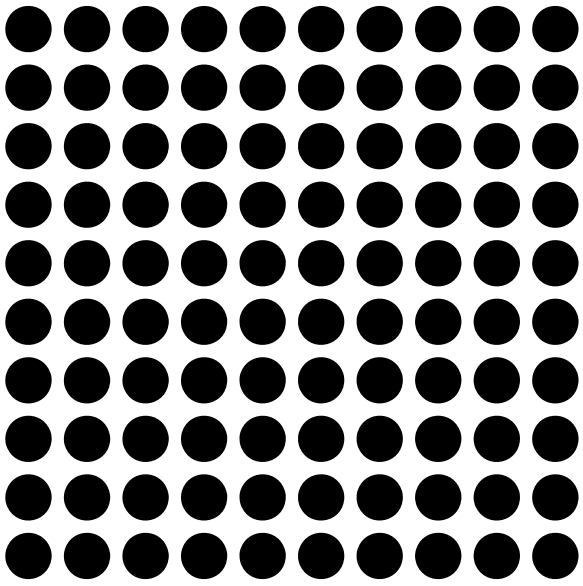

Figure 20: Interconnect array configuration for Test Board C, 100 I/O CABGA

Table 2: Configuration B Package Architecture (Plastic Package)

Parameter	19mm,PBGA (Test Board-B)	10mm, CABGA (Test Board-C)
Ball Count	324	100
Ball Pitch (mm)	1	0.8
Die Size (mm)	7.5	5.55
Substrate Thickness (mm)	0.3	0.232
Substrate Pad Type	SMD	NSMD
Ball Diameter (mm)	0.65	0.48

4.3 Experimental Set-Up

The Lansmont Model-23 drop tower has been used for shock testing of the board assemblies as shown in Figure 21. The drop height and pulse shape has been adjusted using pulse shaper between the impacting surfaces. The event has been monitored by two high speed cameras operating at 50,000 frames per second located as shown in schematic Figure 22. Two different high speed cameras mounted on tripods make an angle of 30° between them. Recommended angle for high accuracy is between 20° to 40° [Gu 2006, Helm 1996]. These synchronized cameras are externally triggered. Cameras are calibrated before recording the drop event which involves capturing the images of the target at different orientations as shown in Figure 23. Target specifications are 12 x 9 grid of black points on a white background with 9 mm pitch. 12 to 15 calibration images are recorded for good minimum error calibration results.

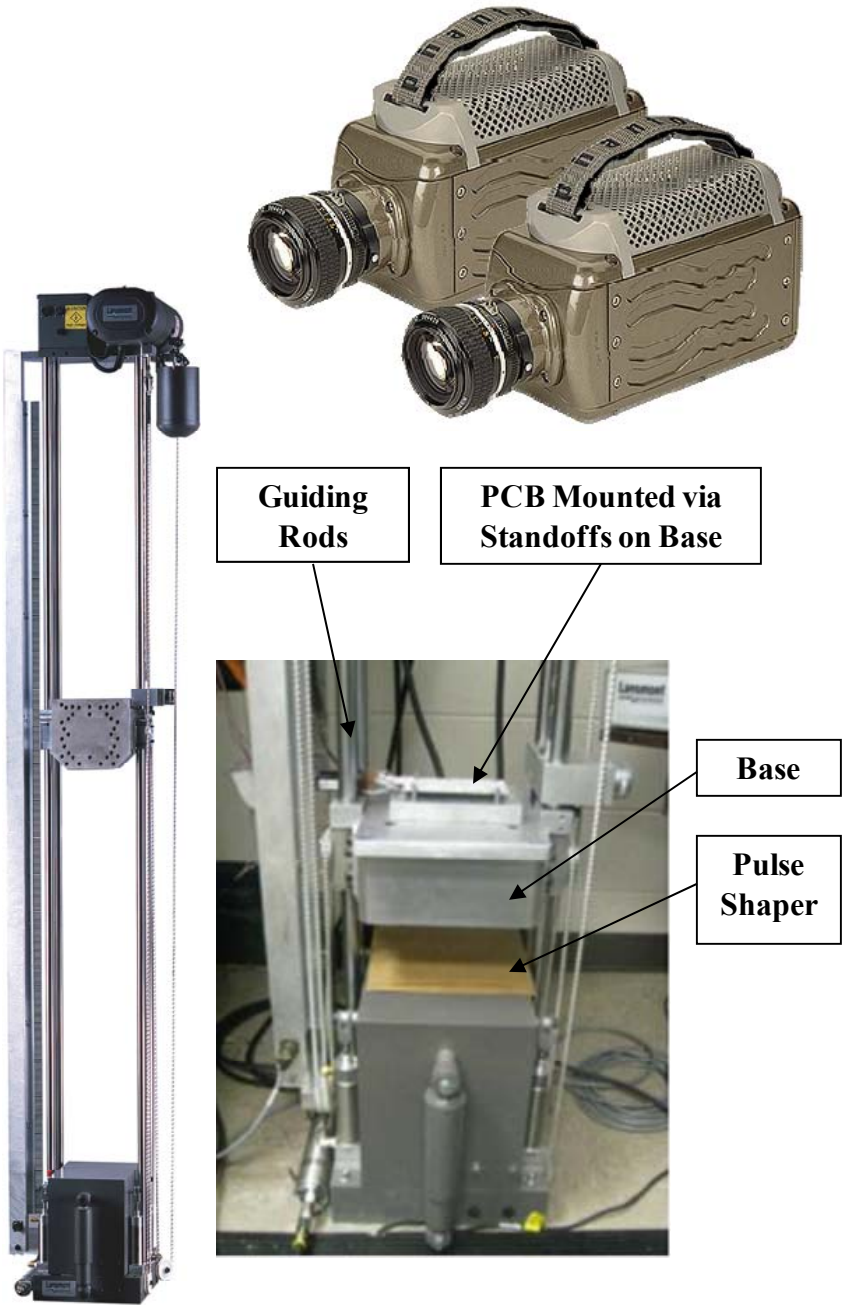

Figure 21: Lansmont Drop Tower Model23

Strain and continuity data is simultaneously acquired during a drop event using a high speed data acquisition system operating at a sampling frequency of 5 million samples per second. Failure is detected as an increase in the strain gage voltage. The board assemblies have been speckle-coated on both the board-side and package-side.

Different package locations on test boards exhibit different strain histories during the same drop and different number drops to failure.

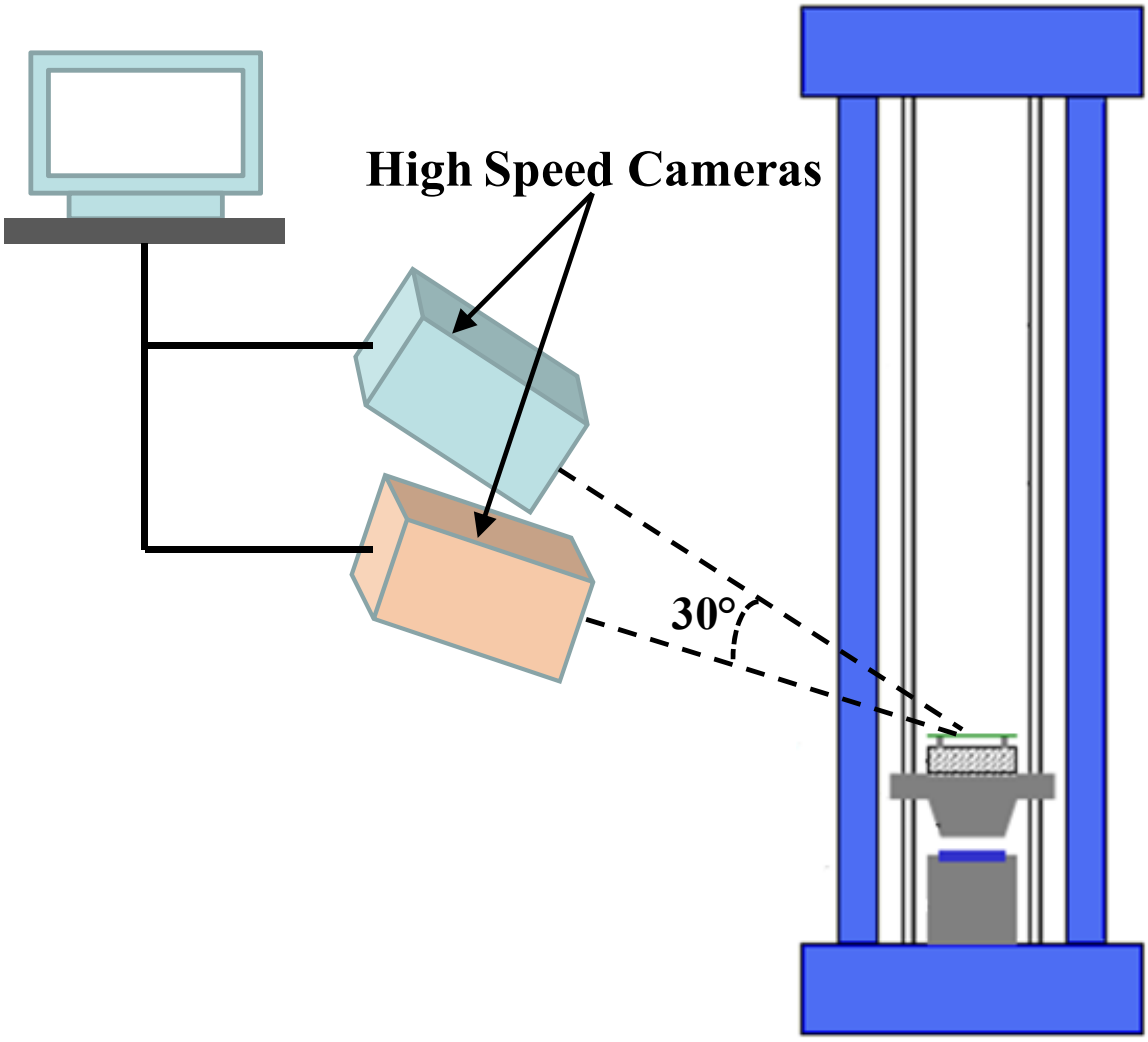

Figure 22: Schematic of drop tower with high speed cameras for DIC

Test- Board A and C have been subjected to 1500G, 0.5ms pulse in accordance with JESD22-B111 while test Board-B has been subjected to ~12,500Gs, 0.2 ms pulse, as shown in Figure 24.

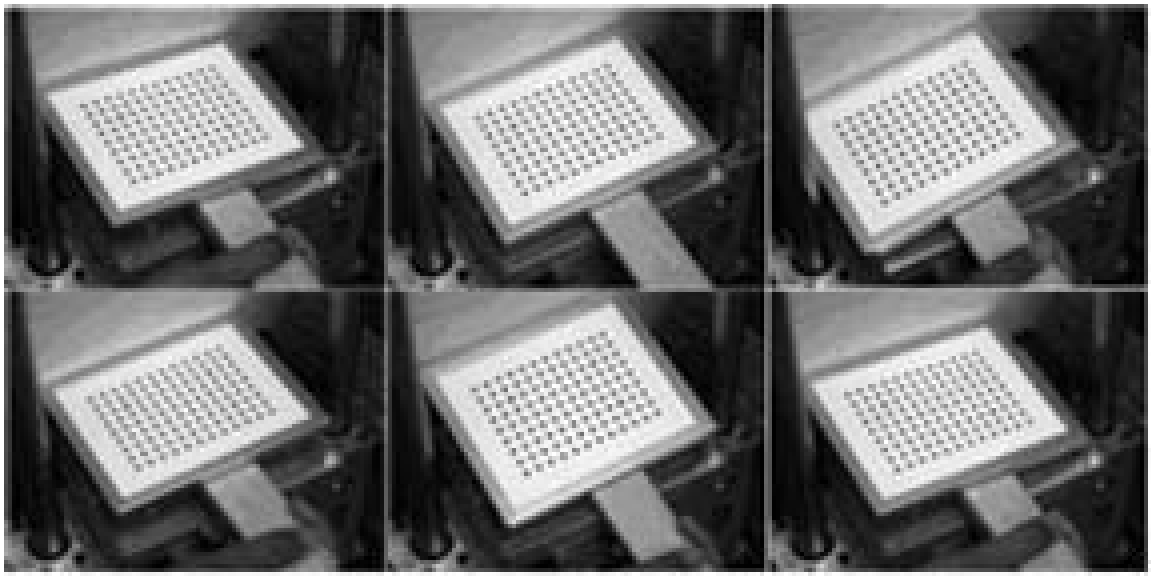

Figure 23: Calibration images captured at different orientations.

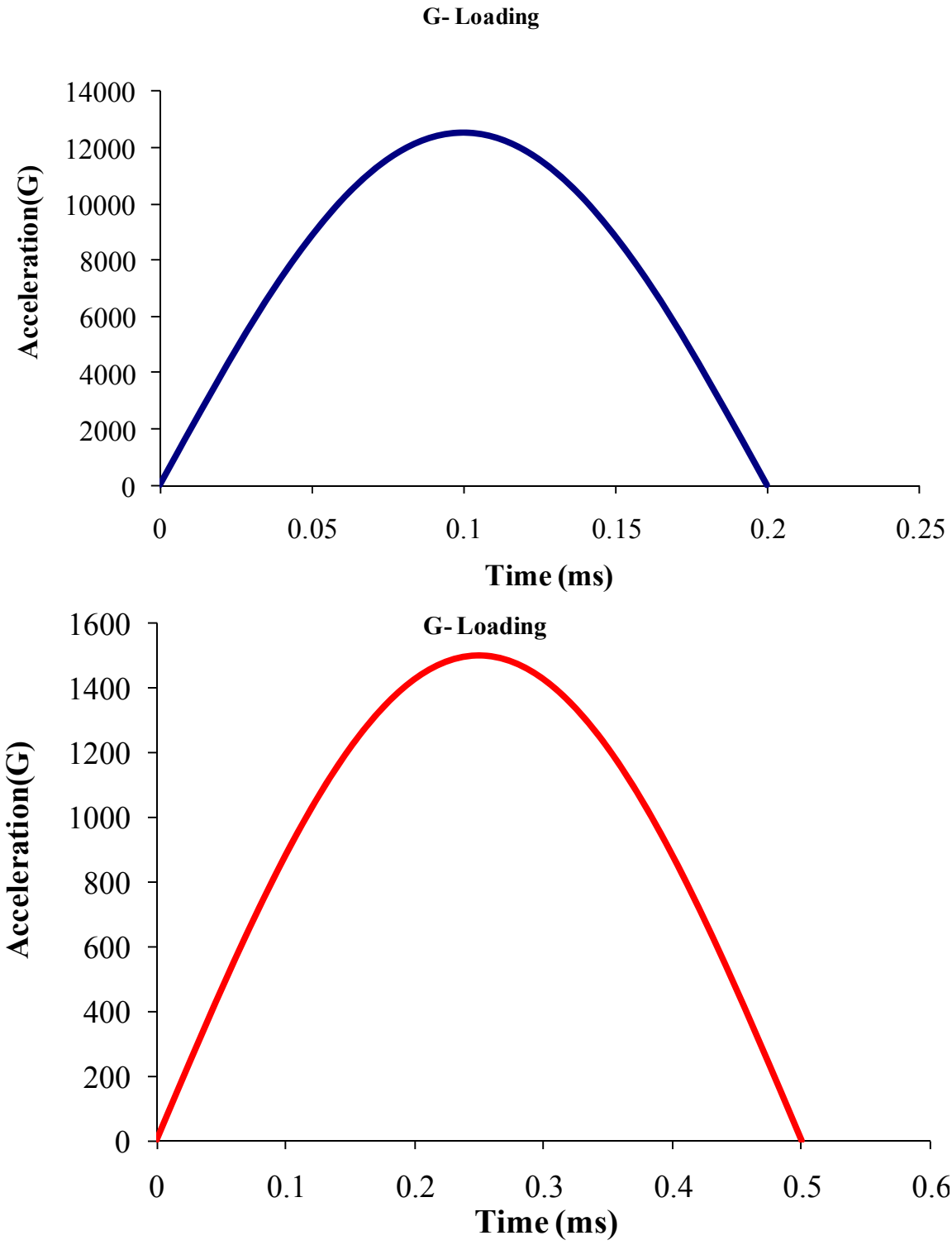

Figure 24: Acceleration for Test Boards

4.4 Digital Image Correlation

Digital image correlation (DIC) is an optical method to measure full field deformation and their derivatives of deformation on the surface of a loaded structure. The technique involves the application of speckle pattern on the surface of the printed circuit board assembly and tracking a geometric point on the speckle patterned surface before and after loading and using it to compute both in-plane as well as out-of-plane deformations in the structures.

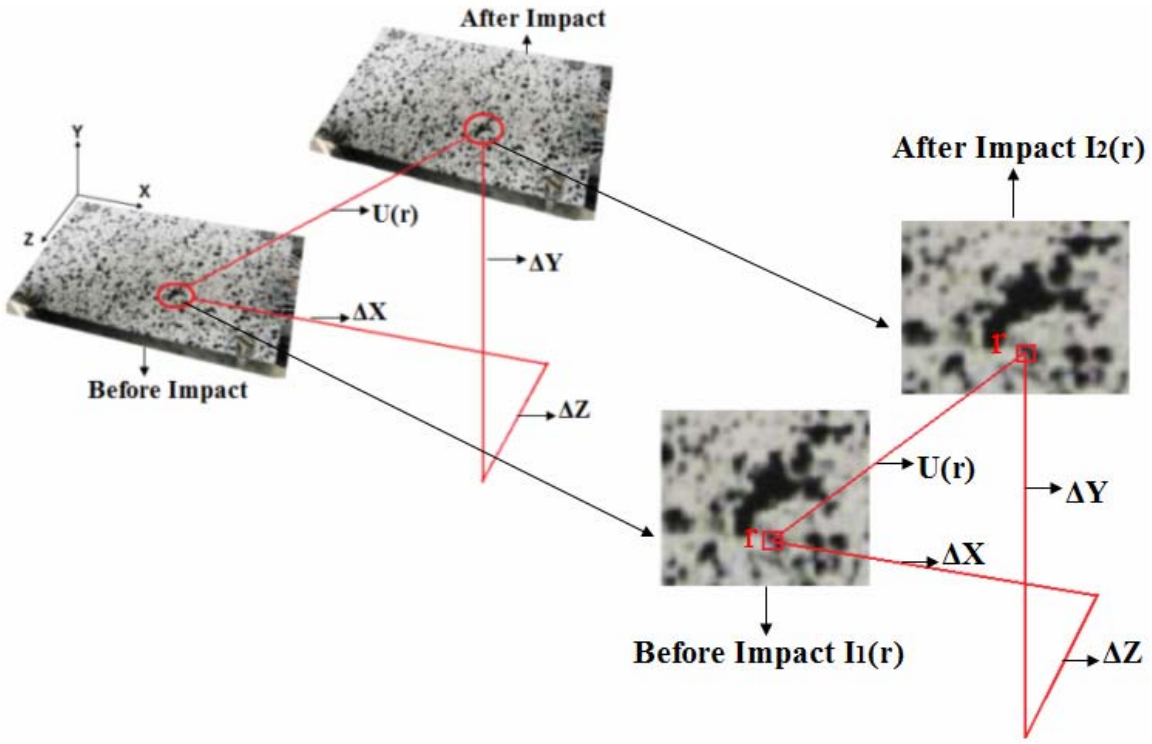

Figure 25: 3D-Digital Image Correlation Measurements in Printed Circuit Assembly

The tracking is achieved using digital image processing of speckle pattern on the specimen surface. Figure 25 shows the principle of DIC in 3-dimensional case. The sub image before impact is referred as $I_1(r)$ and the one after impact is referred as $I_2(r)$ respectively, which are related as follows:

$$I_2(r) = I_1[r - U(r)] \tag{4.1}$$

$$I_1(r) = I_2[r + U(r)] \tag{4.2}$$

where $U(r)$ is the displacement vector at pixel $r = (x, y)^T$. An algorithm based on the mutual correlation coefficient or other statistical functions are used to correlate the change in a reference pixel in the original image and the corresponding reference pixel in the deformed image. Three such typical correlations include absolute difference, least square and cross correlation. There are three typical correlation functions which are used and are defined as follows:

Absolute difference:

$$C_A(r') = 1 - \frac{\iint_\Omega \left| I_2(r + r') - I_1(r) \right| dr}{\iint_\Omega I_1(r) dr} \tag{4.3}$$

Least square:

$$C_L(r') = 1 - \frac{\iint_\Omega [I_2(r + r') - I_1(r)]^2 dr}{\iint_\Omega I_1^{\,2}(r) dr} \tag{4.4}$$

Cross-Correlation:

$$C_C(r') = 1 - \frac{\iint_\Omega I_1(r) I_2(r + r') dr}{\left[\iint_\Omega I_1^{\,2}(r) dr \iint_\Omega I_2^{\,2}(r + r') dr \right]^{1/2}} \tag{4.5}$$

where Ω (M x N) is the area of the sub image around reference pixel r, r` is the current pixel, $C_A(r')$ is the absolute correlation function, $C_L(r')$ is the least square correlation function, and $C_C(r')$ is the cross correlation function. In this research, digital image correlation has been used for material characterization of the solder under high strain rate as well as to determine the strain and deformation field on the entire PCB. Figure 26

shows the speckle coated PCB and Bimaterial Copper-Solder specimen during dynamic events of drop and high rate pull respectively.

Figure 26: Speckle Coated Printed Circuit Board on Drop Tower and Bimaterial Copper-Solder specimen during uniaxial tensile test.

4.5 Model Development

Node based sub-modeling has been used to provide boundary conditions to the XFEM sub-model. Three versions of the explicit global models include Timoshenko Beam Elements, smeared property, and cohesive zone models. Here the global-output of the experimental data has been used to drive the attachment degree of freedom of the XFEM sub-model. These attachment degrees of freedom are the driven nodes and correspond to the DIC data output locations on speckle coated PCB. Digital image correlation has been used to extract displacement and velocity along with strain components at discrete speckle patterned location on PCB. Two model methodologies are

applied in this study namely extended finite element models and explicit finite element models with cohesive elements.

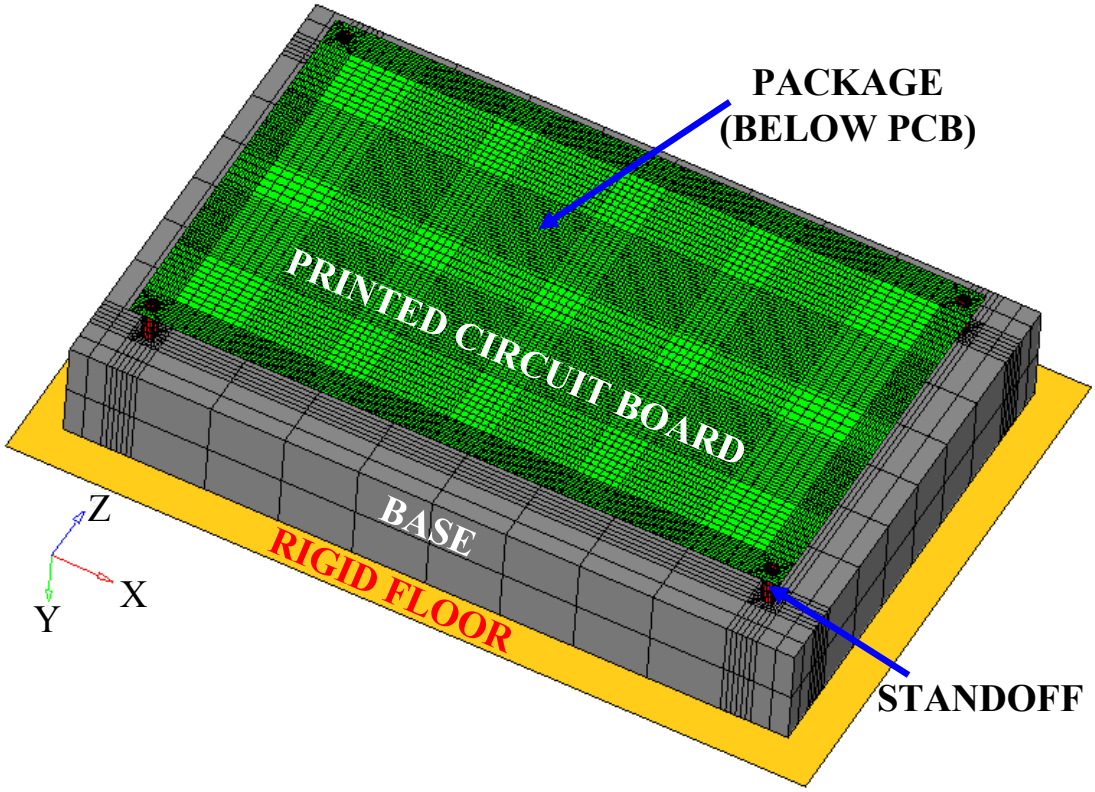

Figure 27: Explicit Global Model (Test Board –A)

In explicit analysis, transient dynamic behavior of the populated printed circuit boards has been simulated after creating smeared property models as shown in Figure 27. Smeared packages are modeled with three dimensional C3D8R continuum reduced integration element to increase computational efficiency. Smeared property models are computationally efficient and structurally equivalent to the original structure [Lall 2004, 2006]. PCB has been modeled with the S4R shell element and floor has been modeled as rigid element R3D4. Rayleigh damping has been used to model the damping behavior of the printed circuit assembly. Output from the global model is extracted at the cut-boundary nodes. Corners of the cut-boundary nodes are shown in Figure 28.

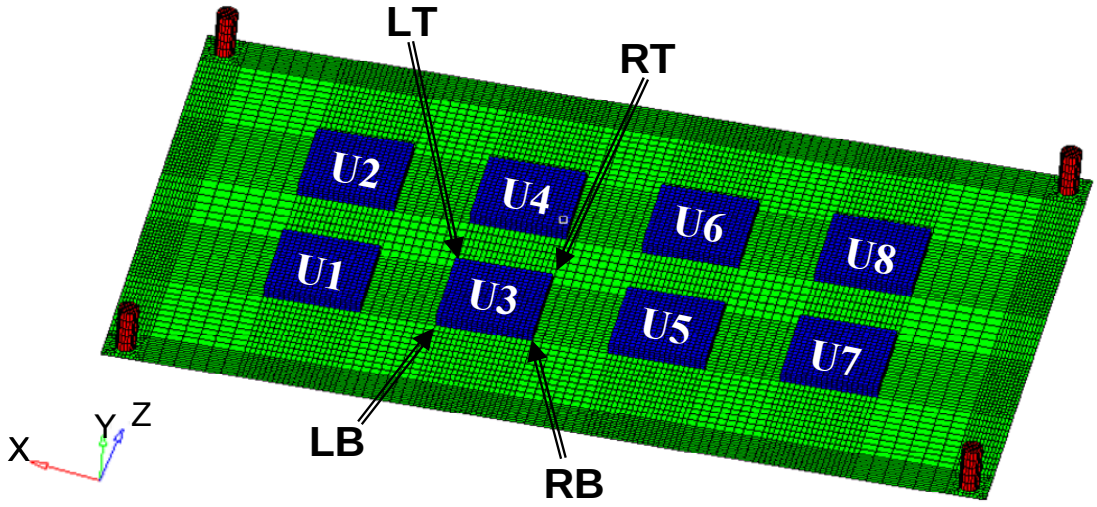

Figure 28: Package nomenclature and Output locations for Explicit Global models at given orientation (Test Board-A)

Figure 35 to Figure 39 shows FE models for various types of interconnects used. Figure 34 and Figure 35 shows the high-lead interconnect with spherical ball of Sn10Pb90 solder component surrounded by eutectic 63Sn37Pb solder component. Figure 36 and Figure 37 shows high lead Sn10Pb90 column wrapped with a copper spiral. The solder column and copper spiral are encased in a layer of eutectic 63Sn37Pb solder. The copper reinforcement is intended to enhance the interconnect reliability and provide redundancy in case of fracture of the solder column. Figure 29 to Figure 33 shows the submodels created for each kind of the package on the test board.

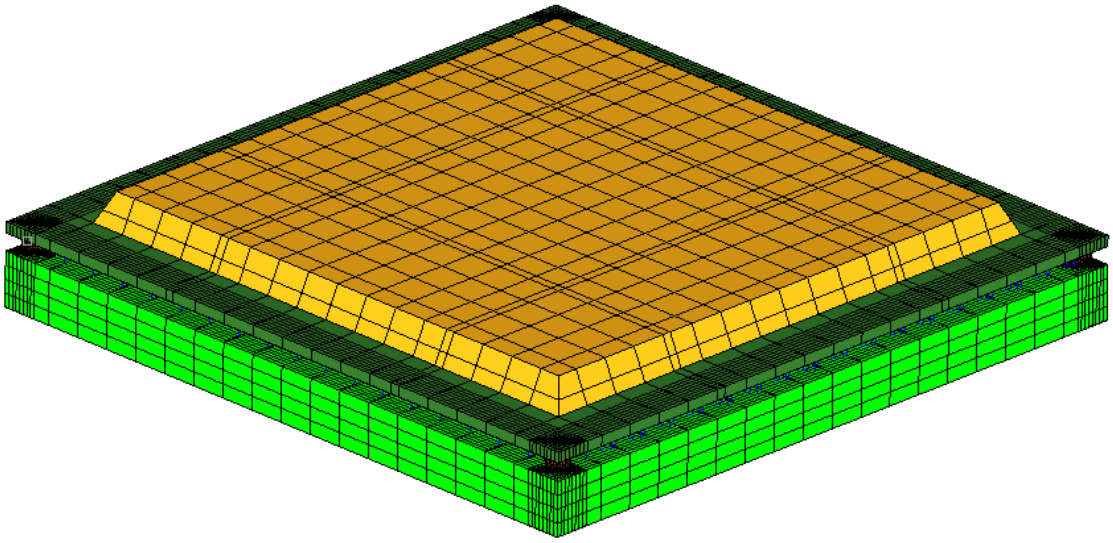

Figure 29: Submodel created for PBGA 324 Sn3Ag0.5Cu of Configuration B test vehicle

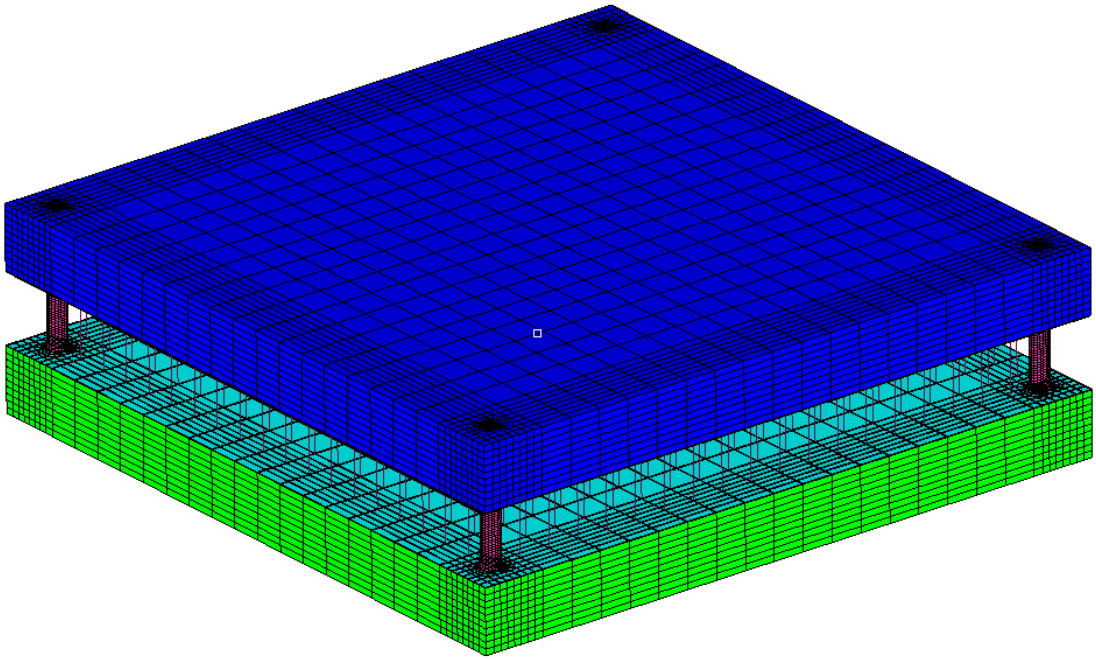

Figure 30: Submodel created for CCGA solder column of Configuration A test vehicle

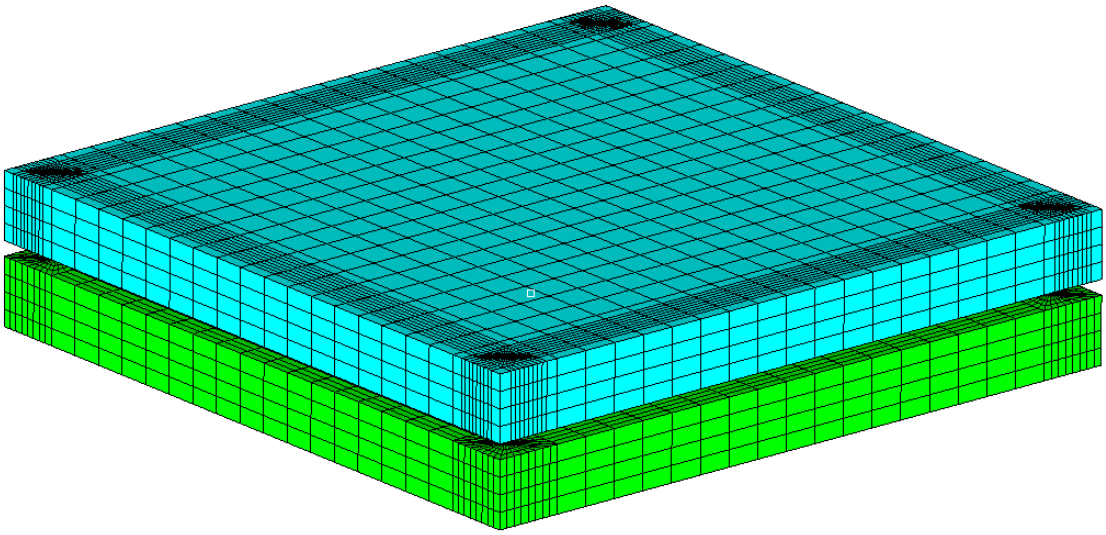

Figure 31: Submodel created for CBGA Sn3Ag0.5Cu of Configuration A test vehicle

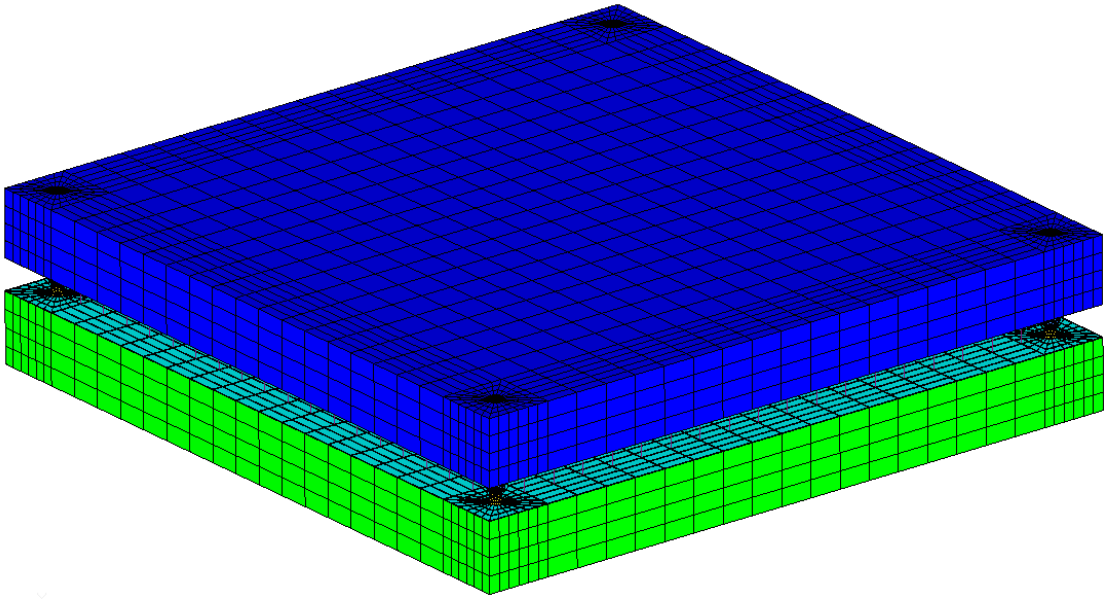

Figure 32: Submodel created for CBGA (Hi-Pb) of Configuration A test vehicle

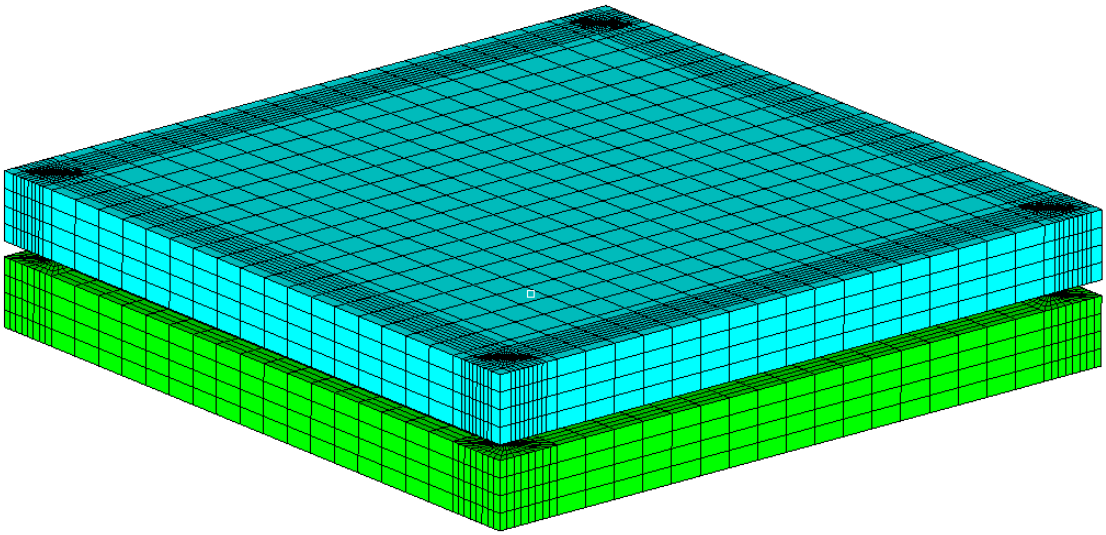

Figure 33: Submodel created for CBGA (63?Sn37Pb) of Configuration A test vehicle

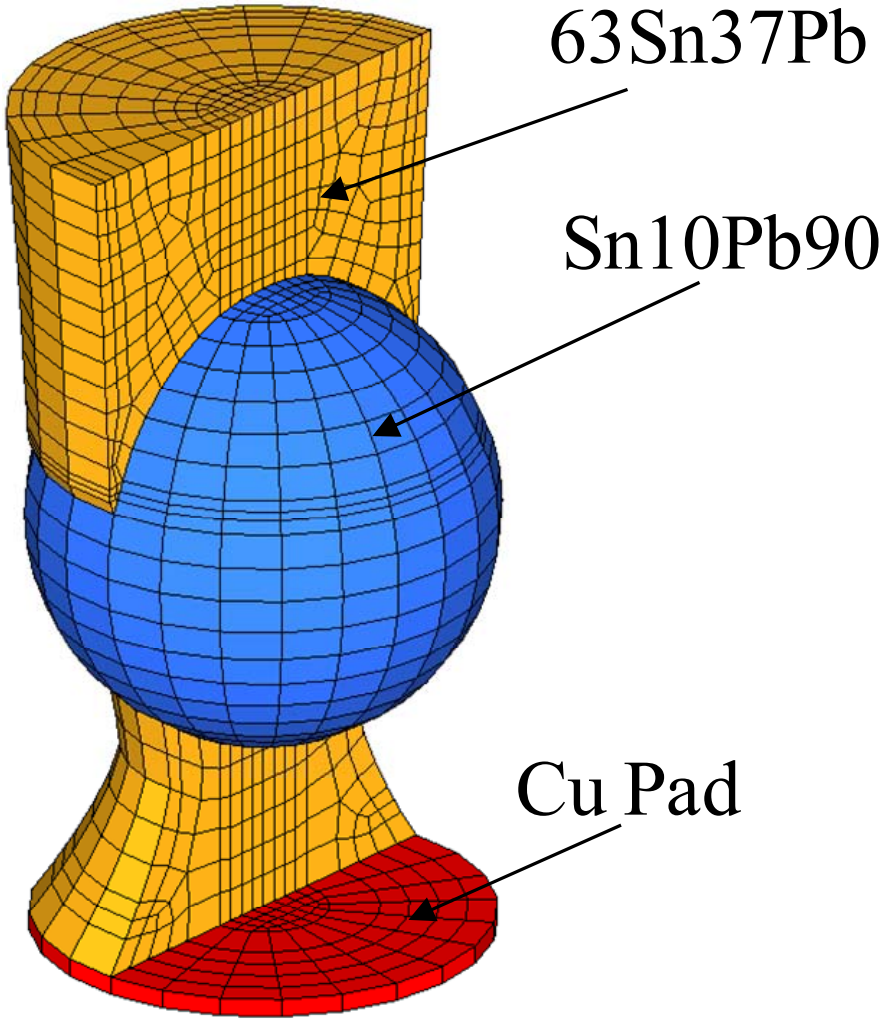

Figure 34: Cut Section view of FE model for 90Pb10Sn Solder Joint on CBGA interconnect

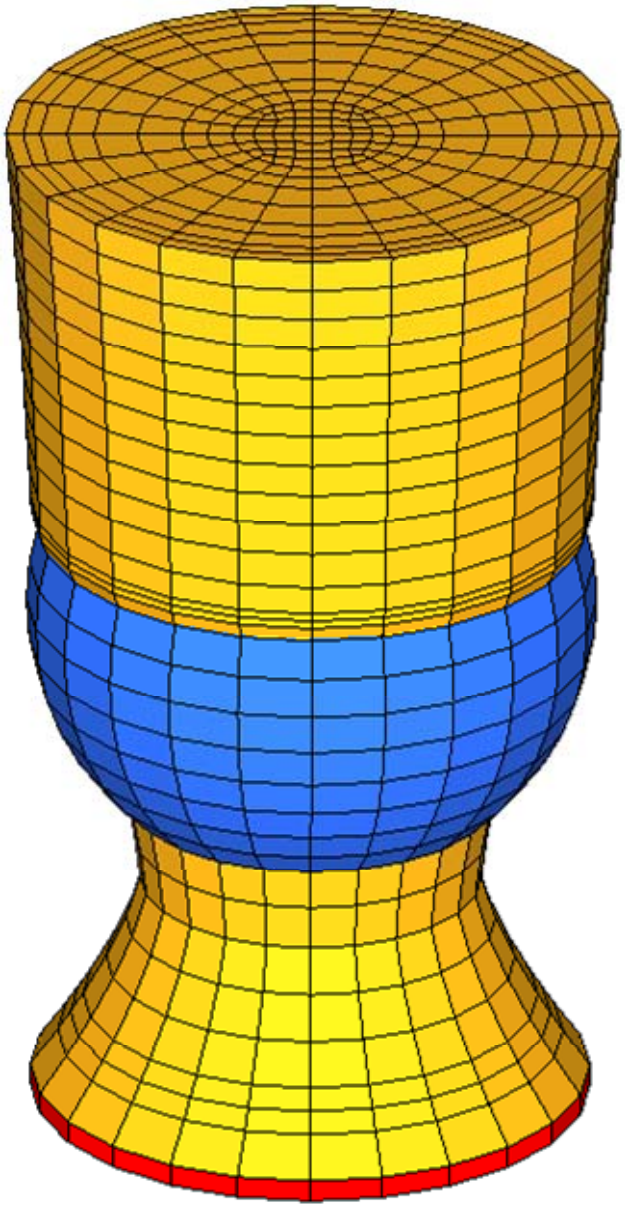

Figure 35: FE model for 90Pb10Sn Solder Joint on CBGA interconnect

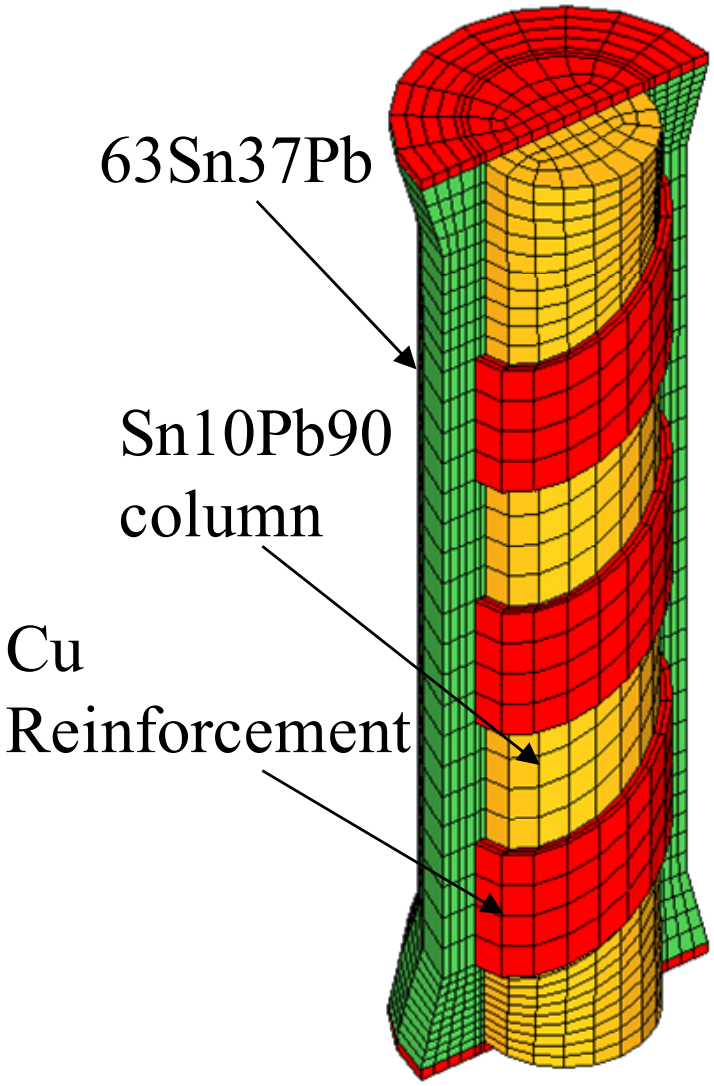

Figure 36: Cut Section view of FE model for Cu-Reinforced Solder Column on CCGA interconnect

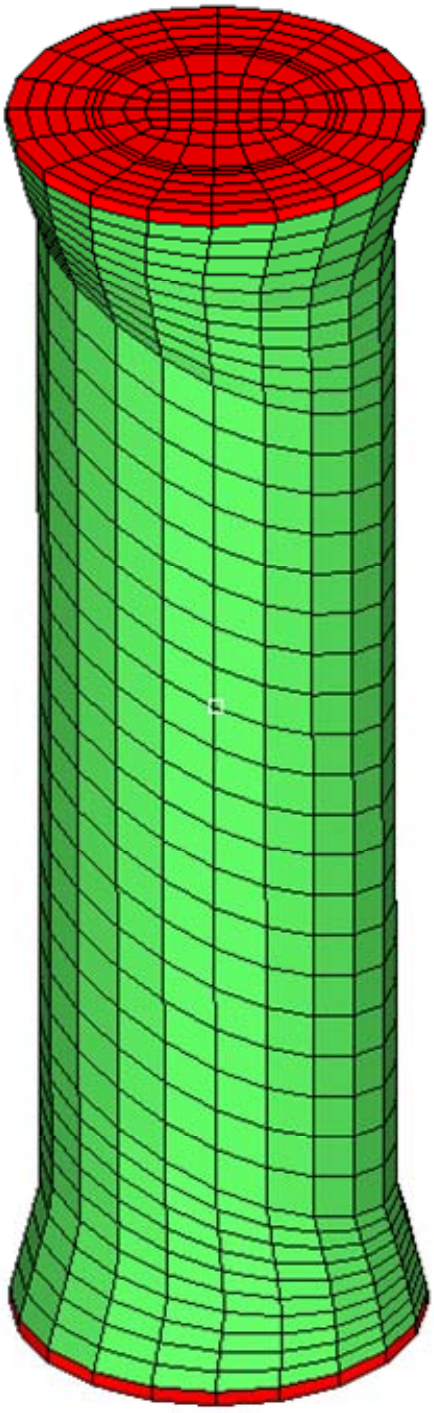

Figure 37: FE model for Cu-Reinforced Solder Column on CCGA interconnect

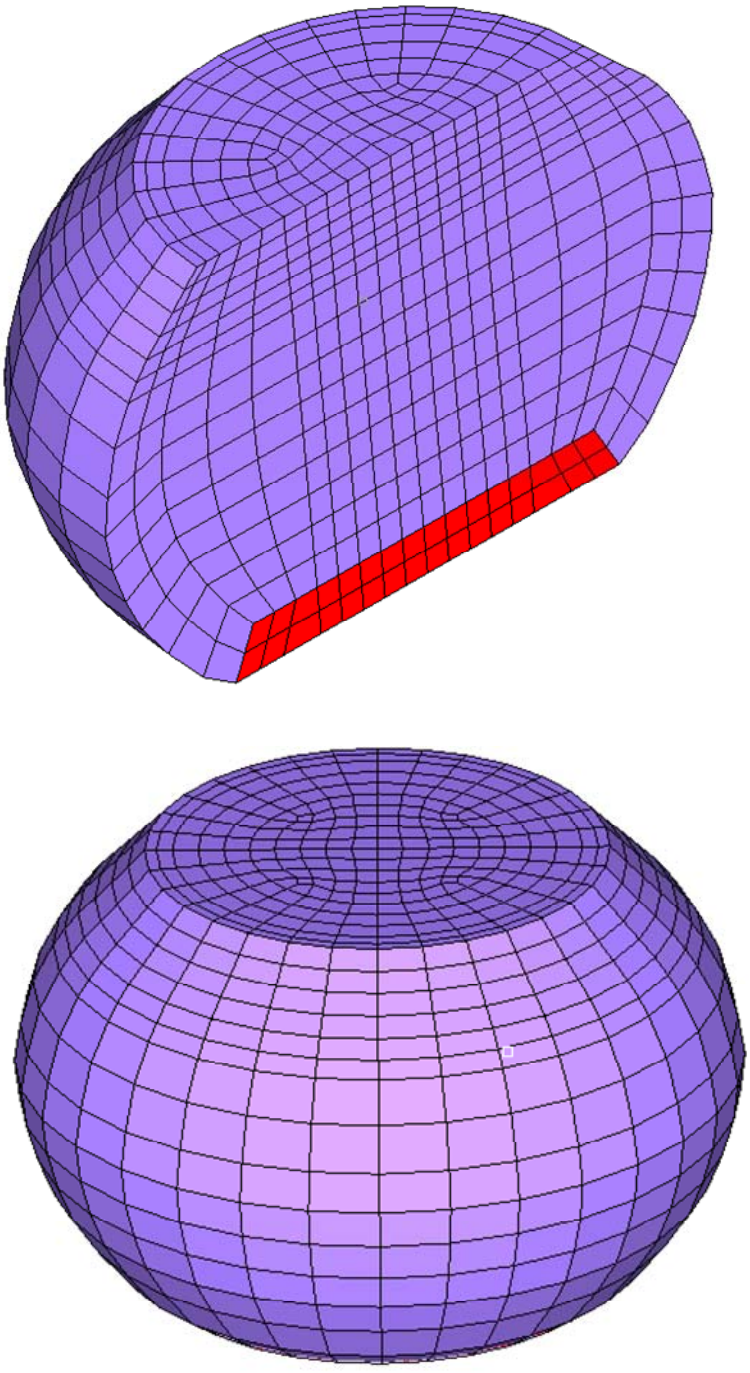

Figure 38: FE model for Sn3Ag0.5Cu Interconnect on CBGA interconnect

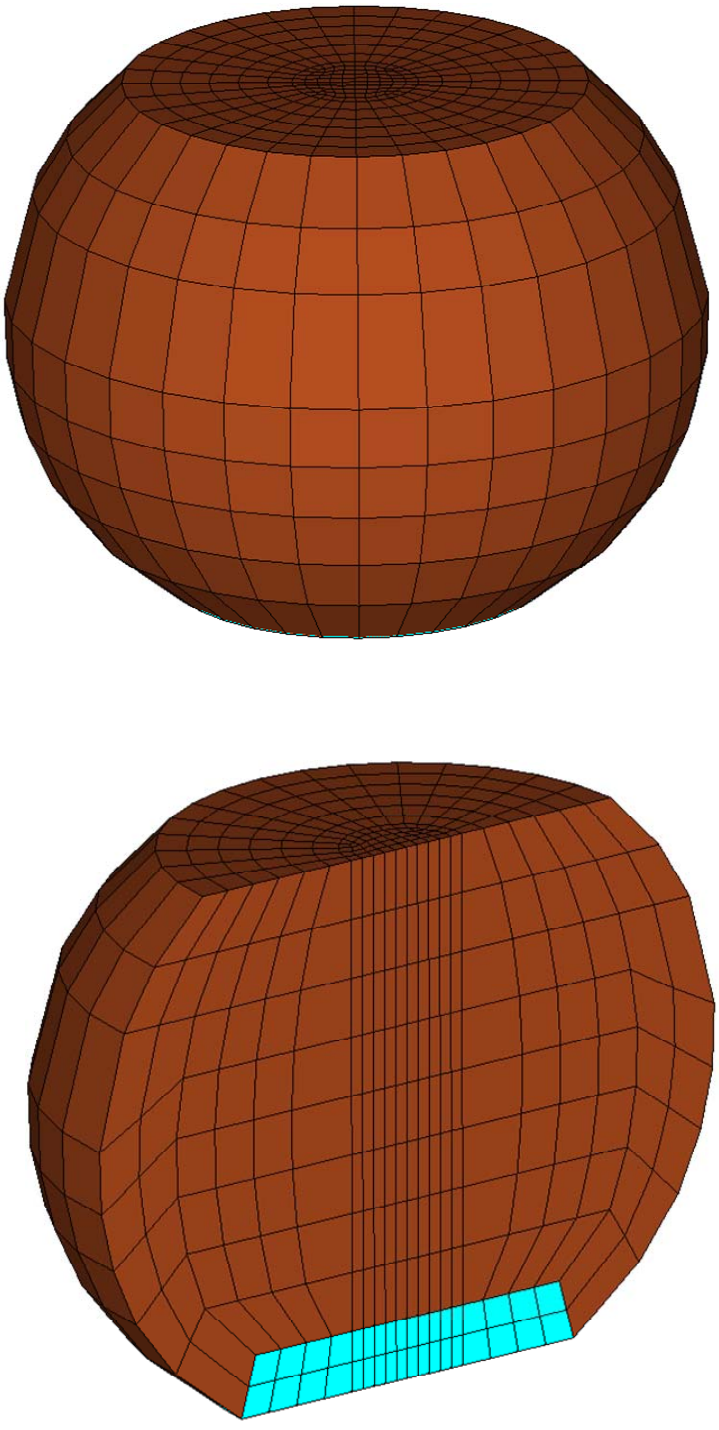

Figure 39: FE model for Sn3Ag0.5Cu Interconnect on PBGA324

Figure 40 shows the schematic of the methodology implemented for XFEM approach. For test board-A with ceramic packages, enrichment domains are defined in the solder region of corner balls. For SAC305 solder (Sn3Ag0.5Cu) and Eutectic tin lead solder (63Sn37Pb) interconnects, entire solder ball is assigned with enrichment domain properties. While for CCGA and Hi-Pb solder, eutectic phase at top and bottom of the interconnect column is enriched with additional degrees of freedom. Similarly entire corner solder sphere is modeled as enrichment domain for plastic package of test board-B. Enrichment domain creates the solution dependent region for XFEM analysis. Node based Submodeling approach is executed with velocity components from digital image correlation used as boundary conditions for all the sub-models. Damage thresholds derived from high rate test of bi-material specimen have been used in assigning the fracture strength of the solder material in the enrichment domain. Maximum principal stress criterion is used as damage initiation parameter. Damage behavior of the interface is governed by the traction separation laws. When this criterion is met, nucleation of the crack occurs and it travels to the adjacent element.

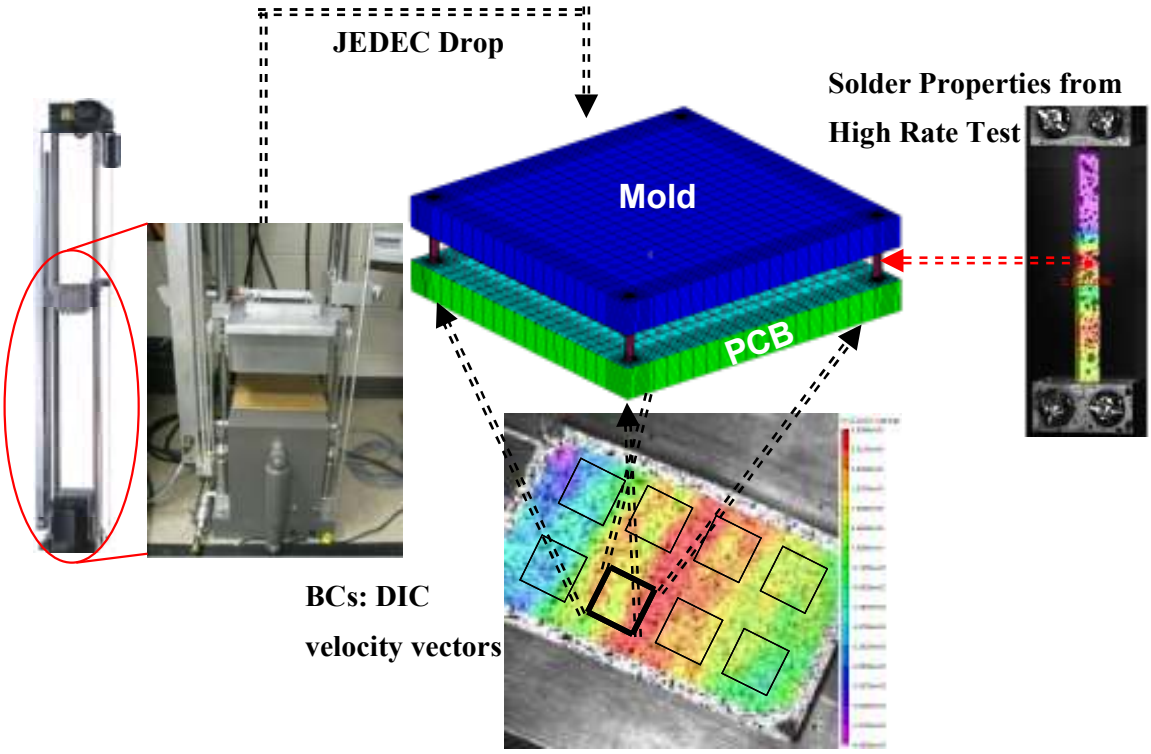

Figure 40: Schematic of methodology in implementing XFEM for Drop event of PCB

The extended finite element sub-models have been created for all the packages on both test vehicles. The corner interconnects have been modeled with 8-node hexahedral element C3D8 elements. The remaining solder interconnects have been created with Timoshenko beam B31 elements. The Timoshenko beam element has six degrees of freedom at each node including, three translational and three rotational degrees of freedom. Rotational degrees of freedom have been constrained to model the interconnect behavior. All remaining package components including the chip, mold compound, substrate and printed circuit board have been modeled with C3D8 elements. Gravity loading has been added in the model to account for the inertia forces occurring during the drop event.

For CCGA column, location U3, initiation and propagation of crack at various times after the impact during the transient shock-event, is shown in Figure 41. Model predictions indicate crack initiation at 1.55 ms after the impact. Failure initiates in interconnects right above the fillet region. Figure 42 and Figure 43 show crack initiation and propagation in bulk solder for Sn3Ag0.5Cu and 63Sn37Pb configurations. Figure 44 shows the crack initiation in the 90Pb10Sn solder interconnect through the 63Sn37Pb wetted attachment layer. Figure 45 shows a crack that has initiated in solder layer on PCB side of the element for Plastic package with SAC305 interconnect. Average stress state has been used to determine the instances and extension of the crack through the solder component of the package.

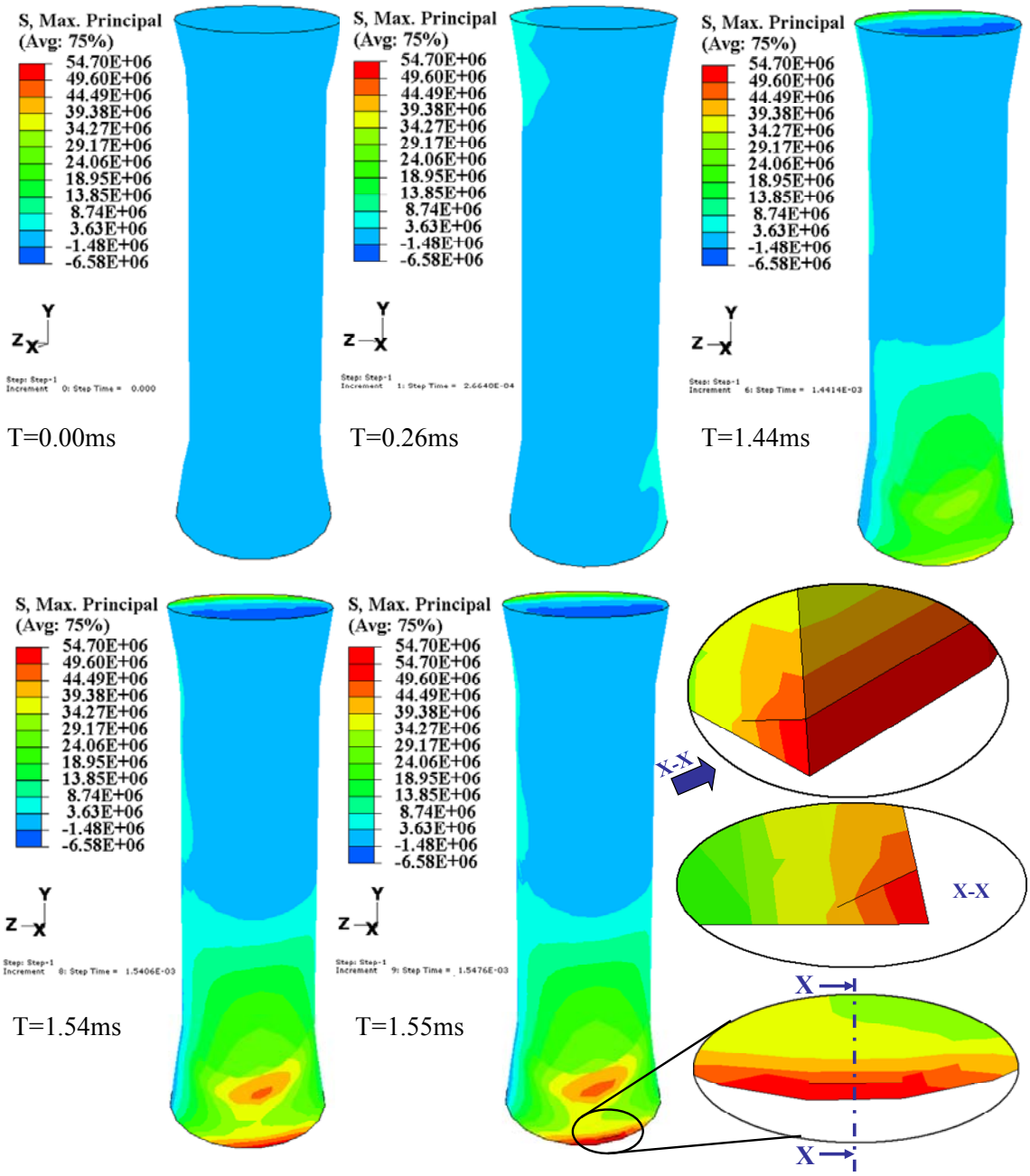

Figure 41: Crack Initiation and Propagation in CCGA column solder joints at different time intervals after the occurrence of impact using XFEM

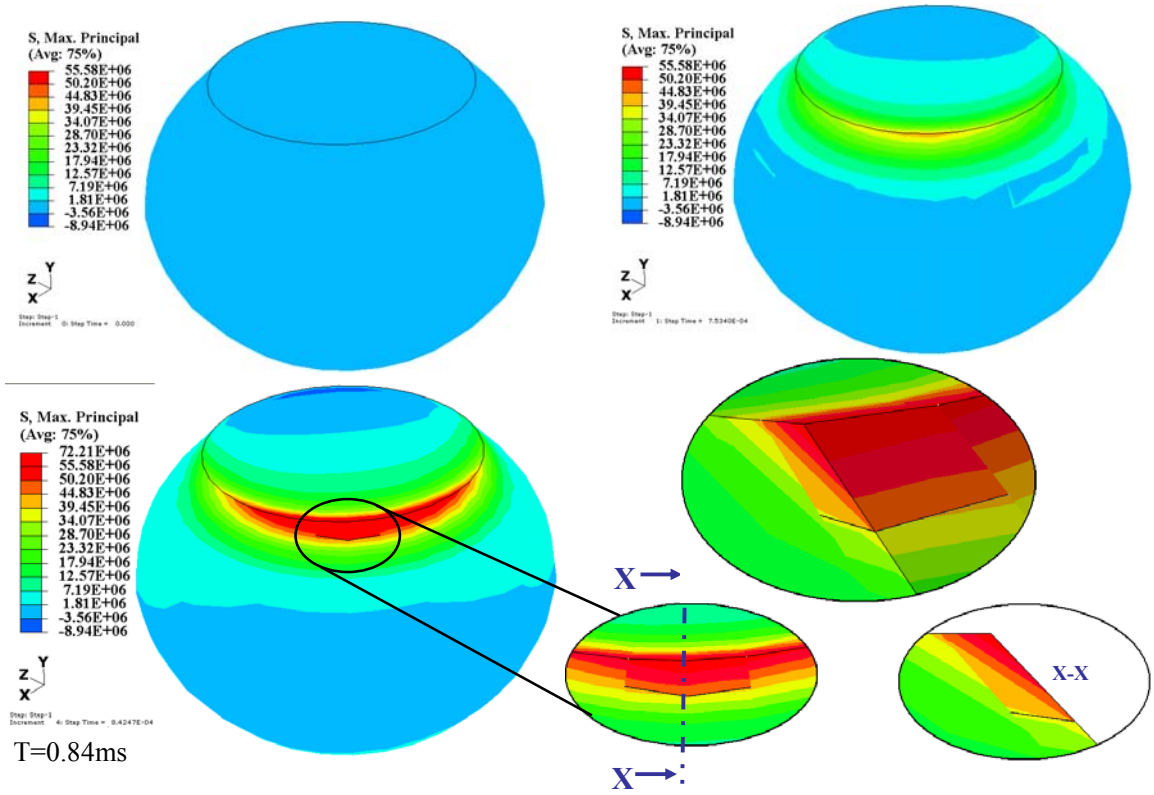

Figure 42: Crack Initiation and Propagation in CBGA Sn3Ag0.5Cu solder joints at different time intervals after the occurrence of impact using XFEM

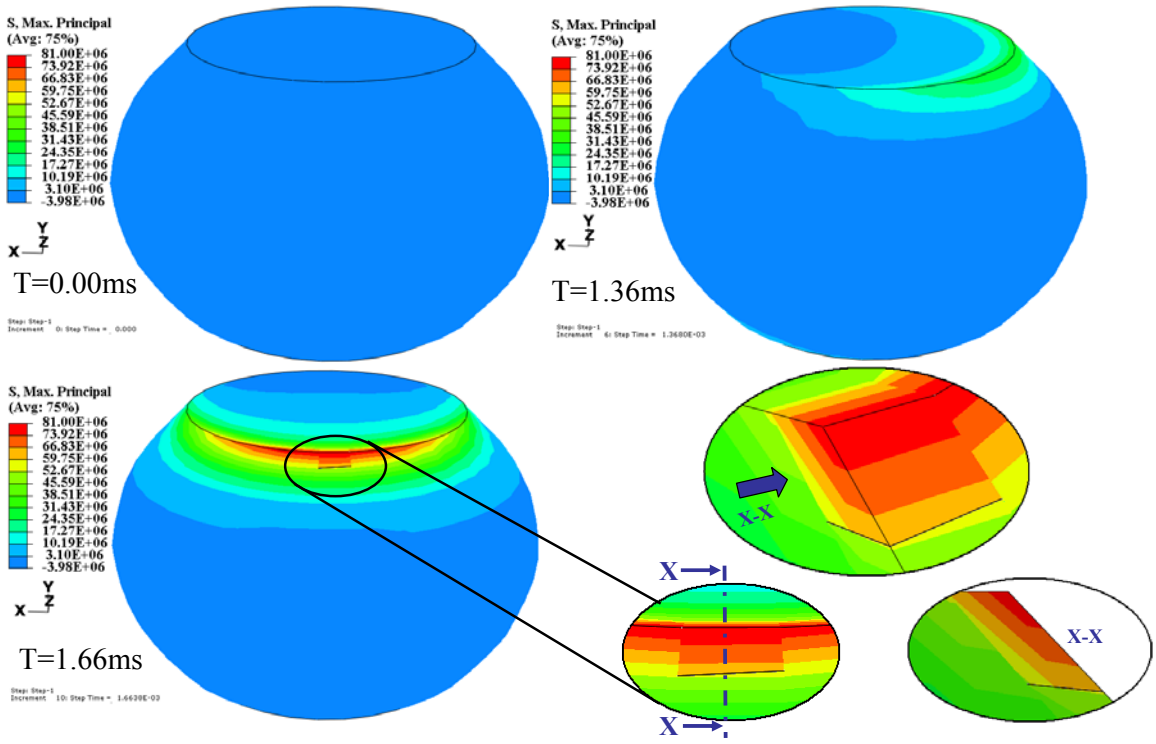

Figure 43: Crack Initiation and Propagation in CBGA Eutectic Tin lead solder joints at different time intervals after the occurrence of impact using XFEM

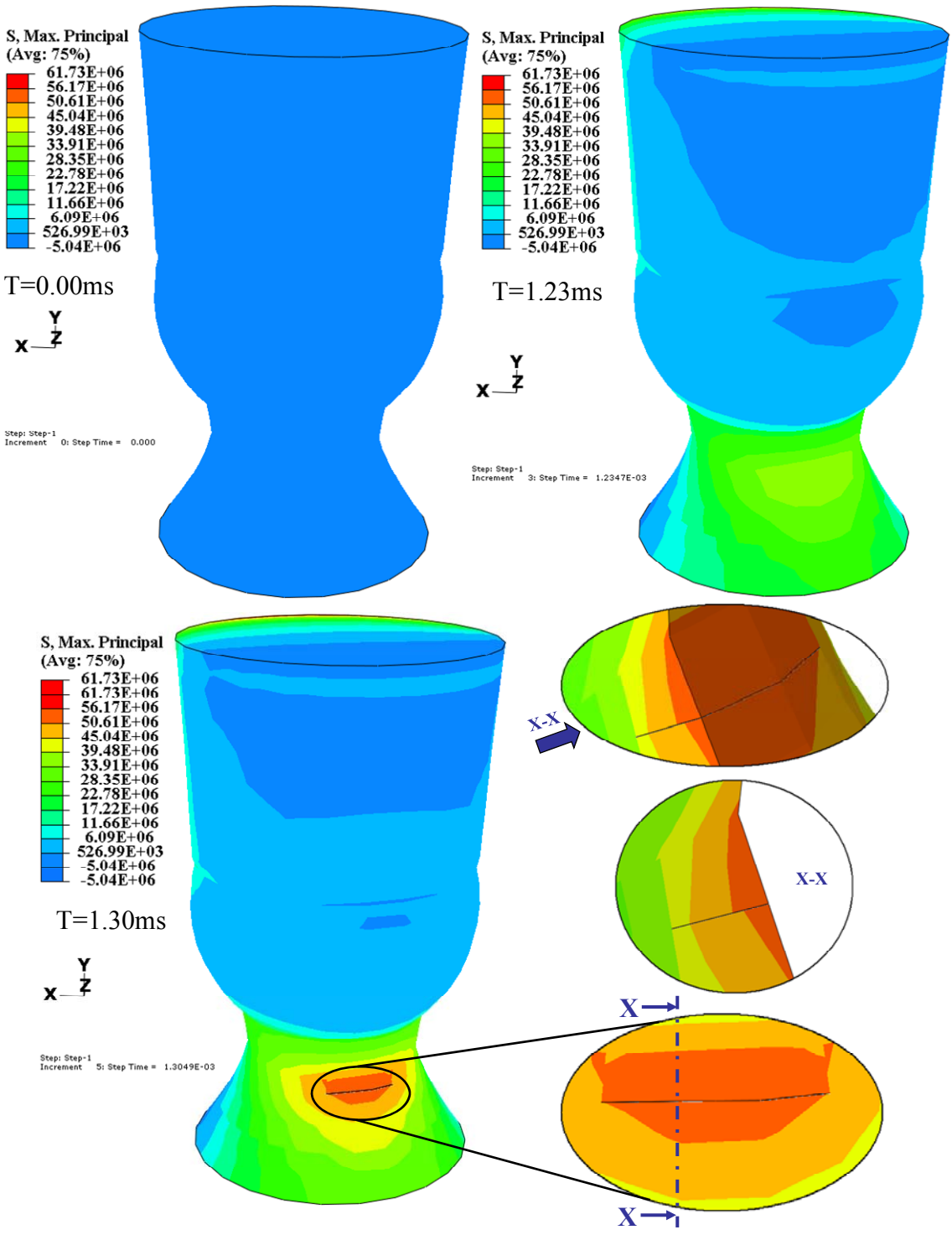

Figure 44: Crack Initiation and Propagation in CBGA Hi-Pb solder joints at different time intervals after the occurrence of impact using XFEM

Figure 46 shows the crack initiation and progression in the 63Sn37Pb solder joint of the ceramic package using the cohesive zone model. The model predictions from CZM correlate well with XFEM models.

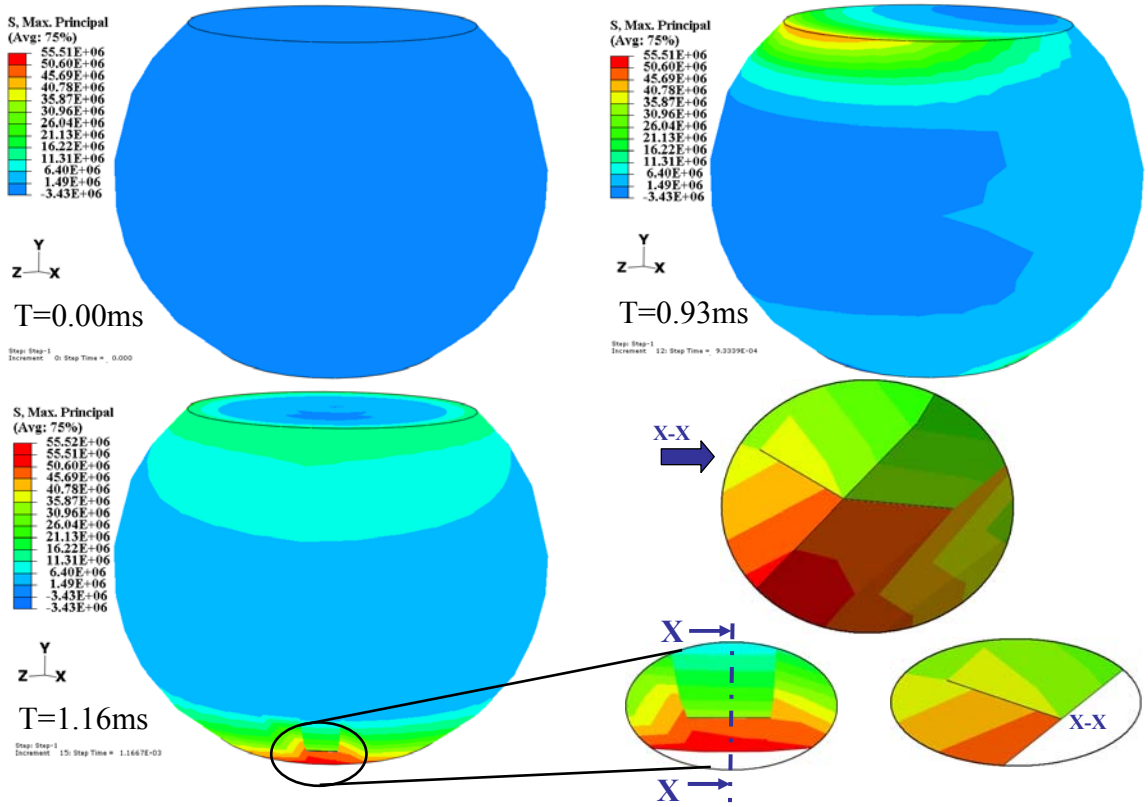

Figure 45: Crack Initiation and Propagation in PBGA Sn3Ag0.5Cu solder joints at different time intervals after the occurrence of impact using XFEM.

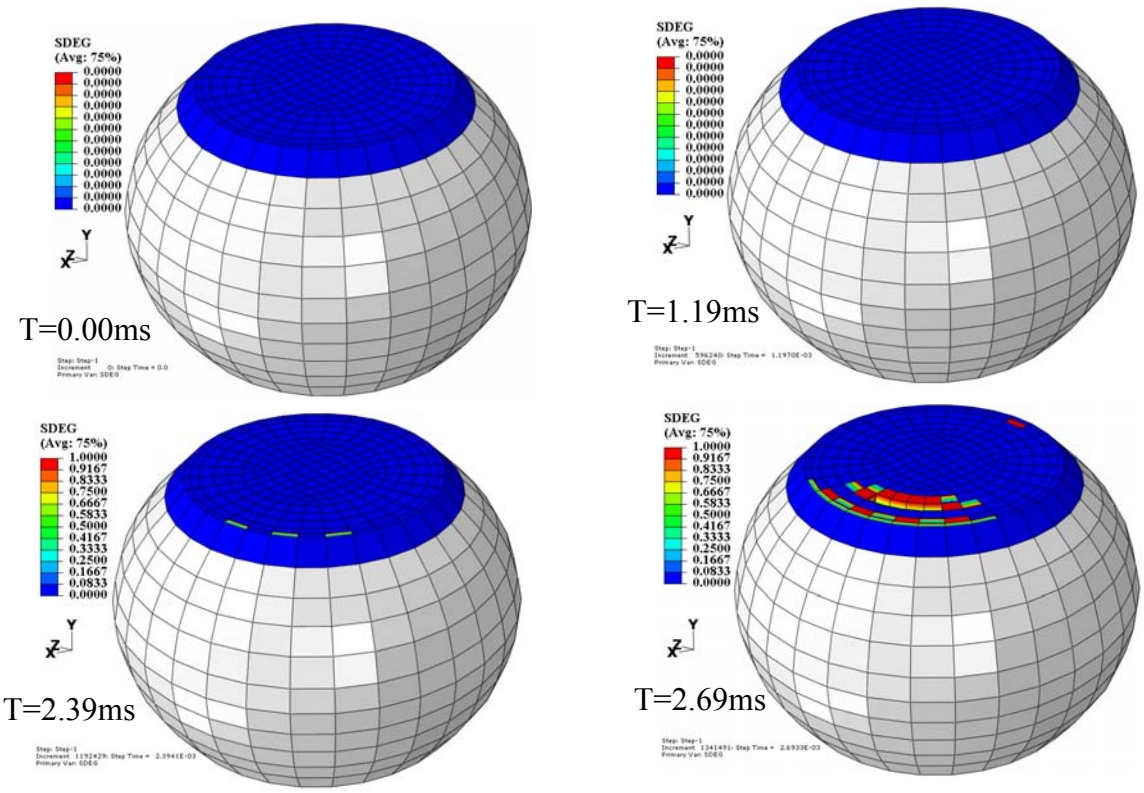

Figure 46: Crack Initiation and Propagation in Test Board A CBGA Eutectic Tin lead solder joints at different time intervals after the occurrence of impact using Cohesive Zone Modeling

4.6 Correlation of Model Predictions with Experimental Data

The results extracted from these models have been compared with the high-speed measurement of strains from digital image correlation. Figure 47 to Figure 50 shows the correlation between experimentally measured strain and simulation strain along the PCB length for package location U4 for 90Pb10Sn Solder Interconnect Ceramic Package in test board-A. Model predictions show good correlation with experimental data in both

magnitude and phase. Figure 51 to Figure 54 shows the correlation for package location U3 with 90Pb10Sn Solder Interconnect Ceramic Package in test board-A.

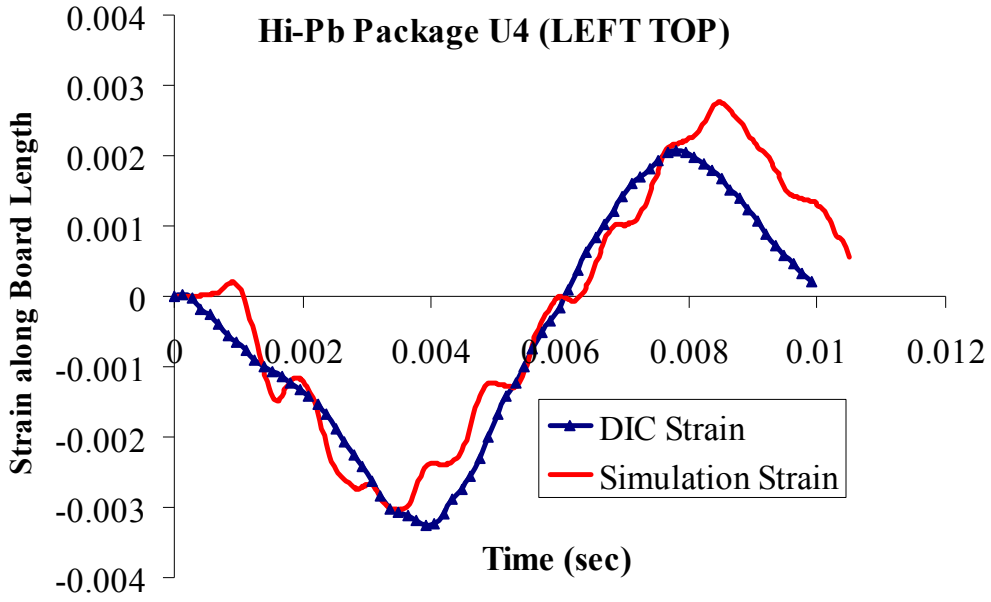

Figure 47: Strain Correlation between FE model and DIC for 90Pb10Sn Solder Interconnect CBGA at U4 (Left Top)

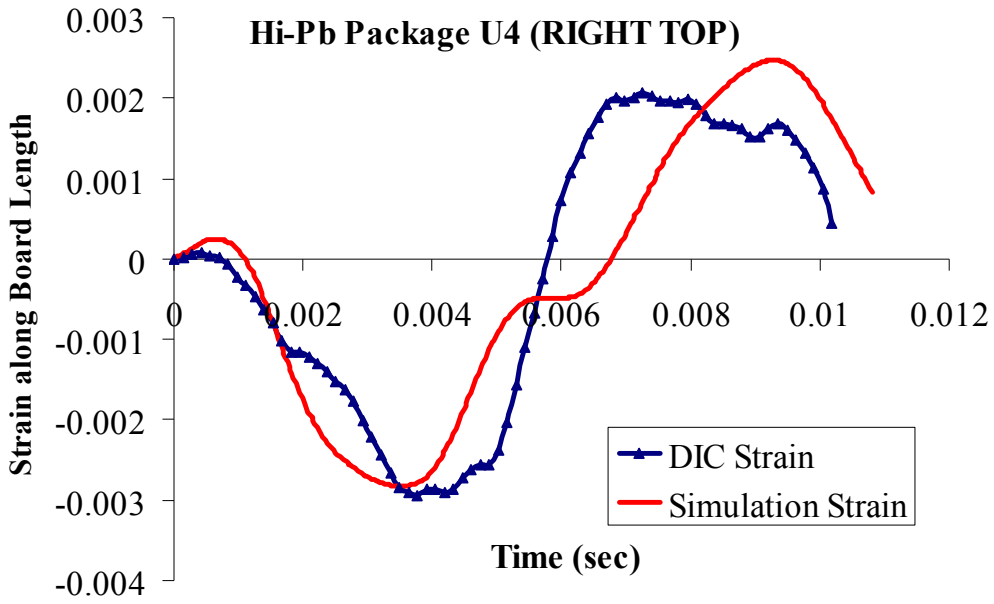

Figure 48: Strain Correlation between FE model and DIC for 90Pb10Sn Solder Interconnect CBGA at U4 (Right Top)

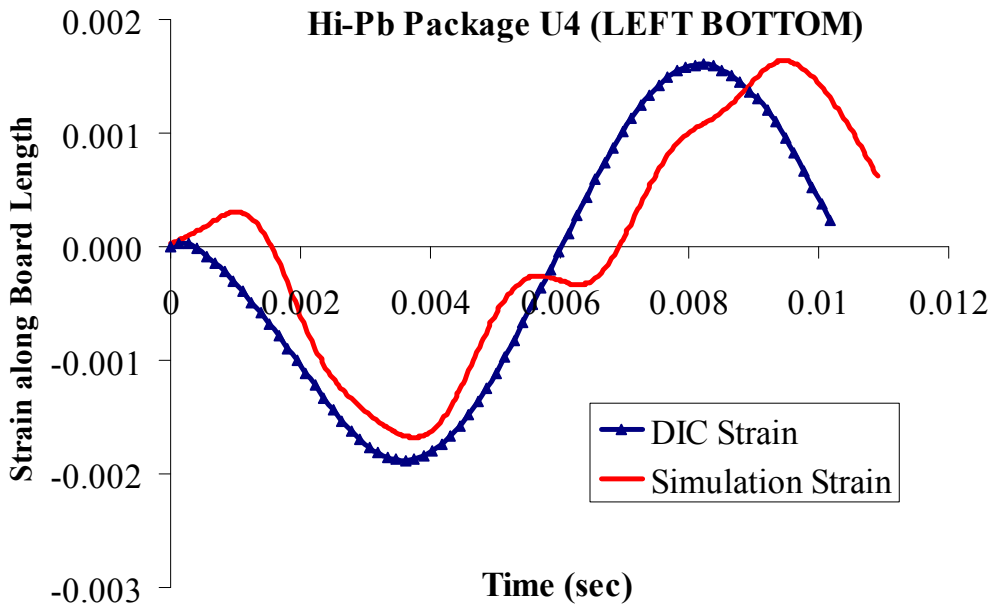

Figure 49: Strain Correlation between FE model and DIC for 90Pb10Sn Solder Interconnect CBGA at U4 (Left Bottom)

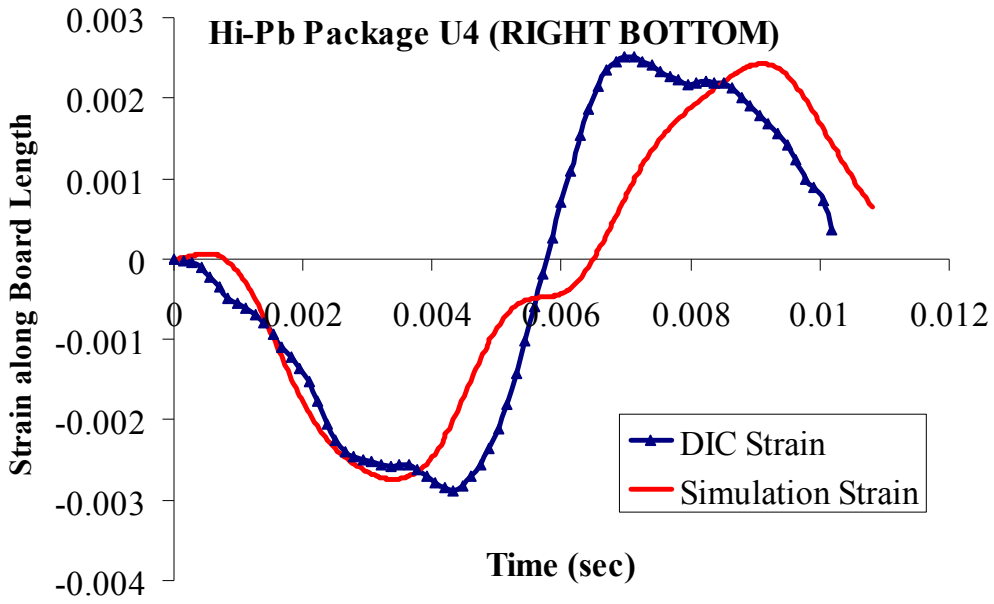

Figure 50: Strain Correlation between FE model and DIC for 90Pb10Sn Solder Interconnect CBGA at U4 (Right Bottom)

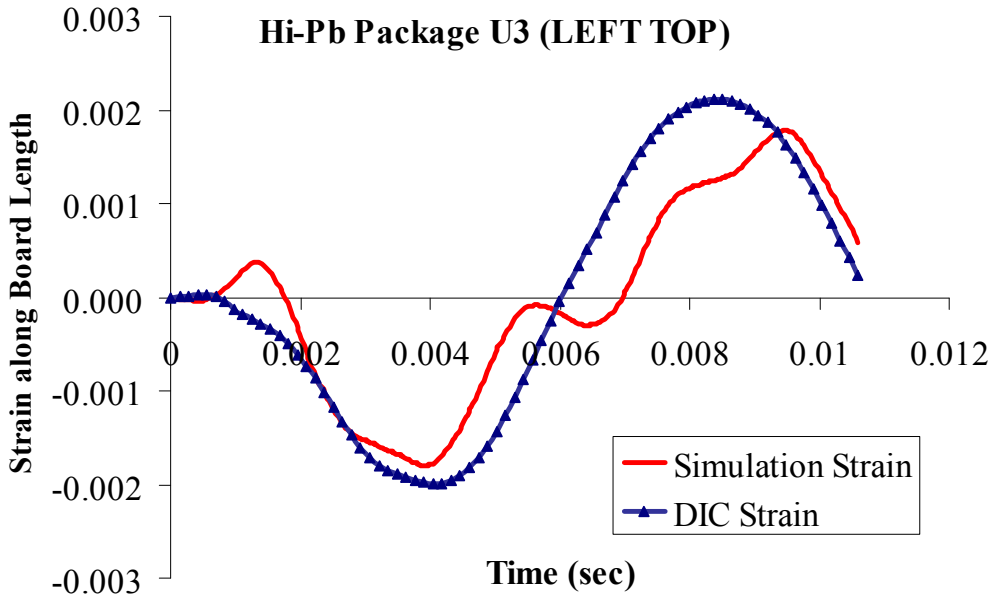

Figure 51: Strain Correlation between FE and DIC for 90Pb10Sn Solder Interconnect CBGA at U3 (Left Top)

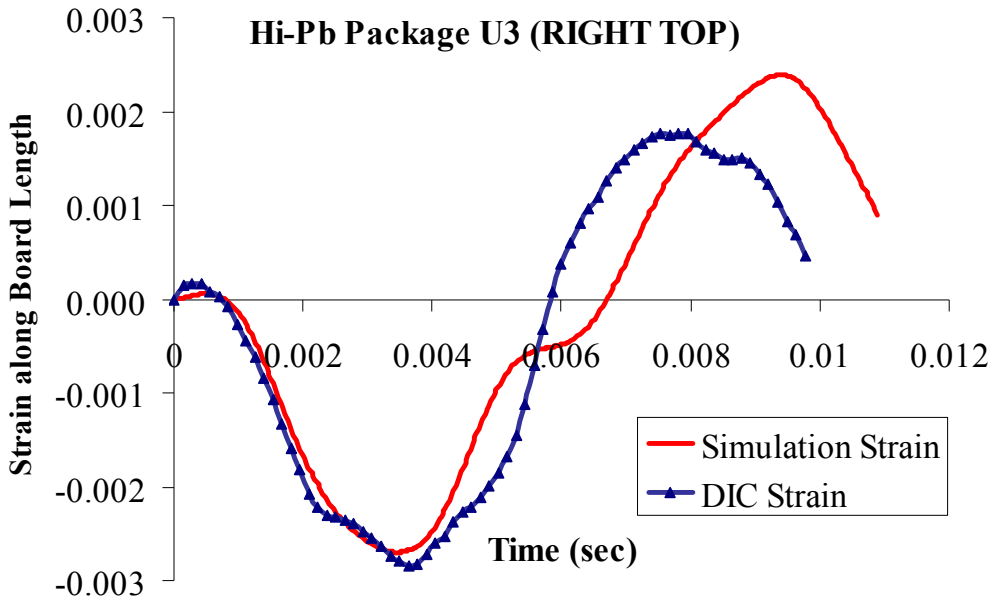

Figure 52: Strain Correlation between FE and DIC for 90Pb10Sn Solder Interconnect CBGA at U3 (Right Top)

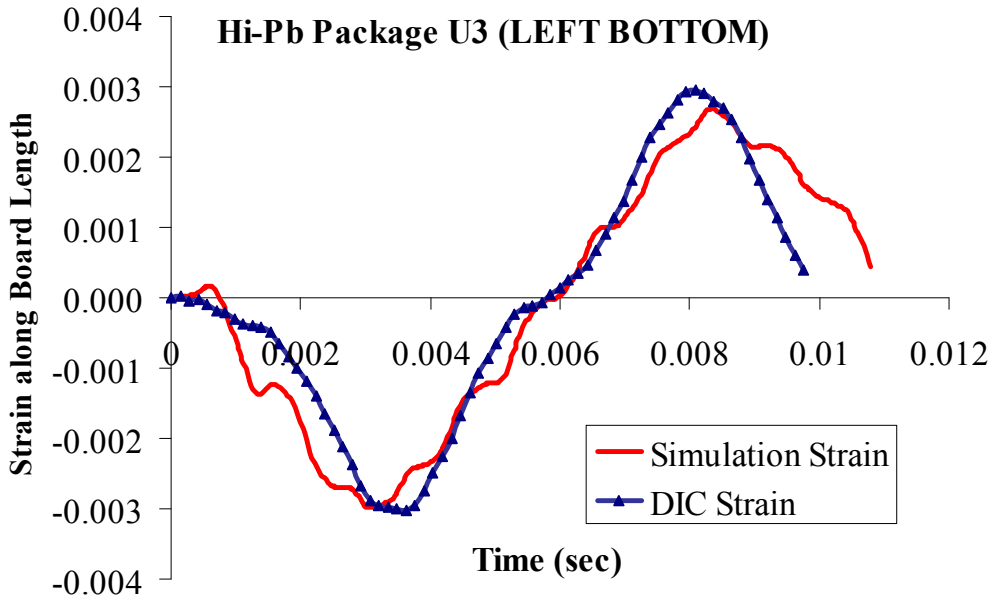

Figure 53: Strain Correlation between FE and DIC for 90Pb10Sn Solder Interconnect CBGA at U3 (Left Bottom)

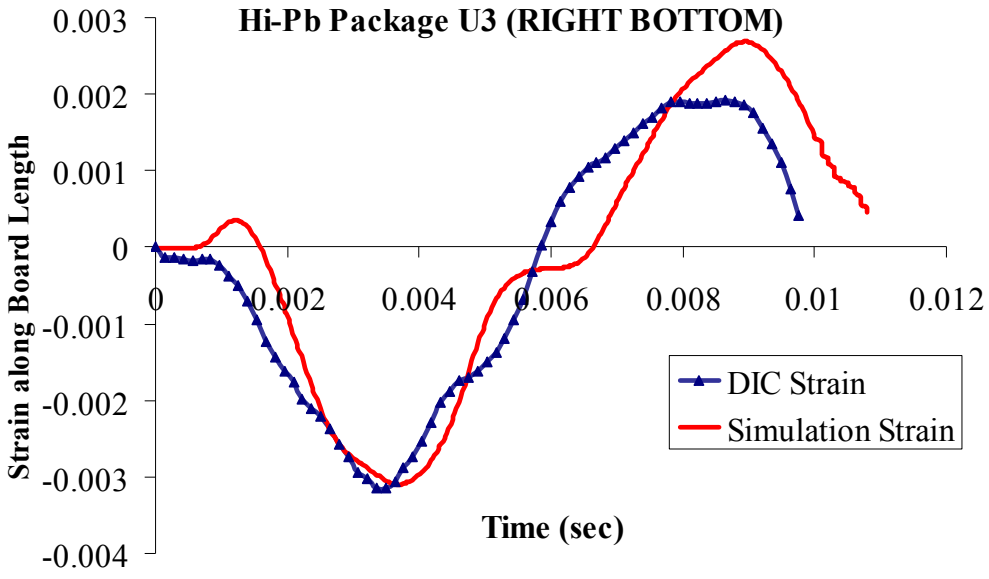

Figure 54: Strain Correlation between FE and DIC for 90Pb10Sn Solder Interconnect CBGA at U3 (Right Bottom)

Explicit finite element model predictions have been validated by full-field correlation of board strains with experimental measurements from digital image correlation. Figure 55 to Figure 58 show the transient mode-shapes and measured strain magnitudes during the drop event from simulation and experiment. Comparison shows that the similarity of the transient mode shape and strain distribution over the entire board assembly. Figure 55 to Figure 58 shows the full field strain distribution on PCB at different instances just after the impact.

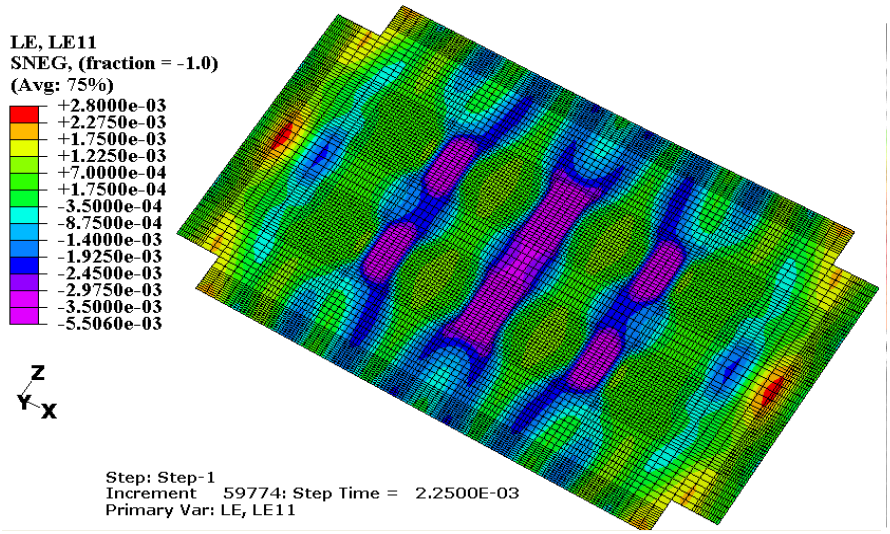

T=2.25 ms

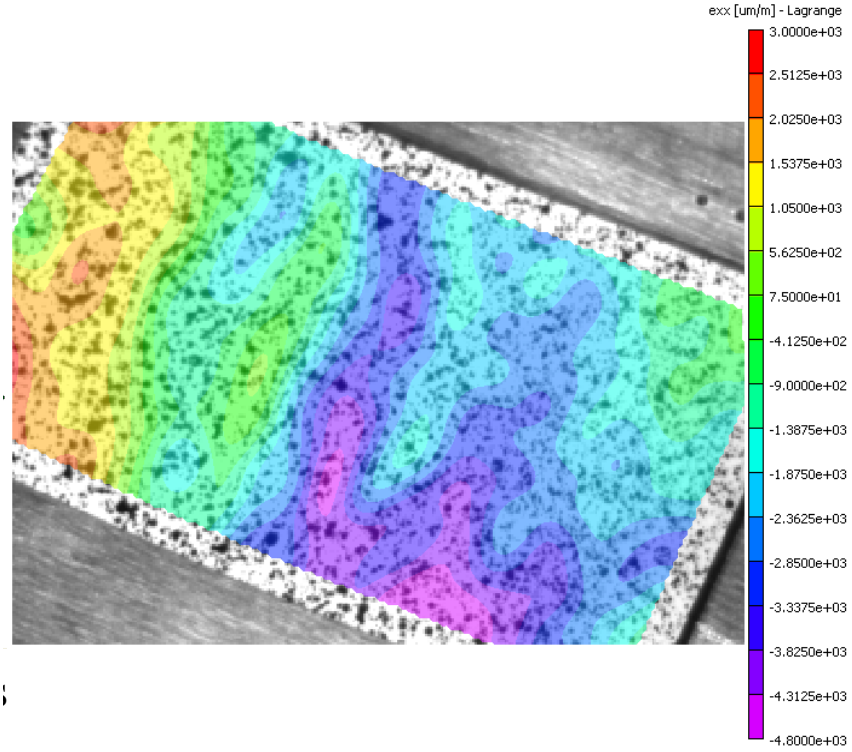

Figure 55: Transient strain contour correlation on PCB between DIC with high-speed imaging and FE analysis at 2.5ms

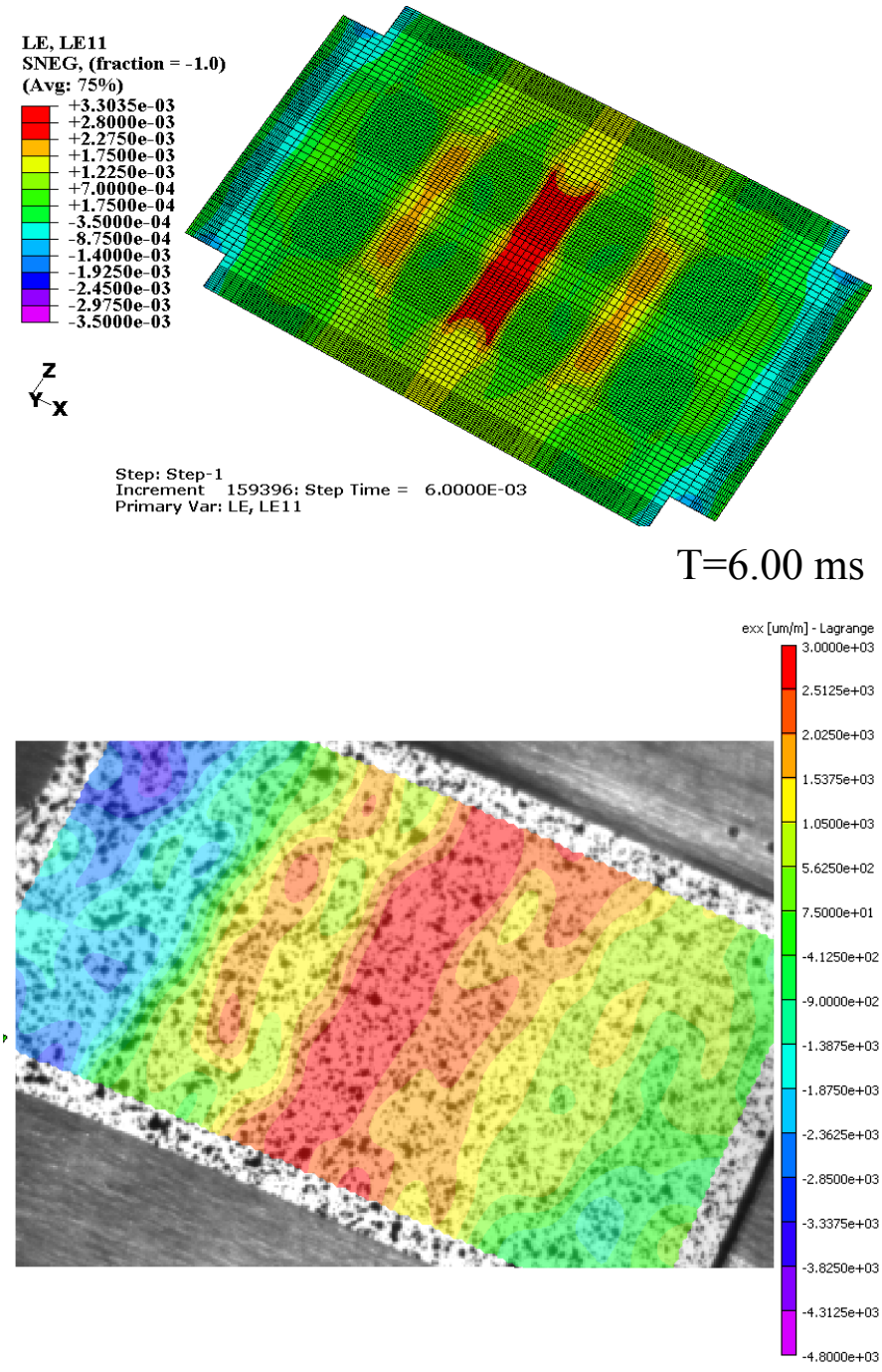

Figure 56: Transient strain contour correlation on PCB between DIC with high-speed imaging and FE analysis at 6ms

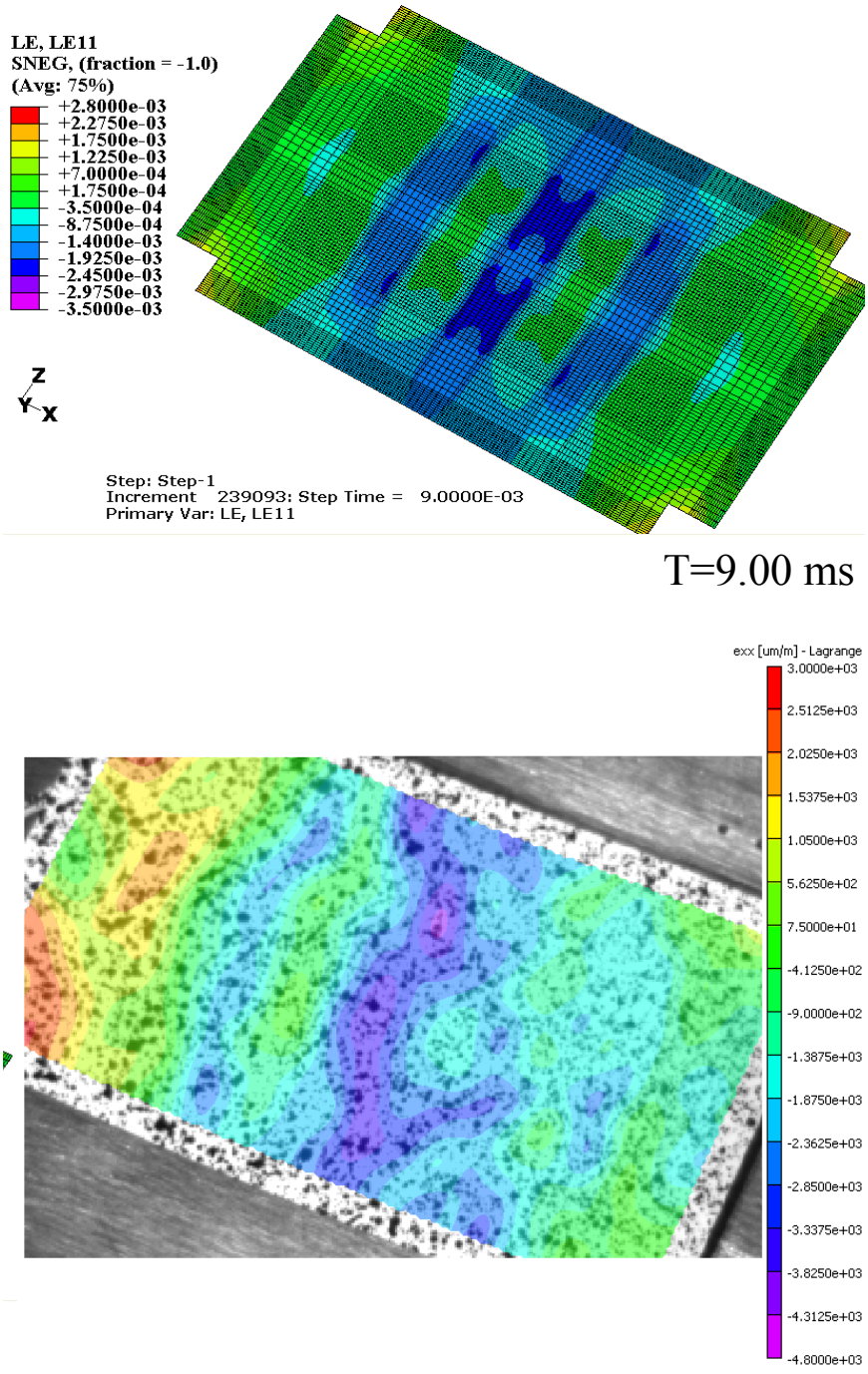

Figure 57: Transient strain contour correlation on PCB between DIC with high-speed imaging and FE analysis at 9ms

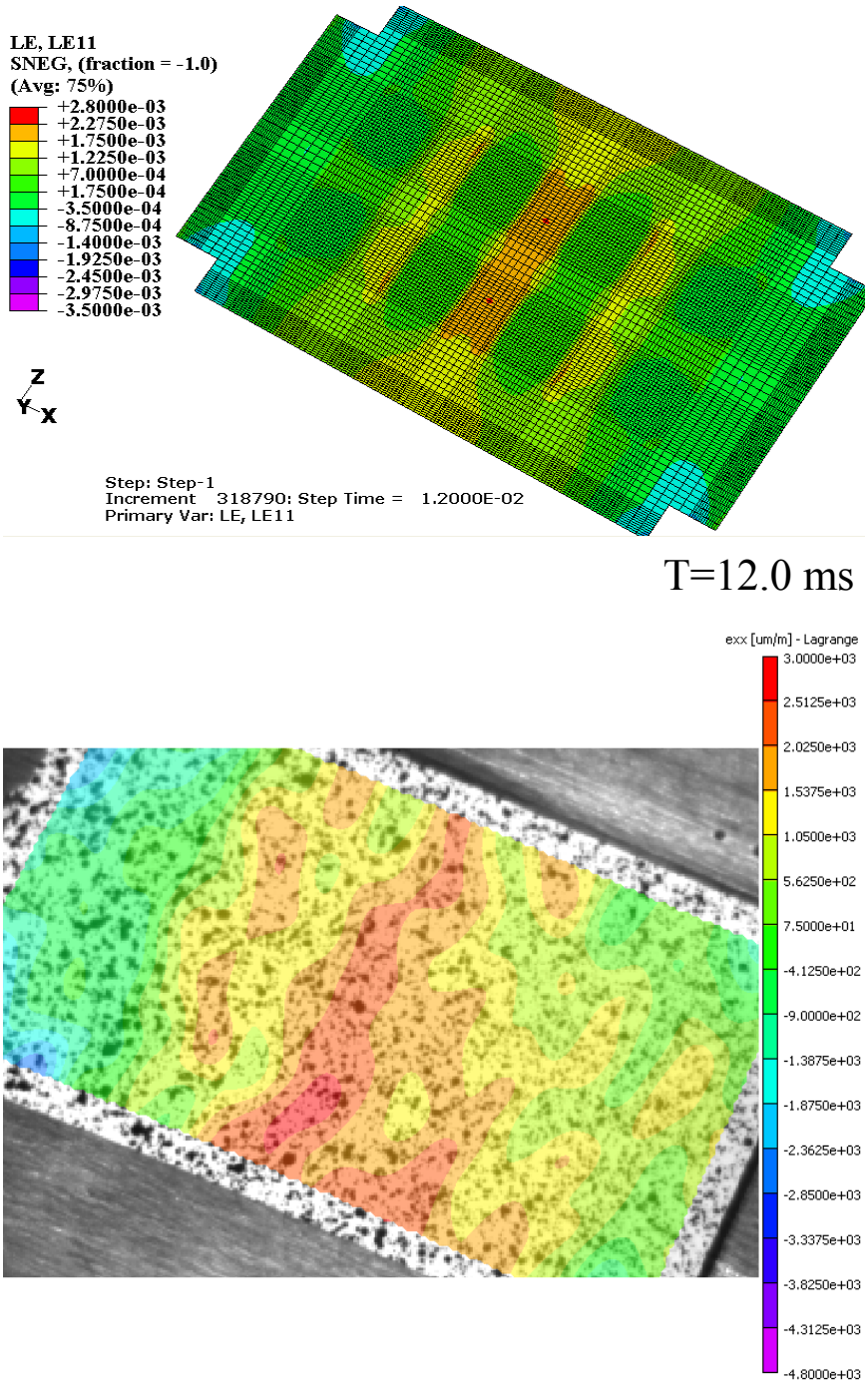

Figure 58: Transient strain contour correlation on PCB between DIC with high-speed imaging and FE analysis at 12ms

Board assemblies have been cross-sectioned after failure to understand the failure modes. Table 3 the correlation between the model predictions and the observed failure modes in board assemblies after failure in the shock test. The location of the failure modes correlate well with the experimental data. Copper columns fail close to the package interconnect interface. Sn3Ag0.5 Cu interconnects on the CBGA package fail close to the package-solder interface. Sn3Ag0.5 Cu interconnects on PBGA package fail close to board interface. 90Pb10Sn interconnects fail close to the board interface in the eutectic solder.

Table 3: Correlation of Model Predictions with Failure Modes from Experiment

Type	Model Predictions	Experimental Data
Cu-Column CBGA	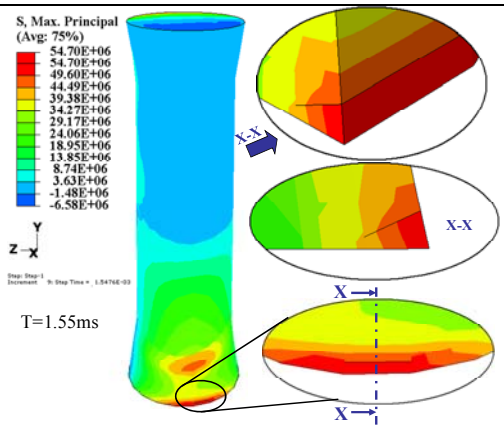	
Sn3Ag0.5Cu CBGA	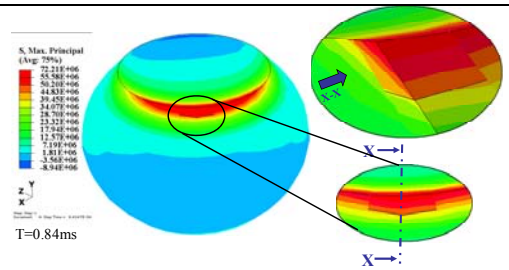	
90Pb10Sn CBGA	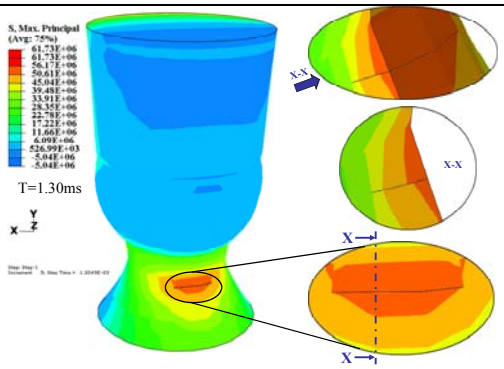	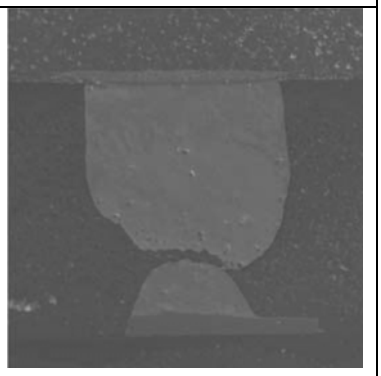
Sn3Ag0.5Cu PBGA	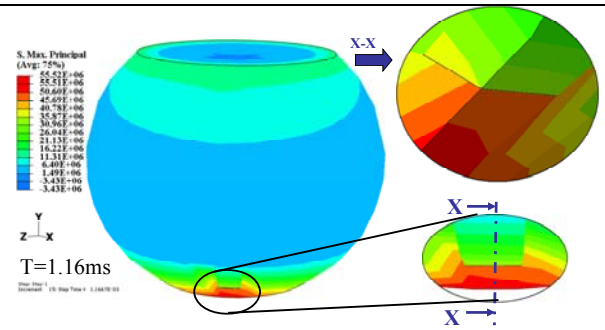	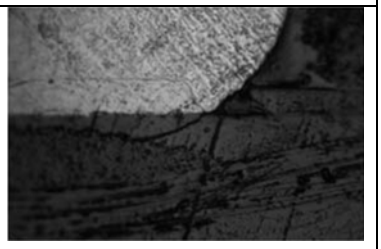

CHAPTER 5

SIF EVALUATION USING XFEM AND LINE SPRING MODELS UNDER HIGH STRAIN RATE ENVIRONMENT FOR LEADFREE ALLOYS

5.1 Introduction

Transition to Pb-free solder alloy system has brought many challenges in electronic industry. Behavior of these new alloys under dynamic conditions of shock and drop is not completely known. Intermetallic compounds of Cu_6Sn_5 and Cu_3Sn are commonly found at the interface of copper pad and solder in case of interconnects. These intermetallics affect the solder joint fatigue life and therefore the reliability of the system [Lall 2010[a], Limaye 2008]. Very minute size of these IMC layers in BGAs makes characterization of these compounds difficult. Therefore in this work, bimaterial copper solder specimens are tested using tensile tester with notch near interface where intermetallic compounds are formed. Stress intensity factor at this critical failure location is determined using both finite element models and experimental techniques. Finite element approach along with experimental testing methods is implemented to assess the reliability of leadfree solder alloys under range of strain rate conditions. Boundary conditions derived from experimental procedures are used to drive finite element models of crack propagation. Bimaterial copper-solder specimens are "V" notched at the center typical of bulk solder and copper pad of package interconnect. These specimens are

tested on uniaxial tensile tester. Finite element simulations of these specimens under tensile testing conditions fetch fracture properties such as SIF, J integral. This thesis addresses the need of testing leadfree alloys at strain rates similar to field applications. Here, specimens are tested for crack propagation study using a uniaxial tensile testing machine which allows high strain rates. Displacement fields in front of crack extracted using ultra high speed imaging are used to evaluate SIF at crack nucleation. This experimental SIF is well correlated with the SIF value determined using line spring finite element model. Bimaterial copper-solder specimens are fabricated with single notch and double notch of 30° at center interface. These specimens are tested at two high strain rate conditions of 20 per sec and 55 per sec. Stress-strain properties acquired during testing are used to build material models in line spring models and extended finite element models. In this paper, solder deformations and critical stress intensity factors are measured at strain rates representative of shock and vibration. Also, JEDEC form factor printed circuit board is tested on a shock tower at high g-level. Stress intensity factor at copper pad solder ball interface is studied in centrally mounted package on this board. Transient deformation of the board is studied with high speed cameras and high speed data acquisition systems. In this study DIC has been used to study crack propagation in single notch and double notch specimens under dynamic loadings. It has also been used to extract velocity vectors on PCBs subjected to drop testing. Relative motion of two ends of bimaterial specimens has been monitored during tensile testing using high speed cameras. The displacements and velocities tracked during these transient events are used to drive FE models. Attachment degrees of freedom of Line spring and XFEM models use these displacements and velocities as boundary conditions for simulation.

5.2 Specimen Fabrication

For the purpose of this study, bimaterial copper solder specimens are prepared using a novel procedure where solder uniaxial test specimens are formed in high precision rectangular cross-section glass tubes using a vacuum suction process. The solder is melted in a quartz crucible using a melting pot maintained at 242°C. Figure 59 shows the set-up for preparing the specimen.

Figure 59: Bimaterial Cu-solder specimen preparation set-up with control valve of vacuum pump

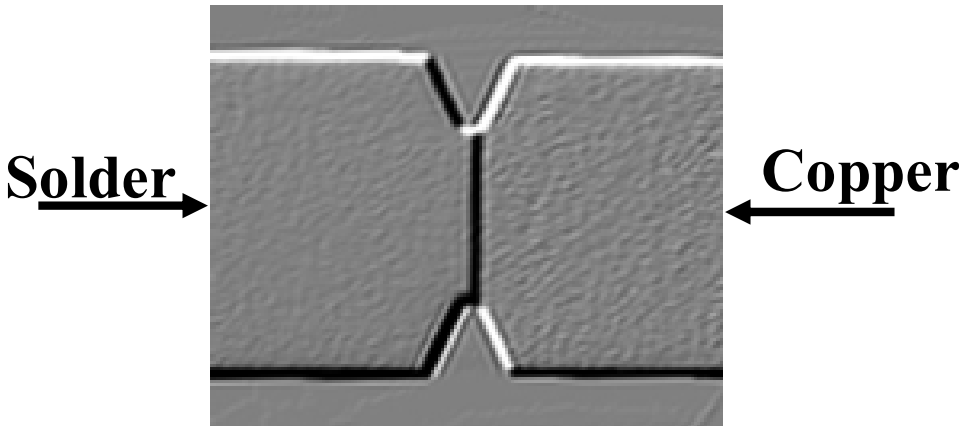

Figure 60: X-ray image of Bimaterial Copper Solder specimen for Sn3Ag0.5Cu

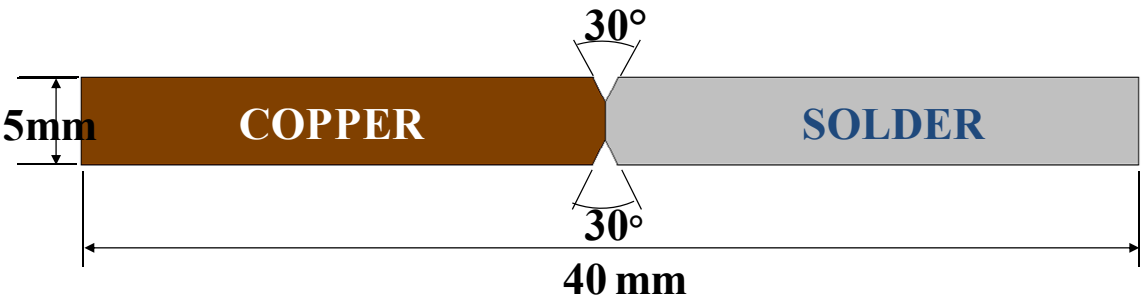

Figure 61: Schematic of Single Notched Bimaterial Specimen Geometry

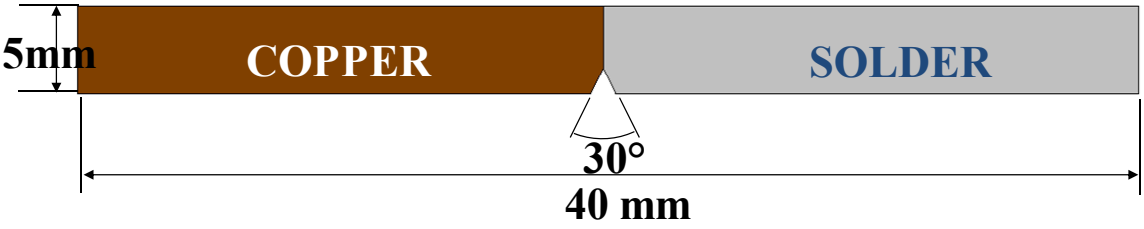

Figure 62: Schematic of Double Notched Bimaterial Specimen Geometry

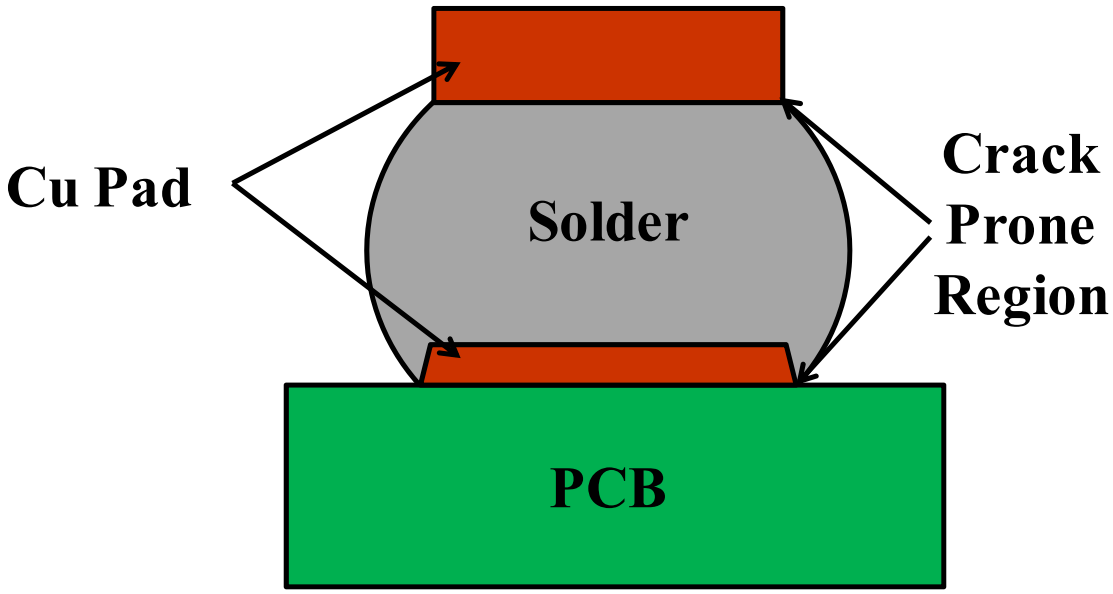

Figure 63: Schematic of typical Cu-Solder Interface in solder interconnect showing crack prone region

Figure 63 shows the X ray image of fabricated specimen showing homogenous interface of copper and solder. Parameters are controlled to avoid formation of voids in solder material. Figure 61 and Figure 62 shows schematic of fabricated single notched and double notched specimen. Bimaterial specimens are fabricated because this interface geometry resembles with the actual copper pad and bulk solder interface in solder interconnects as shown in Figure 63. Intermetallic compound is formed at this region which is a critical for a crack to nucleate and propagate [Lall 2010[a]].

Oxidized Copper material with 0.4mm thickness was inserted into glass tube up to half of its length. Specimen thickness is chosen to be representative of an actual joint. Other end of the glass tube was inserted into the molten solder which rises in the tube by capillary action, and additionally suction was applied to the other end via a rubber tube connected to the house vacuum system. The suction force was controlled through a regulator on the vacuum line. When desired amount of solder was drawn into the tube,

the glass tube is drawn out of solder pot and is held in a vertical position for cooling of solder. In this holding position cooling solder is on top of the copper strip where bottom end of copper strip is connected to vacuum pump. Therefore the weight of solder and the suction pressure act in the same direction avoiding formation of voids due to opposing forces. The tube was then cooled to room temperature (25°C) by air cooling. Temperature of specimen solder is recorded during cooling stage to study the cooling of solder during fabrication. Figure 64 shows the schematic of method implemented to record the temperature of solder specimen during cooling. Thermocouple is connected to a multimeter with data logging system.

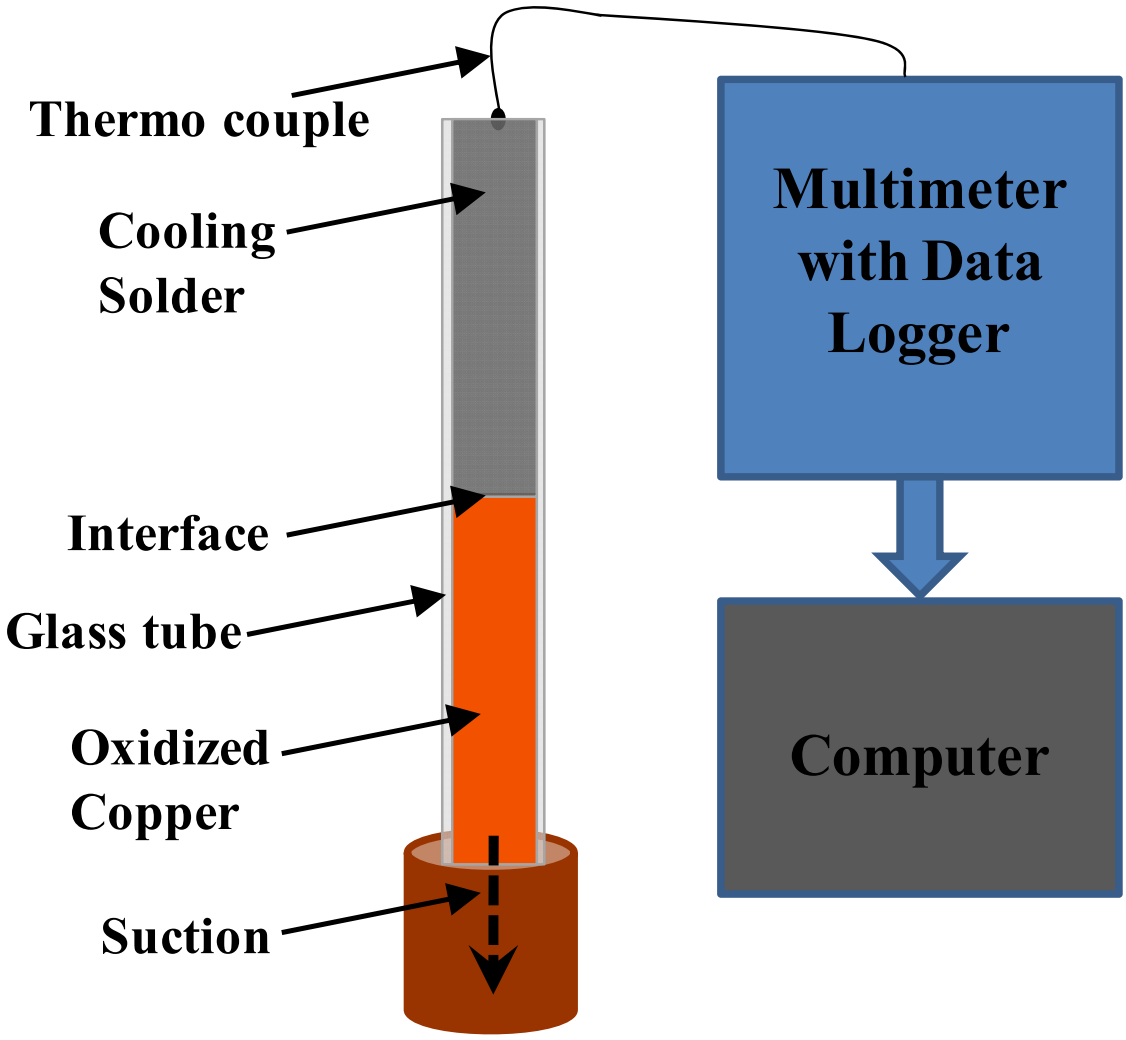

Figure 64: Schematic of recording of cooling profile for bimaterial copper-solder specimen during cooling stage

Figure 65 shows the comparison of recommended and actual observed cooling profile of specimen. Cooling part of the recommended reflow oven profile suitable for Pb-free alloys is compared with cooling profile of specimen. It can be seen that the rate of cooling of the specimen after fabrication is identical to the rate of cooling of solder interconnects during actual reflow of printed circuit boards. This plays an important role

in achieving similar grain structure and therefore material properties as observed in actual solder interconnects.

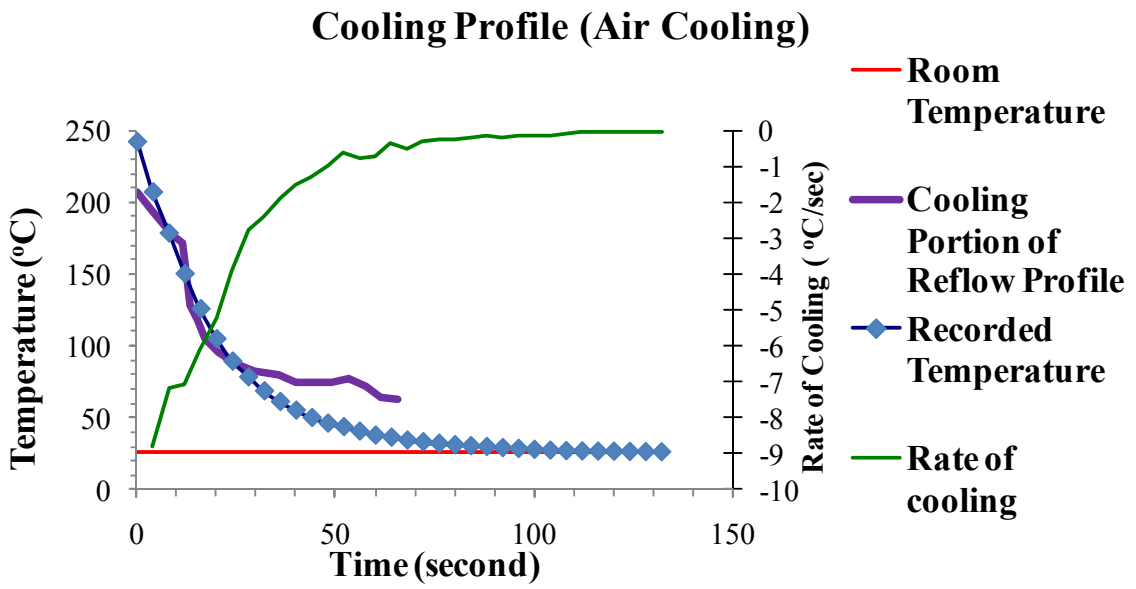

Figure 65: Comparison of recorded air cooling profile with industry recommended reflow cooling profile

The overlapped solder was then removed from the oxidized copper surface area. The solder-copper interface is purely edge-to-edge. 'V' notches were made along the interface using wire electronic discharge machine (EDM). The notch opening angle selected was 30^0. A flux was applied on copper in order to make a good joint during the casting process. These specimens were speckle coated from one side to capture DIC.

5.3 High speed Uniaxial Tensile testing

Bi-material copper solder specimens have been subjected to high strain rate tensile testing. Specimens are tested to a strain rate typical of shock and vibration. Uniaxial tensile testing machine as shown in Figure 66 is employed for this purpose. The bimaterial specimens were notched with a 30° 'V' notch at the interface typical of solder-copper interface in package interconnects. Two types of specimen are fabricated with

single notch and double notch. Single edge notched tension (SENT), double edge notched tension (DENT) specimens have been tested for steels to study effect of specimen geometry J integral [Landes 1972, Gross 1965]. Specimen is gripped between two crossheads using screws. A range of strain rates 1-100 s^{-1} has been achieved by controlling the impact hammer. Testing is continuously monitored by high speed cameras and high speed data acquisition systems.

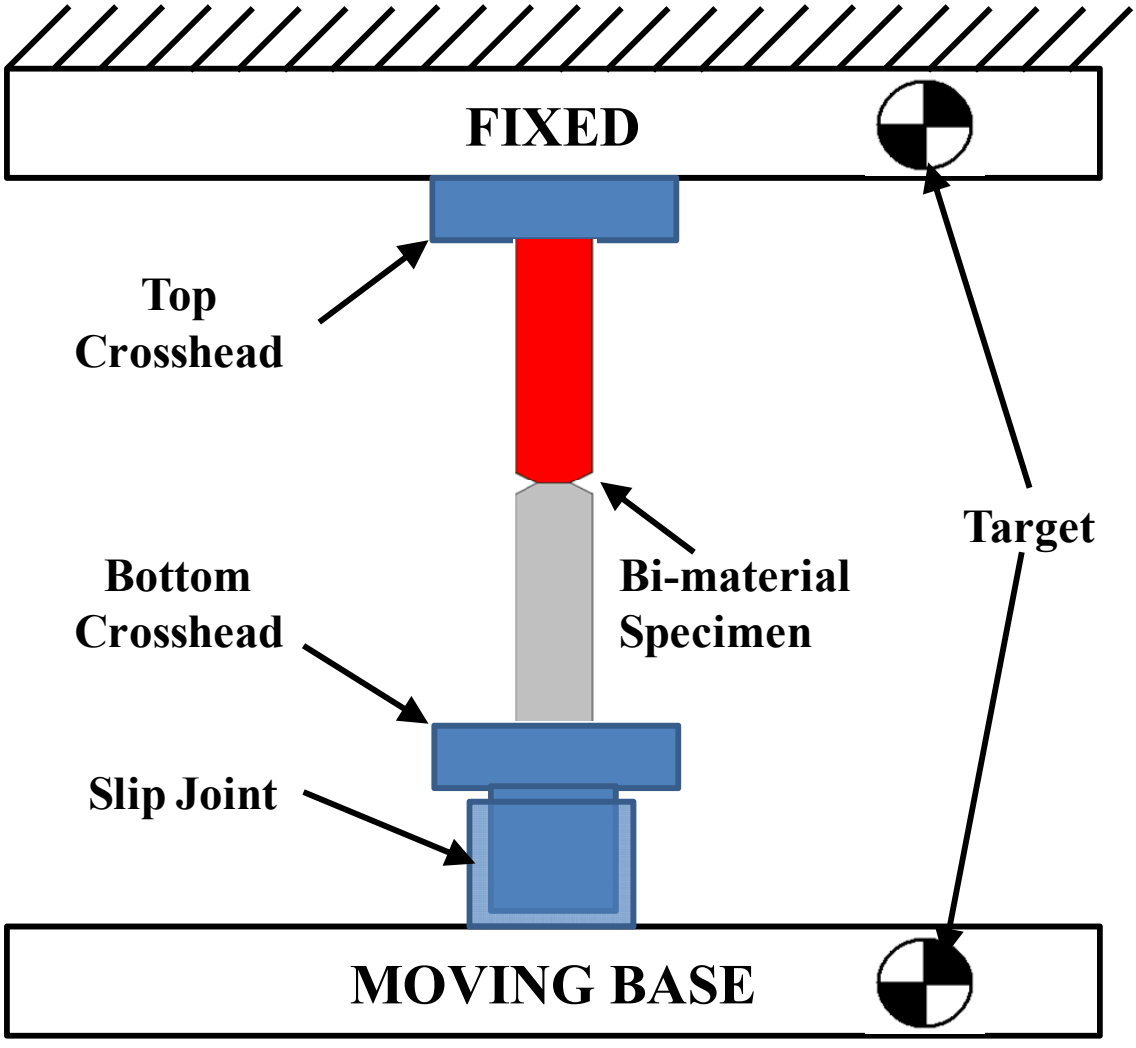

Figure 66: Schematic of uniaxial high strain rate tensile machine

Two targets are placed on a machine as shown in Figure 66. Top target is attached on a fixed plate while bottom target on a moving plate. Using high speed imaging

cameras motion of these targets is recorded. Slip joint is inserted between bottom crosshead and bottom plate in order to remove any noise and sudden jerk due to hammer impact. Displacement of bottom target with respect to top target gives the deformation of the specimen. Two different leadfree alloys with two strain rates are tested.

The load was monitored using ICP force sensor in conjunction with a high speed data acquisition system. The ICP force sensor uses a built-in MOSFET microelectronic amplifier to convert the high impedance charge output into low impedance voltage signal for recording. The low impedance voltage signal is not affected by tribo-electric cable noise or contaminations. The ICP sensor is powered from a separate constant current source. It is well suited for continuous, unattended force monitoring in harsh environment such as drop/impact conditions. Sensor is designed to measure impact force. The flat sensing surface is located on top of the sensor and is designed to measure force as it is applied axially. In this application of impact testing, as the impact hammer contacts the moving base of uniaxial tensile tester metal to metal impact produces high frequency ringing. Polyimide film tape covers cap surface of the sensor to reduce this effect. These sensors are constructed with compression mode quartz crystals preloaded in a rigid housing. These designs give the sensors microsecond response time and resonant frequencies in hundreds of KHz, with minimal overshooting or ringing. Small diaphragm diameter ensures spatial resolution of narrow shockwaves. Therefore, use of these sensors is perfectly suited for such high speed high strain rate loading application [PCB 2009].

5.4 Fracture Analysis of bimaterial Specimens

Line spring and XFEM models are used for determination of stress intensity factor and J integral at interface between copper and solder of bimaterial specimens.

Variation of SIF with solder alloys and strain rate has been measured. Single notched and double notched XFEM and line spring models are built. This stress intensity factor defines amplitude of crack tip singularity. It is one of the most important concepts in fracture analysis. J integral which is nonlinear energy release rate can be viewed as both energy parameter and a stress intensity parameter. It is a path independent contour integral for analysis of crack. J integral is a more general version of the energy release rate. For case of bimaterial tensile testing condition with linear elastic material [Anderson 2005],

$$J = \frac{K_I^2}{E'} \tag{5.1}$$

Node based modeling technique has been implemented to provide boundary conditions to these models. Here global output extracted from experimentation has been used to drive attachment degree of freedom of FE models. These attachment degrees of freedom are the driven nodes in the simulation. Figure 68 shows the methodology used while simulating these models. Relative displacement vectors measured from experimentation are given at the bottom edge of the solder part of model. Top edge in copper region is constrained which resembles the fixed base of the uniaxial tensile tester. In order to achieve sufficient element density at the expected crack region, multipoint constraints are implemented. MPCs help in defining fine mesh at the interface region. Central interface of Cu-solder bimaterial specimens is critical from failure point of view. Therefore, maximum number of elements is needed in this region of possible failure. With use of MPC, it is possible to achieve finer discretization of elements at desired region resulting optimum mesh density. Coarse mesh is acceptable in the region away from interface. This method is computationally efficient and memory economical.

Multipoint constraints (MPC) allow constraints to be imposed between different degrees of freedom of the model. Linear and quadratic type multi-point constraints are used here to achieve higher element density near interface of two materials [Abaqus 2009c].

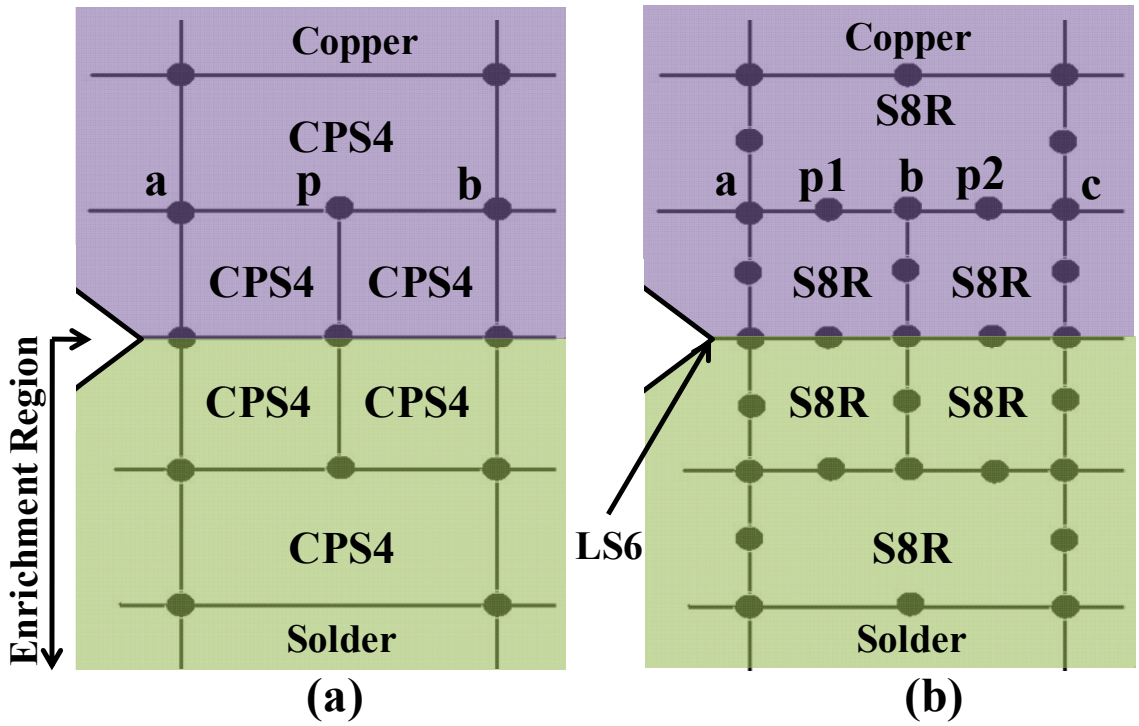

Figure 67: Linear (a) and Quadratic (b) MPCs used in XFEM and Line Spring models respectively

Figure 67 (a) shows linear MPCs used for plane stress CPS4 elements of XFEM model. Each degree of freedom at point p is interpolated linearly from the corresponding degrees of freedom at nodes a and b. Entire solder region of bimaterial specimen is modeled as enrichment domain. In case of line spring models, second order shell elements S8R are used to construct the models. Quadratic mesh refinement is implemented for these second order elements. Here, as shown in Figure 67 (b) each degree of degree of freedom at node p1 and p2 are alternately interpolated quadratically from corresponding degrees of freedom at nodes a, b and c. Line spring elements are

modeled near the root of a notch at interface. Element types used for every part of both Line spring and XFEM models is given is Table 4. As 2nd order line spring LS6 needs to be aligned with shell element, therefore line spring models are constructed with S8R shell elements. Figure 69 and Figure 70 show the detailed zoomed in view of these models for single notched and double notched geometry.

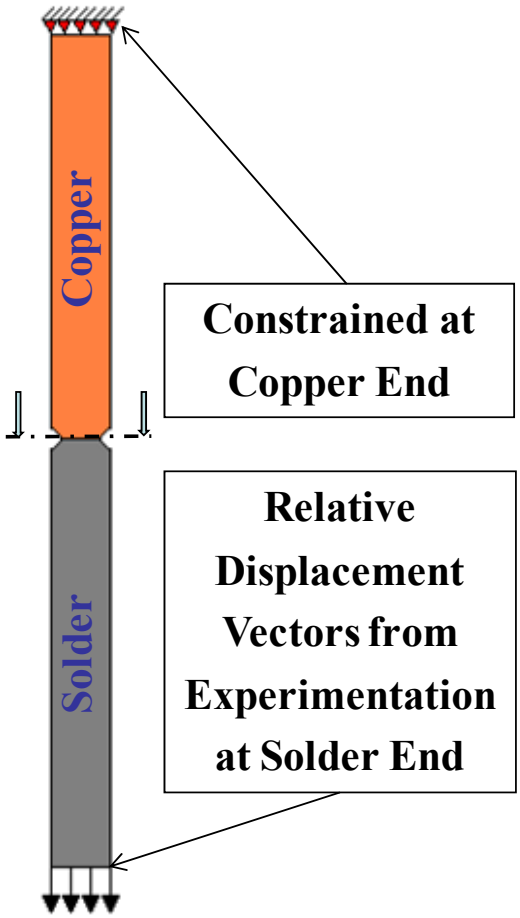

Figure 68: Line Spring model and XFEM Methodology for Bimaterial specimen tensile testing

Table 4: Element types used for FE models created for copper-solder bimaterial specimens

Element Types	Copper	Solder
Line Spring Model	S8R	S8R
XFEM Model	CPS4	CPS4

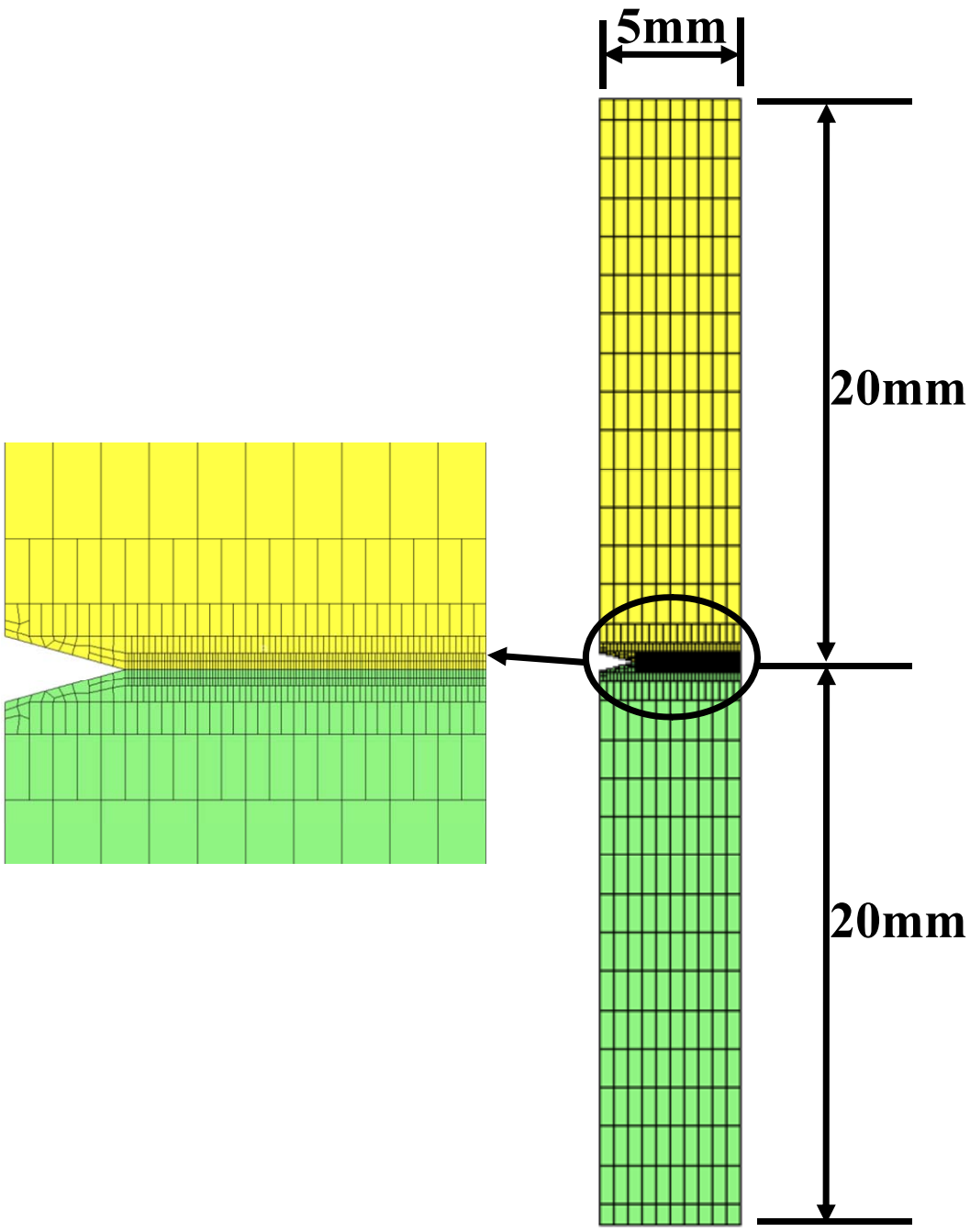

Figure 69: FE models of Single Notch Bimaterial specimens with MPCs

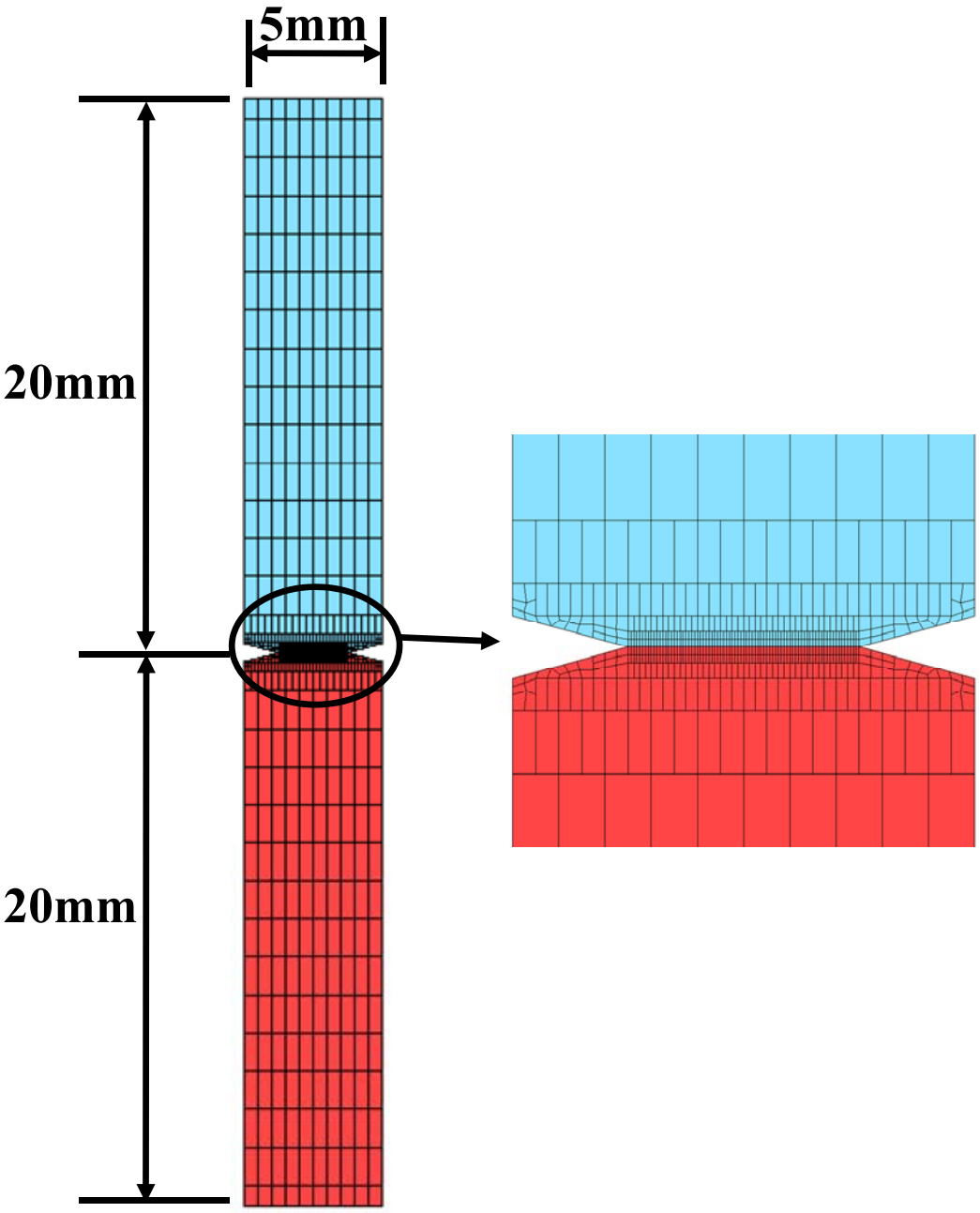

Figure 70: FE models of Double Notch Bimaterial specimens with MPCs

For these simulations, classical metal plasticity material models are used in conjunction with linear elastic models. These models use Mises yield surfaces which allows isotropic yield. The Mises yield surfaces assume that yielding of the metal is independent of the equivalent pressure stress [Abaqus 2009d]. Yielding of the solder

material is observed at the crack tip of notched specimen under high strain rate condition. Material model is defined by giving the value of uniaxial yield stress as a function of uniaxial equivalent plastic strain. Uniaxial yield stress and uniaxial equivalent plastic strain is measured from stress-strain curves shown in Figure 71 for Sn1Ag0.5Cu and Figure 72 for Sn3Ag0.5Cu plotted for corresponding strain rates (20 per sec and 55 per sec) using uniaxial tensile tester [Lall 2011]. Figure 73 shows the representative constitutive model of elastic-plastic material defined for Sn1Ag0.5Cu and Sn3Ag0.5Cu under experimentally tested strain loading conditions. Total strain in solder is composed of plastic strain and elastic strain.

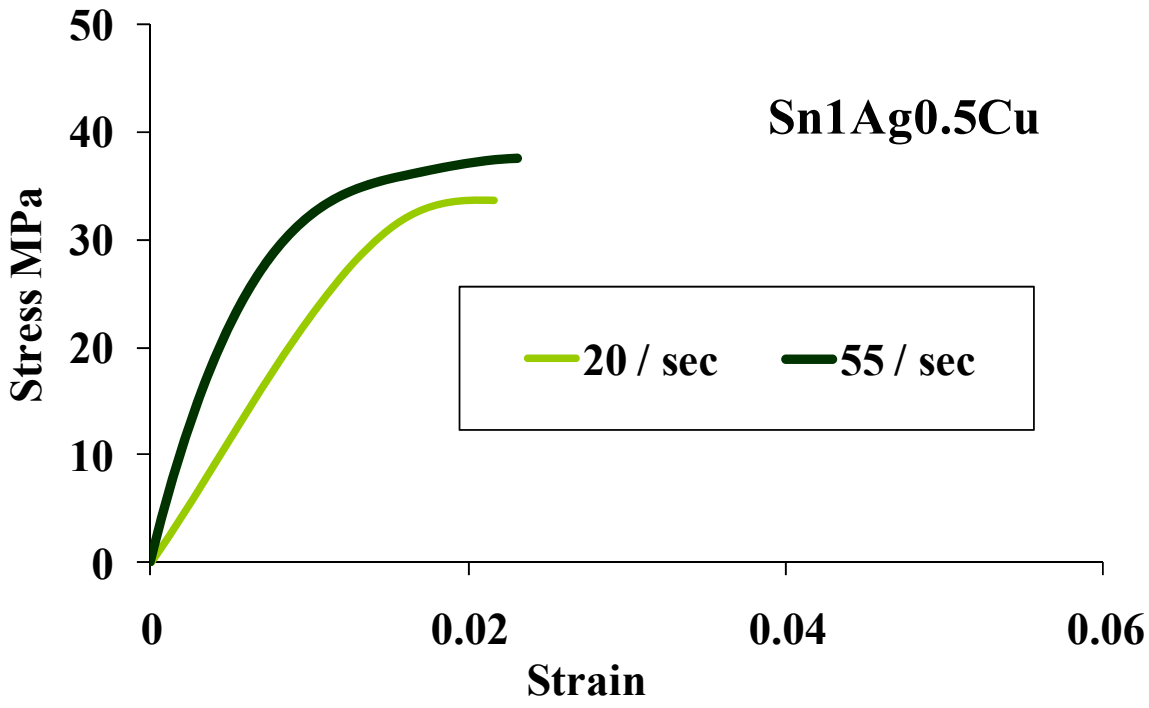

Figure 71: Stress-Strain curve plotted for Sn1Ag0.5Cu for strain rates of $20s^{-1}$ and $55s^{-1}$ [Lall 2011]

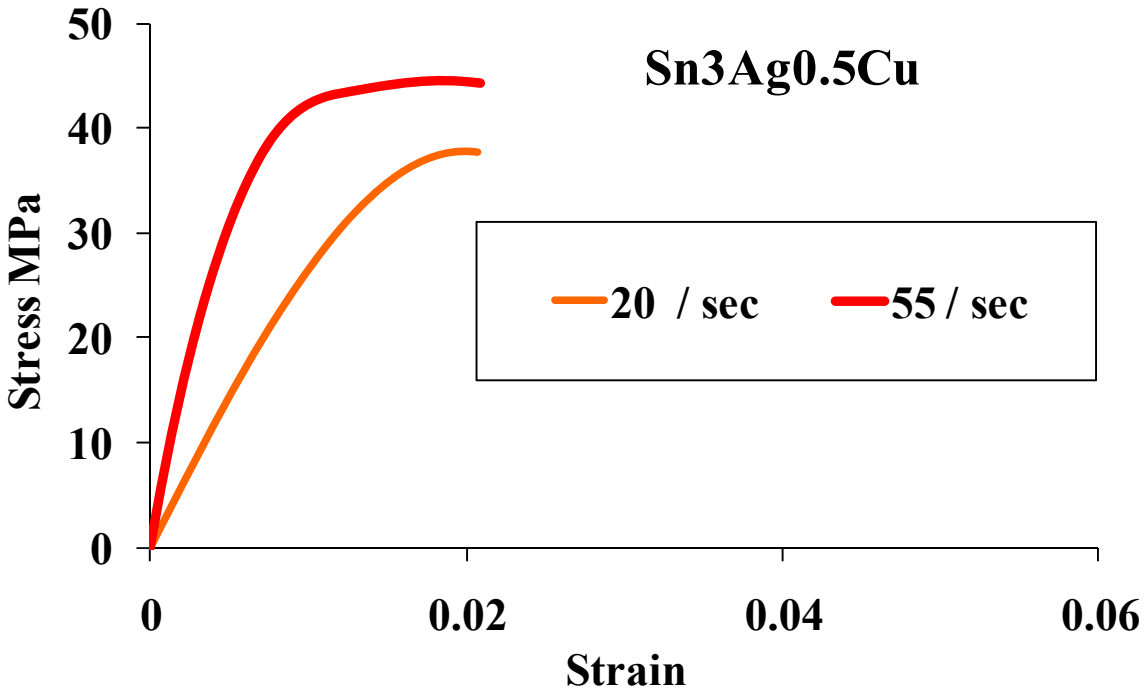

Figure 72: Stress-Strain curve plotted for Sn3Ag0.5Cu for strain rates of $20s^{-1}$ and $55s^{-1}$ [Lall 2011]

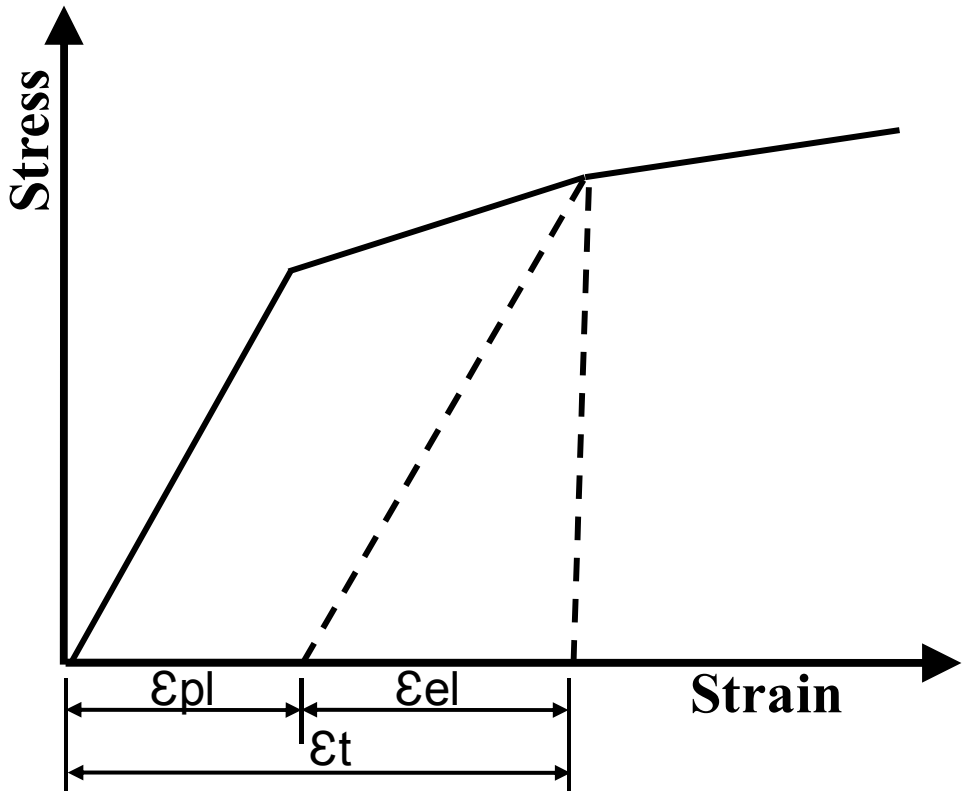

Figure 73: Schematic of simulation elastic-plastic material model developed for Sn1Ag0.5Cu and Sn3Ag0.5Cu

To evaluate fracture properties of solder, two crack/flaw models of extended finite element and line spring models are simulated for each case as described below:

(a) Extended Finite Element Model:

Initially XFEM model is simulated until the crack initiates and starts propagating. Entire solder region is enriched with additional degrees of freedom as specimen is expected to fail in weak solder portion. Instead of embedding the discontinuity/crack at experimentally observed location, damage criterion is defined for model. As this criterion is met crack nucleates and travels to the neighboring elements. For both cases of single

notch and double notch geometry, failure has been observed at root of the notch. This region is same as experimentally observed location of crack. Critical time at which crack starts initiating and opening is extracted for each alloy and each strain loading condition using XFEM models. Crack opening displacement is also measured for this critical time. This crack domain is defined with material models developed from experimentation. For a case Sn3Ag0.5Cu alloy with single notched bimaterial specimen, Figure 74 shows that crack initiates at 29µs after pull and later propagates in the neighboring elements. Initiation of deformation shows a stress concentration at the root of notch. Critical time duration and critical crack opening displacement is recorded for these conditions. These XFEM models use displacement boundary conditions derived from experimentation.

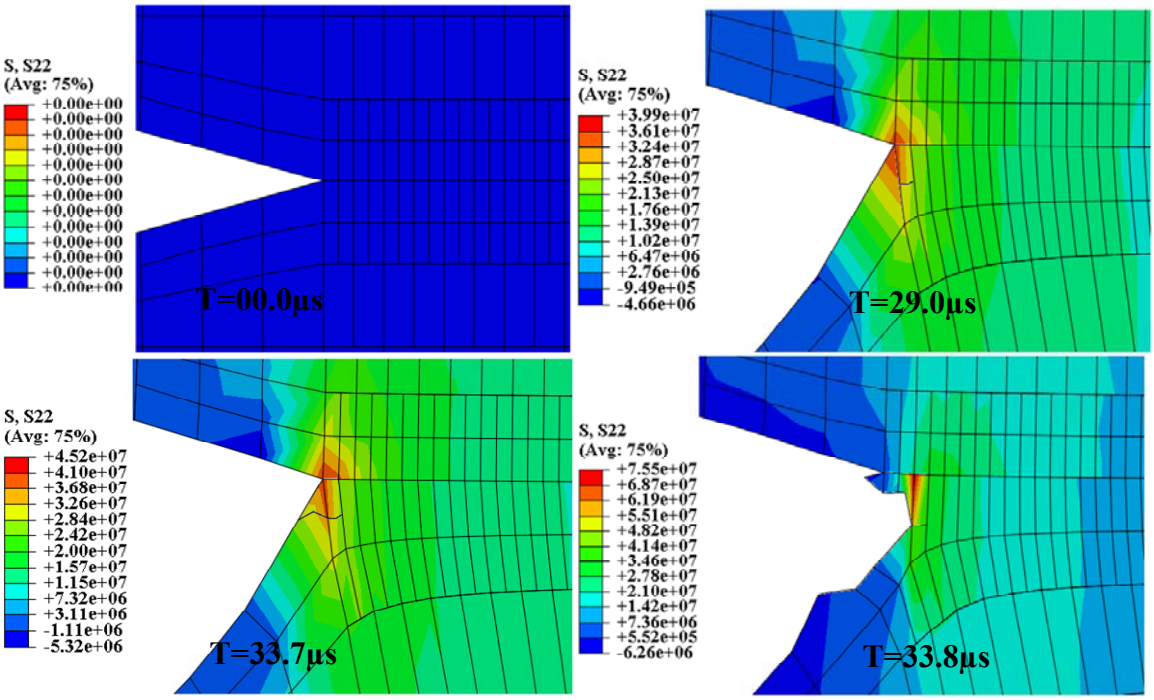

Figure 74: Crack Initiation and propagation in Bimaterial Cu-solder specimen of Sn3Ag.0.5Cu under 20 /sec strain rate

(b) Line Spring Model:

Line Spring models are built with second order shell elements. Second order 1D LS6 element is given a flaw depth as critical crack opening displacement measured from XFEM simulation. Line spring model is simulated for a critical time duration extracted from XFEM models. Therefore critical SIF can be evaluated from these line spring models. Figure 75 shows line spring model output for Sn3Ag0.5Cu specimen under 20 per sec strain rate. LS6 elements at crack tip show critical value of SIF at tip of crack.

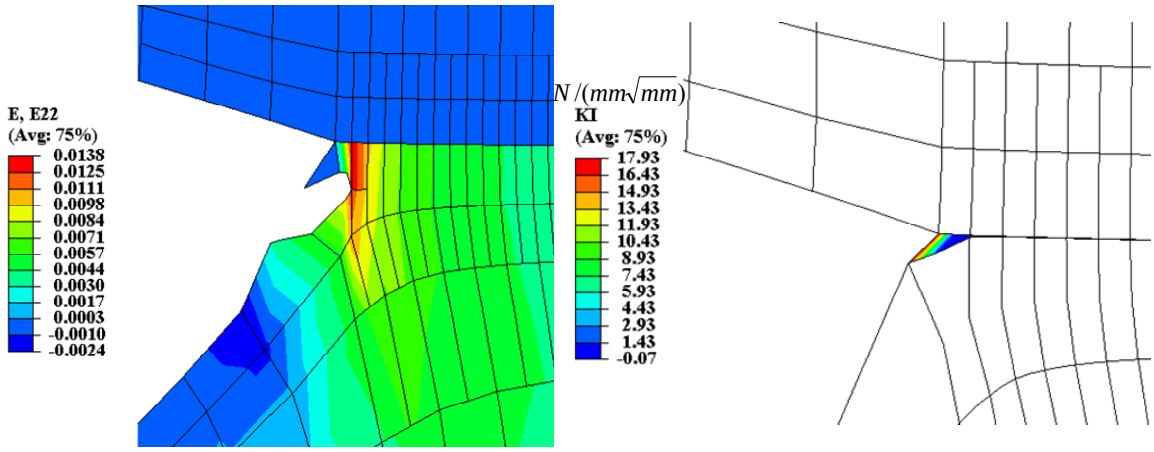

Figure 75: Critical SIF for Sn3Ag0.5Cu measured from line spring model with input from XFEM model under 20 per sec strain rate

Similar models are constructed and analyzed for both single notched and double notched bimaterial specimens. Stress-strain properties obtained from experimentation of Sn3Ag0.5Cu and Sn1Ag0.5Cu alloy systems are fed to extended finite element models and then to line spring models. Figure 76 and Figure 77 show that at strain rate of 55 per sec SIF value for double notched and single notched bimaterial specimen does not show much difference. This is expected because [Gross 1965], SIF measurement capacity for single edge notch and off center pin loaded specimens in tension is not sensitive to the eccentricity of loading. It can be seen that SIF value does not show much variation

between Sn1Ag0.5Cu and Sn3Au0.5Cu alloys for lower values of strain rate of 20 per sec. SIF increases with increase in strain rate. For both cases of single notch and double notch cases Sn3Au0.5Cu has higher SIF compared to Sn1Au0.5Cu at 55 per sec strain rate.

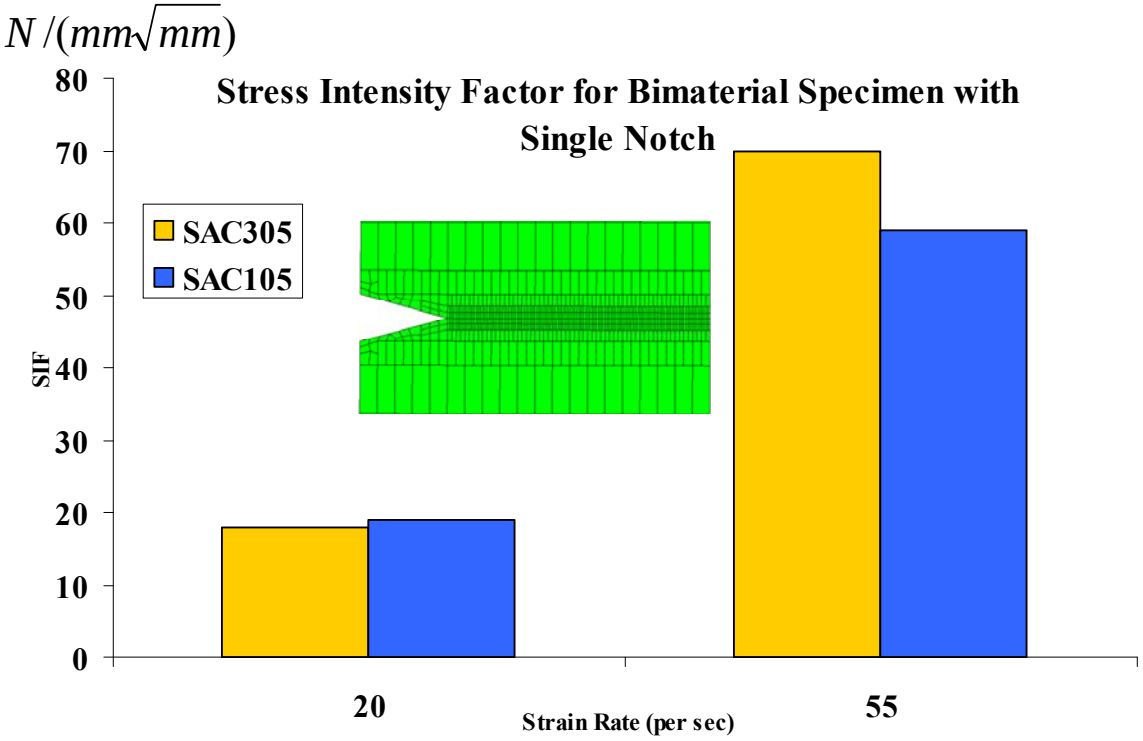

Figure 76: SIF comparison for single notched bimaterial specimen of Sn3Ag0.1Cu and Sn1Ag0.5Cu

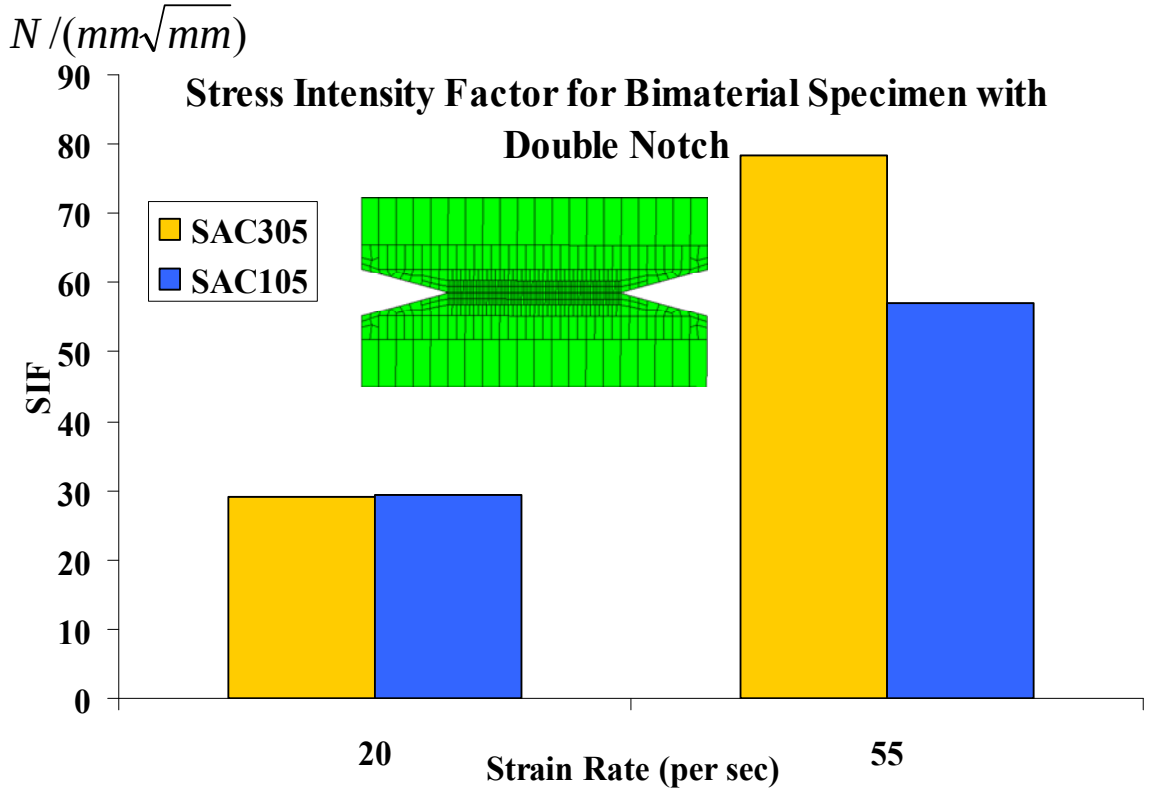

Figure 77: SIF comparison for double notched bimaterial specimen of Sn3Ag0.5Cu and Sn1Ag0.5Cu

5.5 Model Validation

Failed specimens have been studied using optical microscope after the tensile test. Interface region of the Sn3Ag0.5Cu solder shows formation of intermetallic compound due to bond with copper region of bimaterial specimen as shown in Figure 78. All bimaterial specimens failed at the interface as crack initiated at the root of the V notch and propagated along the intermetallic layer of interface.

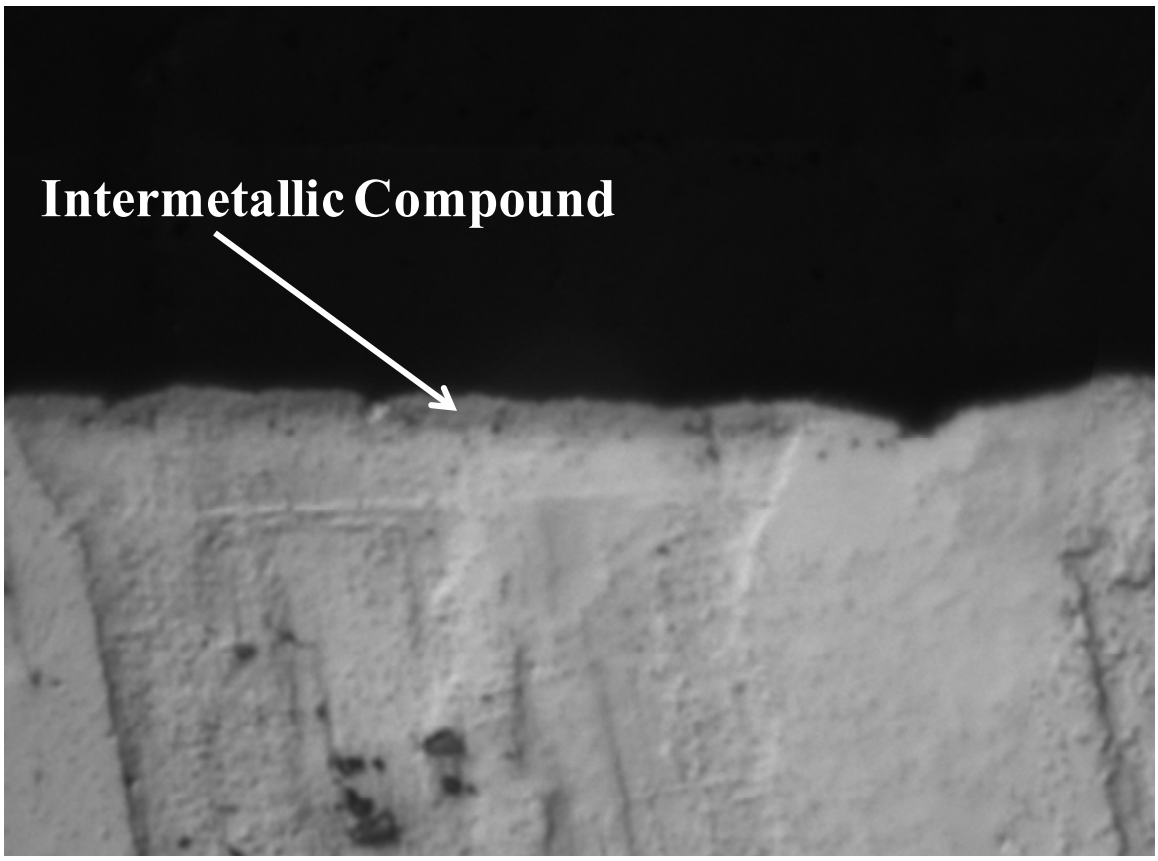

Figure 78: Optical Microscopic image of solder region of bimaterial Sn3Ag0.5Cu specimen showing IMC at interface

Digital image correlation enables measurement of full field strain, displacement and velocity on the entire area of the specimen. High speed imaging at 320,754 makes study of crack nucleation and travel of crack possible. Displacement of bottom crosshead is tracked with respect to fixed top crosshead using motion analysis of targets on tensile tester. After complete displacement of slip joint deformation of specimen initiates. Closer look at images of interface shows (Figure 79) nucleation and development of crack with time. Final frame of this experimental high speed imaging in Figure 79 shows copper and solder parts are completely separated. Strain along the length of the specimen extracted from both experimentation and XFEM simulation has been compared to validate the

accuracy of the approach. Strain values with respect to time are extracted at number of locations on the specimen. Along with contours, these strain magnitudes are compared statistically between experimentation and simulation. Figure 80 to Figure 83 shows the transient strain magnitudes and FE predicted strain at various time steps after impact on moving base of uniaxial tensile tester. Comparison shows similarity of strain contours over entire specimen area. The strain induced in copper part of the specimen is lower compared to solder region during entire event. At the root of the crack plastic behavior of solder material is observed. Therefore, strain contours near notch shows higher strain along length of the specimen. This plastic region starts growing as the bottom crosshead moves downwards and material starts deforming. DIC contours in Figure 83 shows that the interface is on the verge of separation resulting in the failure of specimen. Strain extracted in the plastic region shown in Figure 84 indicates nonlinear behavior of the material.

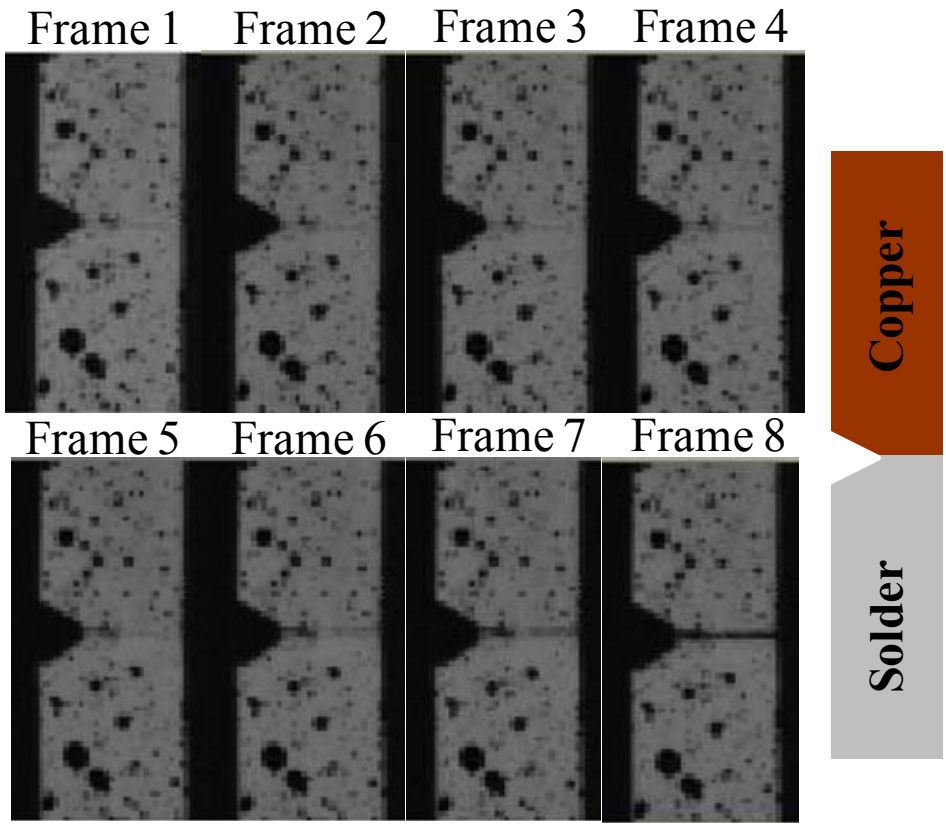

Figure 79: Crack Initiation and propagation in bimaterial Cu-solder specimen of Sn3Ag0.5Cu under strain rate of 20 per sec captured using ultra high speed imaging at 320,754 frames per second.

Figure 84 shows correlation between strain at the crack location extracted during simulation and DIC for bimaterial specimen of Sn3Ag0.5Cu with single notch pulled at 20 per sec. This strain Eyy is variation of strain magnitude along length of specimen with time. Correlation matrix in Table 5 shows strong statistical correlation (0.5<<0.9915) between strain vectors from simulation and DIC at crack location. Figure 85 and Table 6 give strain magnitude correlation at point P2 away from cracked notch on the same specimen in the solder region.

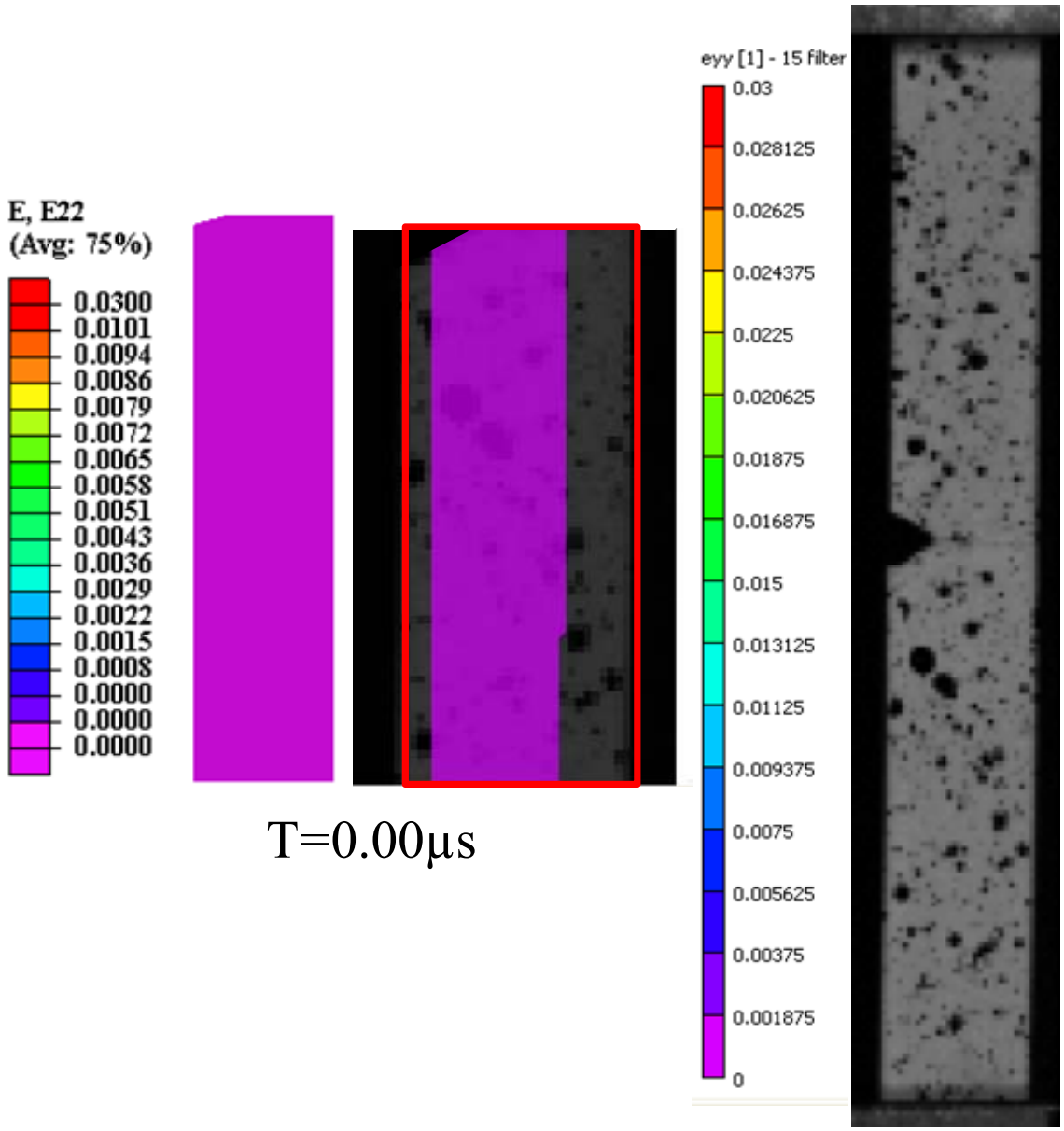

Figure 80: Transient strain contour correlation on Single notched Sn3Ag0.5Cu specimen between DIC with high speed imaging and FE at 0.00µs

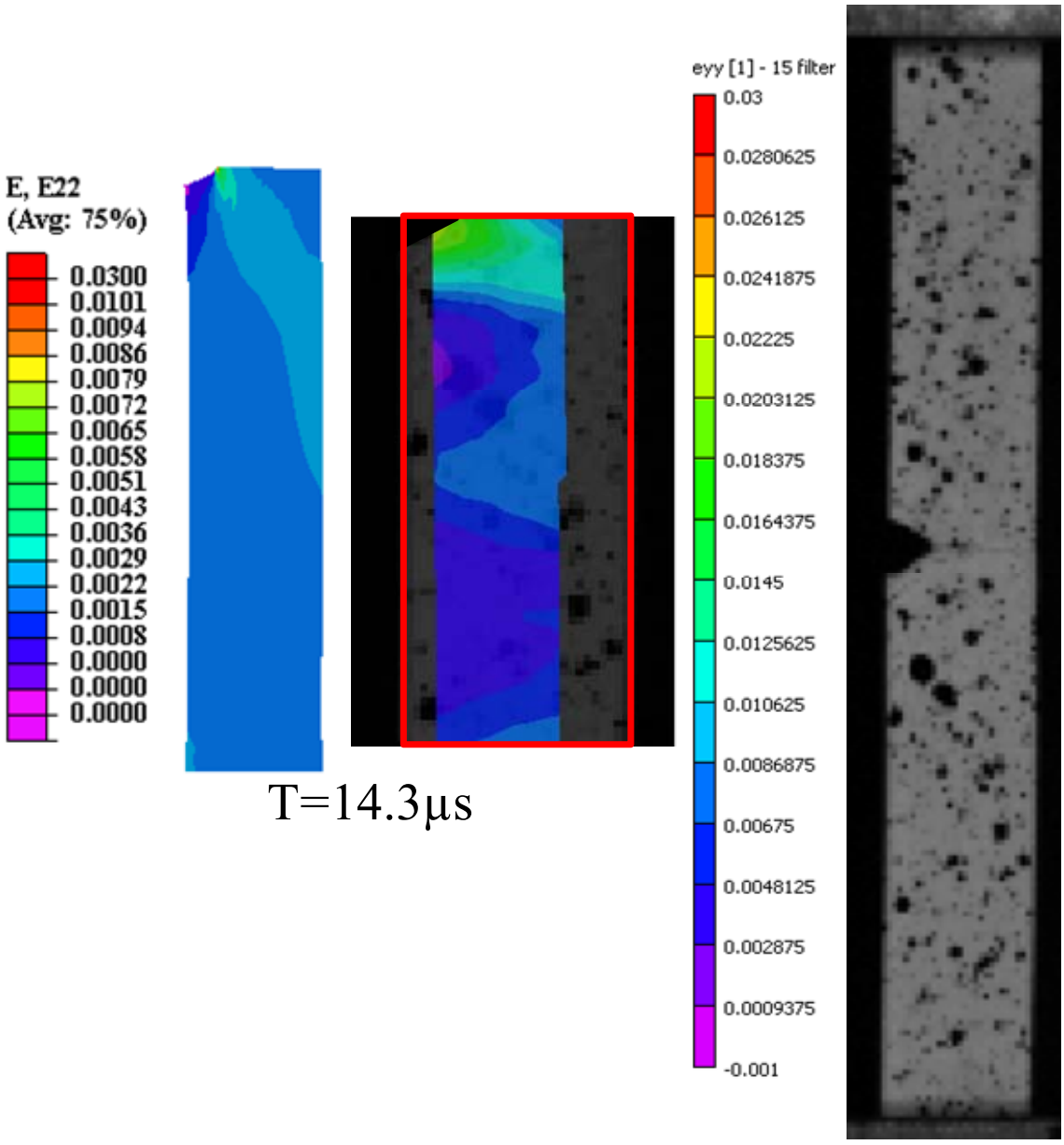

Figure 81: Transient strain contour correlation on Single notched Sn3Ag0.5Cu specimen between DIC with high speed imaging and FE at 14.3µs

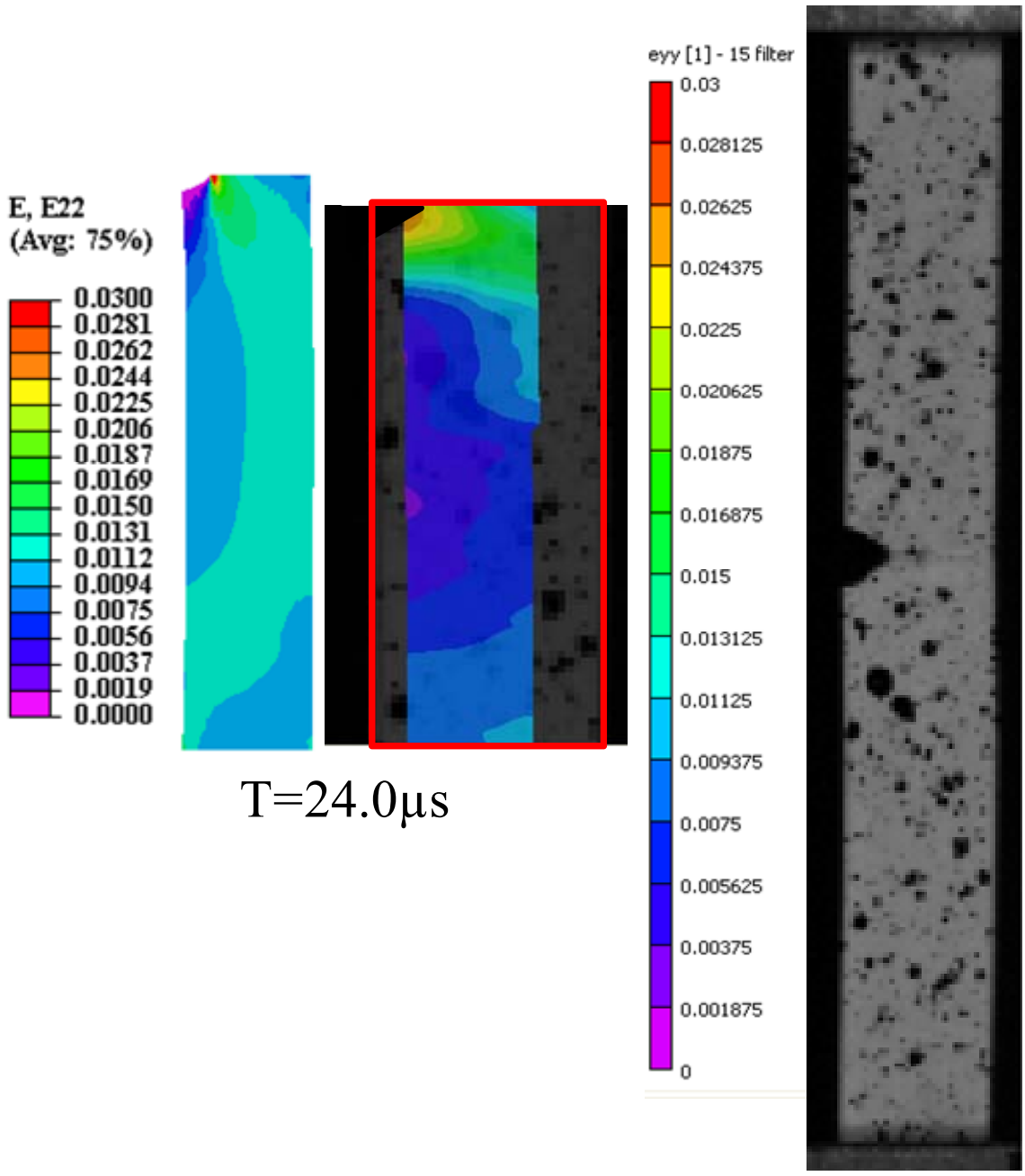

Figure 82: Transient strain contour correlation on Single notched Sn3Ag0.5Cu specimen between DIC with high speed imaging and FE at 24.0µs

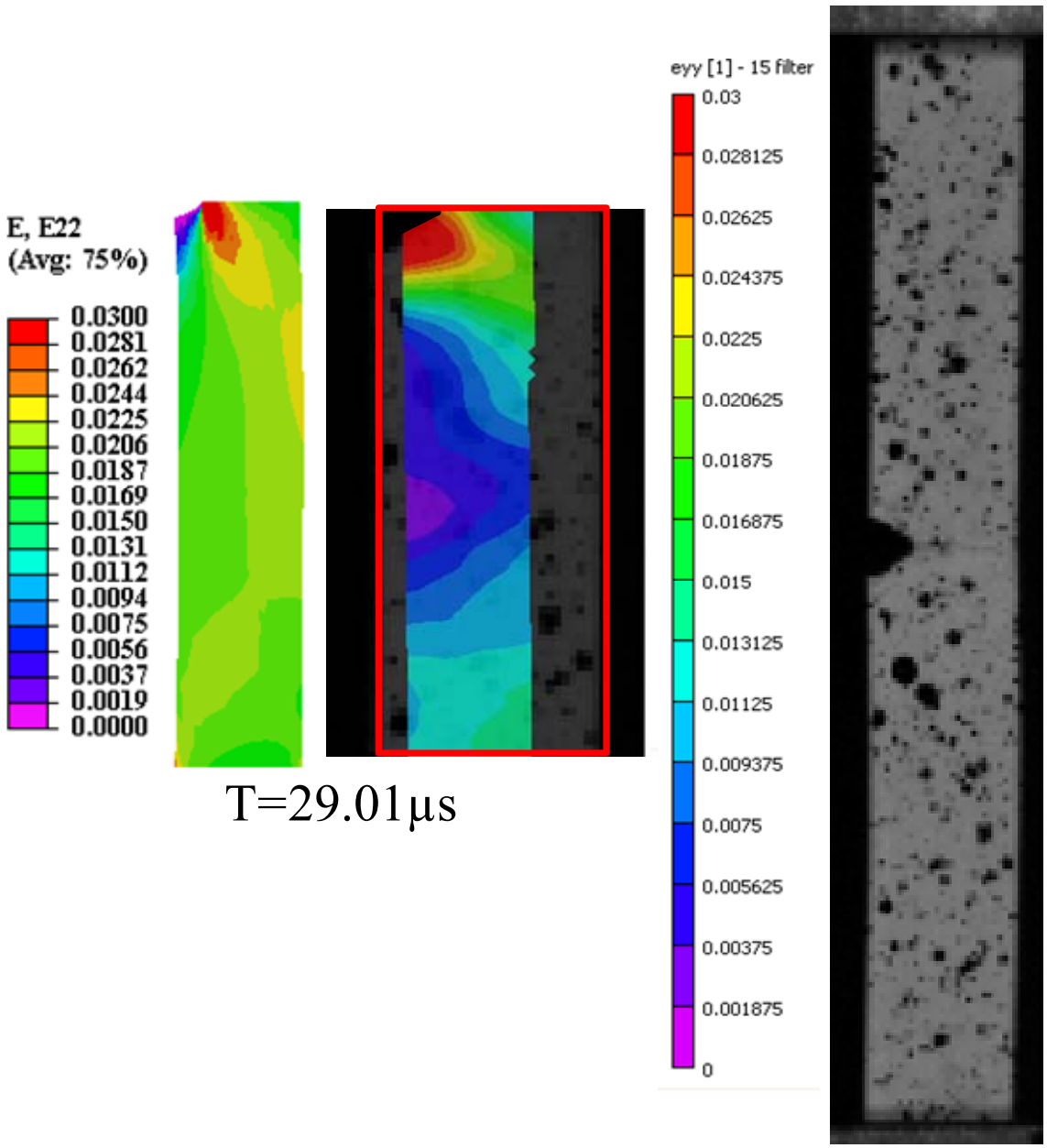

Figure 83: Transient strain contour correlation on Single notched Sn3Ag0.5Cu specimen between DIC with high speed imaging and FE at 29.01µs

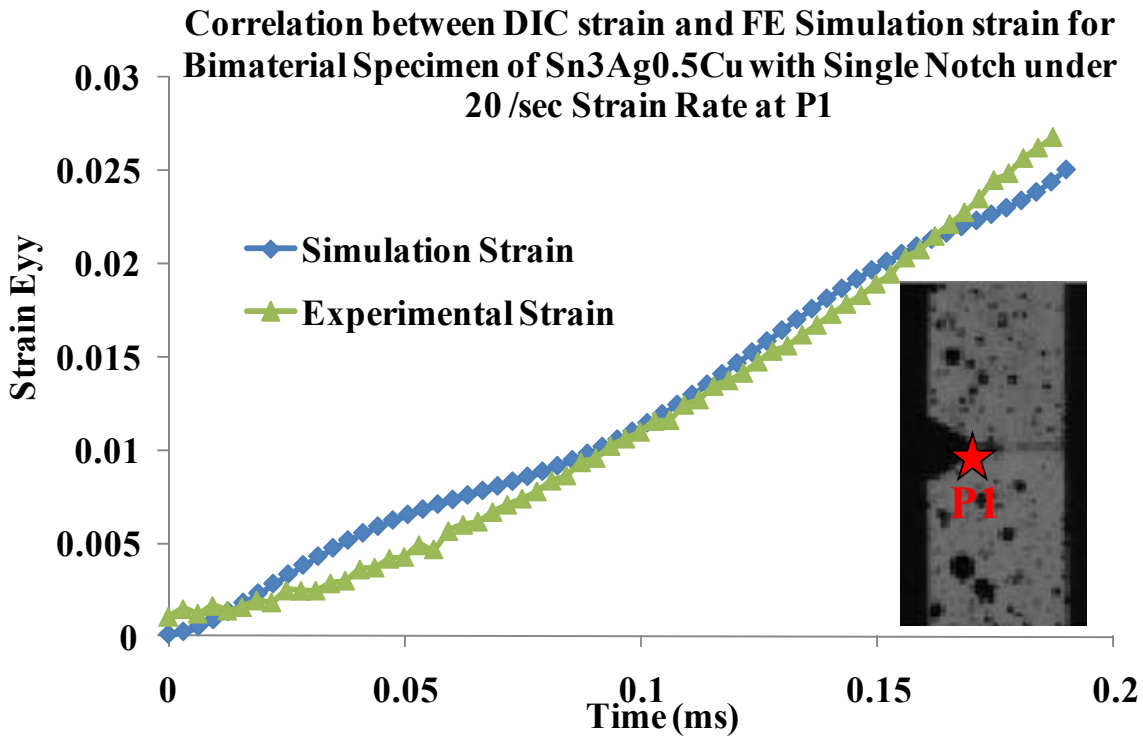

Figure 84: Strain correlation at Point P1 between DIC and XFEM simulation

Table 5: Statistical correlation matrix of strain vectors extracted at point P1 near crack initiation location

Correlation Matrix For Point P1		Strain Eyy	
		Simulation	Experimental
Strain Eyy	Simulation	1.0000	0.9915
	Experimental	0.9915	1.0000

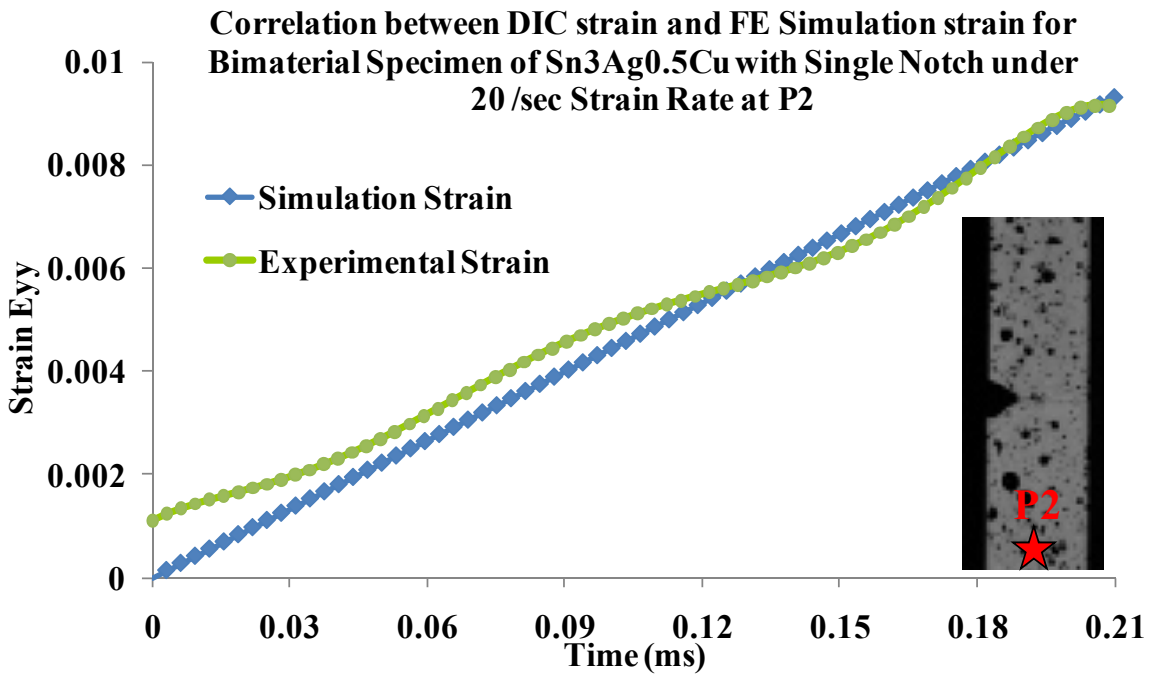

Figure 85: Strain correlation at Point P2 between DIC and XFEM simulation

Table 6: Statistical correlation matrix of strain vectors extracted at point P2 away from crack

Correlation Matrix For Point P2		Strain Eyy	
		Simulation	Experimental
Strain Eyy	Simulation	1.000	0.993
	Experimental	0.993	1.000

5.6 Experimental SIF determination

[Limtrakarn 2010] proposed a method to compute stress intensity factor in opening mode and shearing mode.For linear elastic fracture mechanics (LEFM), stresses are related to stress intensity factor by following relations [Williams 1957],

$$\sigma_x = \frac{1}{\sqrt{2\pi r}}\left[\begin{array}{l} K_I \cos\frac{\theta}{2}\left(1-\sin\frac{\theta}{2}\sin\frac{3\theta}{2}\right) \\ -K_{II}\sin\frac{\theta}{2}\left(2+\cos\frac{\theta}{2}\cos\frac{3\theta}{2}\right)\end{array}\right] \quad (5.2)$$

$$\sigma_y = \frac{1}{\sqrt{2\pi r}}\left[\begin{array}{l} K_I \cos\frac{\theta}{2}\left(1-\sin\frac{\theta}{2}\sin\frac{3\theta}{2}\right) \\ +K_{II}\sin\frac{\theta}{2}\cos\frac{\theta}{2}\cos\frac{3\theta}{2}\end{array}\right] \quad (5.3)$$

$$\tau_{xy} = \frac{1}{\sqrt{2\pi r}}\left[\begin{array}{l} K_I \sin\frac{\theta}{2}\cos\frac{\theta}{2}\cos\frac{3\theta}{2} \\ +K_{II}\cos\frac{\theta}{2}\left(1-\sin\frac{\theta}{2}\sin\frac{3\theta}{2}\right)\end{array}\right] \quad (5.4)$$

Here,

K_I: Stress intensity factor for opening mode (Mode I)

K_{II}: Stress intensity factor for tearing mode (Mode II)

r and θ Distance and angle in polar coordinate system as shown in Figure 86.

σ_x Normal stress in X direction

σ_y Normal stress in Y direction

τ_x Shearing stress

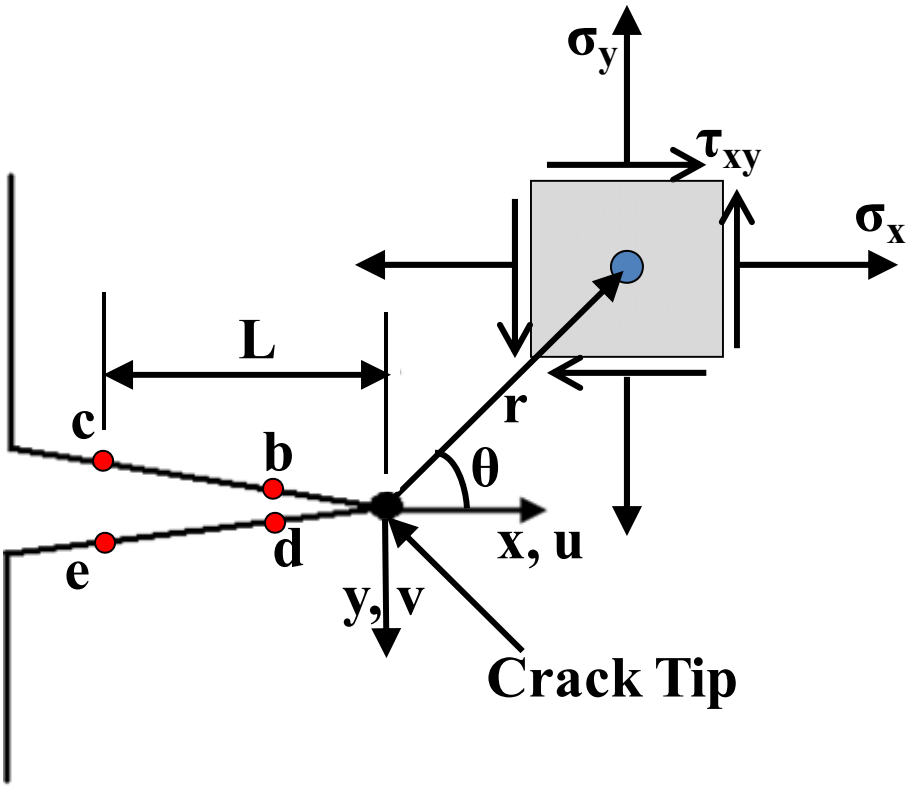

Figure 86: State of stress in polar coordinates from crack tip

Generalized form of stress intensity factor at the crack tip is given by [Limtrakarn 2005],

$$K = F\sigma_{\infty}\sqrt{\pi a} \qquad (5.5)$$

Here, F is the geometry factor which depends on dimensions, σ_{∞} is far-field stress and a is the crack length.

The opening stress intensity factor K_I can be computed from displacement extrapolation at points b, c, d and e as shown in Figure 86 [Limtrakarn 2010]. Points b, c, d, e are location near crack tip. Using high speed imaging technique of DIC, displacements u and v along x and y directions can be measured. These displacement vectors are extracted till nucleation of crack.

$$K_I = \frac{E}{3(1+\upsilon)(1+k)}\sqrt{\frac{2\pi}{L}}\left(4(V_b - V_d) - \left(\frac{V_c - V_e}{2}\right)\right) \qquad (5.6)$$

where, E is modulus of elasticity

υ is poisson's ratio

k= (3- υ)/(1+ υ) for plane stress condition.

Figure 87 shows the 'v' displacement plots for point b, c, d and e along 'y' direction for bimaterial single notched case tested with 20 per sec strain rate.

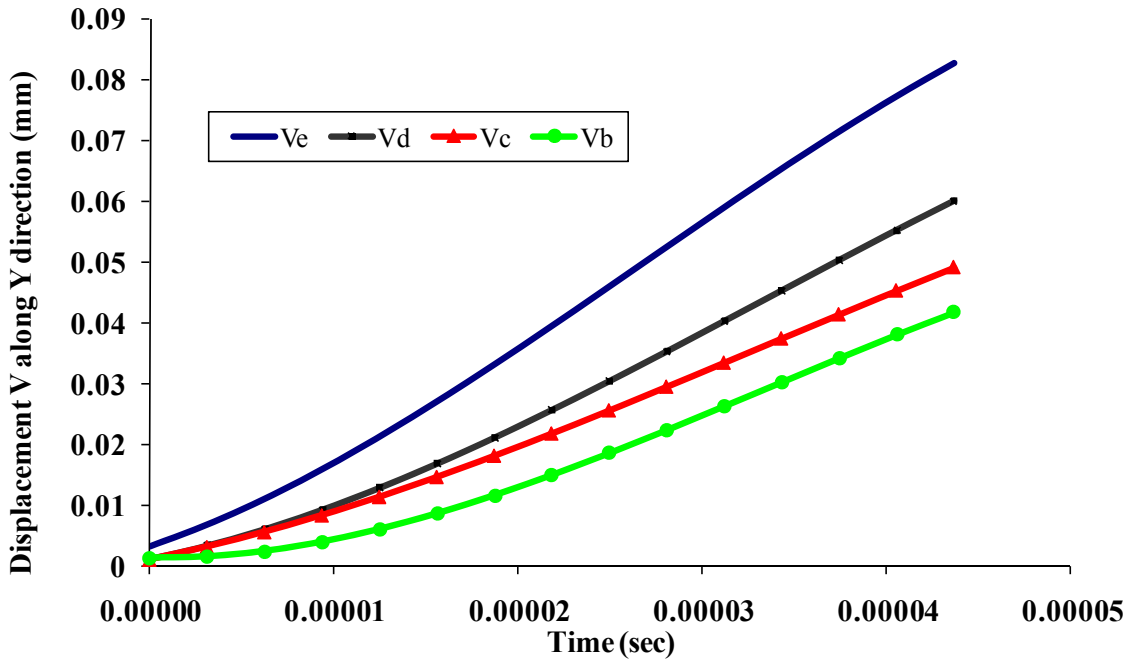

Figure 87: Displacement V plots at points near crack tip

Form equation (5.6) stress intensity factor for opening mode I for Sn3Ag0.5Cu alloy under strain rate of 20 per sec, K_I is calculated to be 19.82 $N/(mm\sqrt{mm})$. For identical conditions of simulation line spring models predict SIF K_I as 17.93 $N/(mm\sqrt{mm})$. Thus, it can be seen that simulation method shows strong correlation with experimentally measured value as shown in Figure 88 with error of 9.5%.

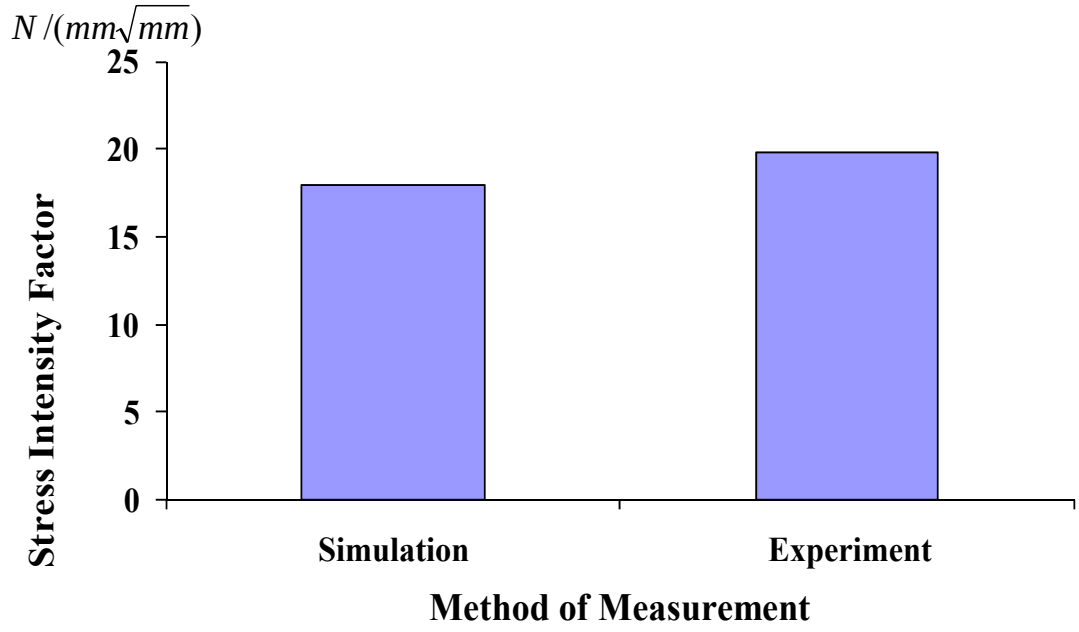

Figure 88: Correlation of opening mode stress intensity factor between line spring model and experimentally measured

5.7 Use of Line Spring FE Models for BGA Under Mechanical Shock

Finite elements models are created for plastic packages with two different alloy systems namely SAC105 and SAC305. Line spring element technique discussed previously has been implemented in order to extract fracture properties at interconnect failure region. Time dependent Stress intensity factor and J integral values at interface between solder ball and copper pad region are measured in drop simulation at high g loading conditions. Test vehicle used for this purpose has a centrally mounted single package of PBGA324. Package attributes are shown in Table 7.

Table 7: Package Architecture for PBGA324

Parameter	PBGA324
Ball Count	324
Ball Pitch (mm)	1
Die Size (mm)	7.5
Substrate Thickness (mm)	0.3
Substrate Pad	SMD
Ball Diameter (mm)	0.65

DIC velocity data at four corner locations of package on PCB side of speckle coated board is measured. DIC has been used to extract displacement and velocity along with full field strain contours on speckle pattern coated PCB. These velocity drive attachment degrees of freedom of PBC components of line spring as shown in Figure 89. Contour plot of full filed strain histories is measured on entire printed circuit board during complete drop event. Board is coated with speckle pattern similar to bimaterial specimens. Figure 90 shows high speed camera snapshots at different time intervals after board is dropped at 12,500g. As central region of the board undergoes maximum deflection, maximum strain is observed at this location during flexing.

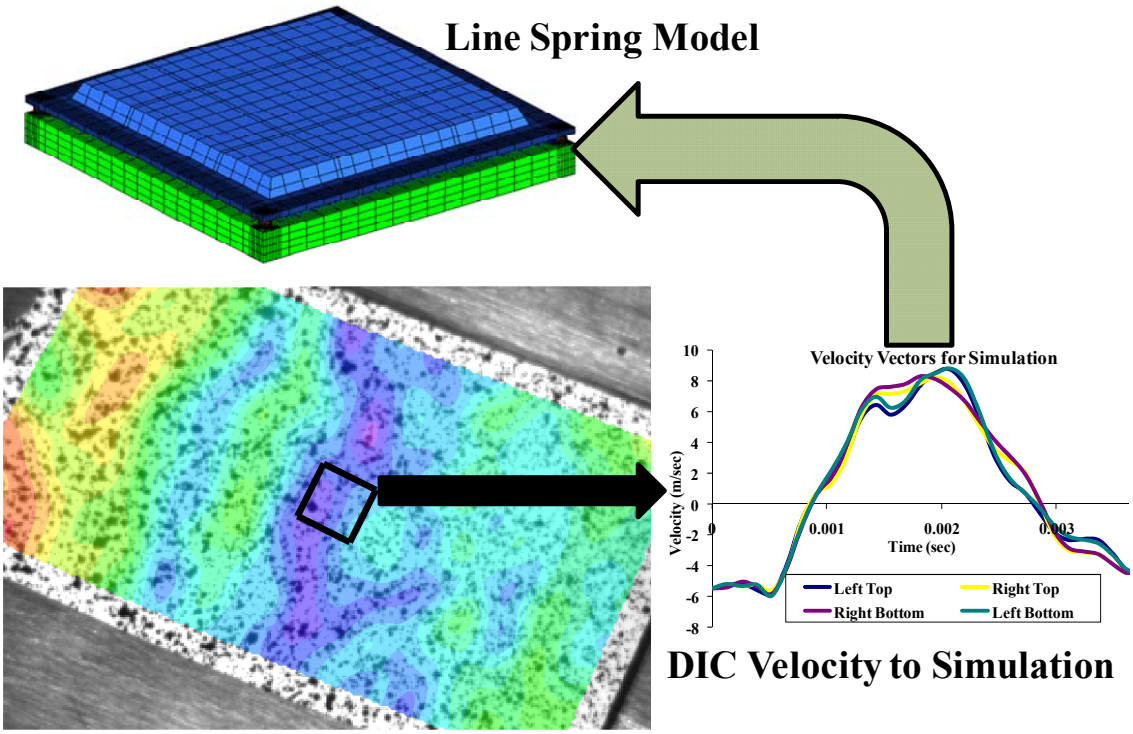

Figure 89: Methodology implemented for defining boundary conditions to FE Models

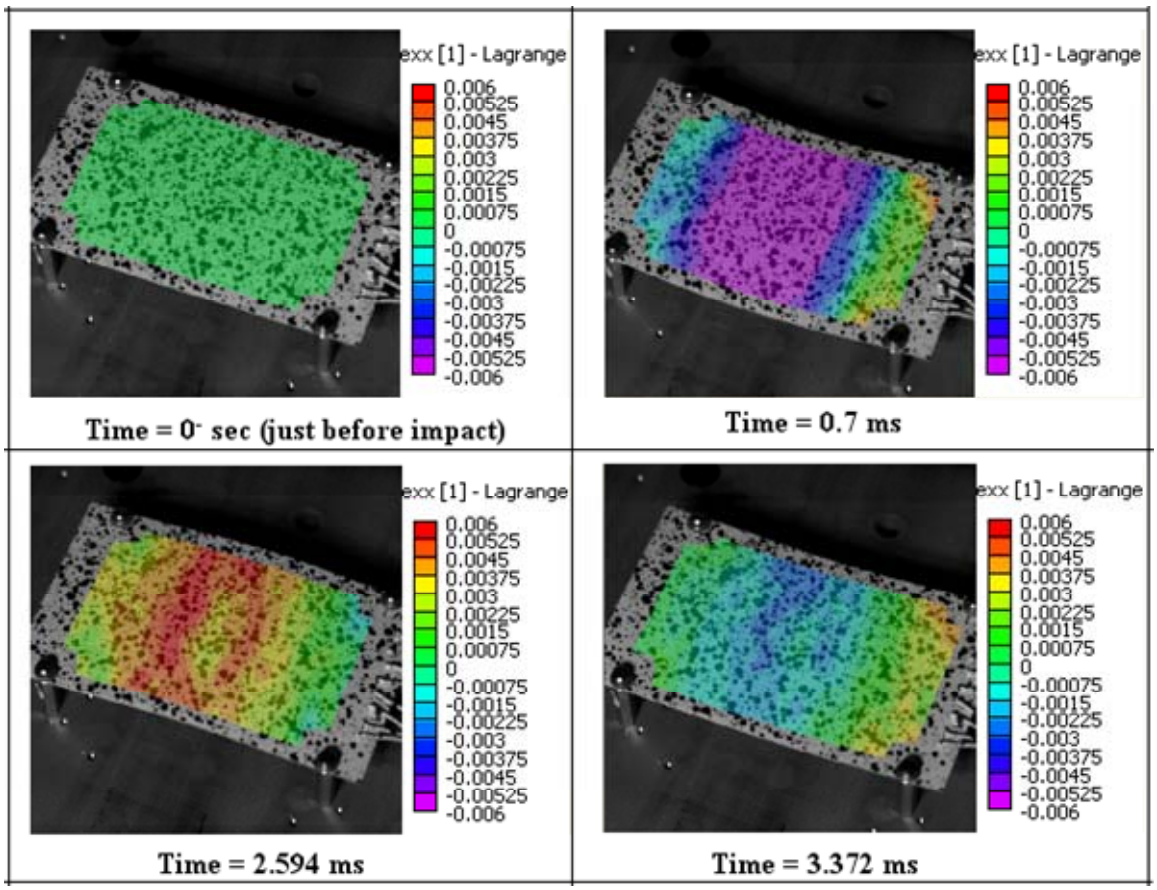

Figure 90: High speed camera snapshots of PCB showing full field strain distribution when dropped at high g loading

It has been shown previously that bulk solder crack at the interface is a predominant mode of failure for printed circuit board assemblies under drop environment [Lall 2010[a]]. Therefore line spring elements LS6 are inserted in this region of a critical solder interconnect at most critical region. Figure 92 explains the procedures implemented in order to identify the most critical region on critical solder interconnect.

Transient dynamic behavior of this centrally located package is simulated for 6ms at high loading of 12,500g. Global model is created with smeared packages mounted on PCB. In this explicit analysis, critical high stress region is identified as four corners of the package. To carry out detailed investigation of this critical region, submodels are created

with all four corner solder interconnects as spherical solder balls. Remaining 320 interconnects are modeled as Timoshenko beam elements. B31 beam element has six degrees of freedom including three rotational and three translational dof. Rotational degrees of freedom have been constrained to model the interconnect behavior of the beam elements. This explicit model is given experimental boundary conditions as explained earlier. Corner solder joint with maximum stress if found as shown in Figure 91 and modified as enrichment domain for XFEM analysis.

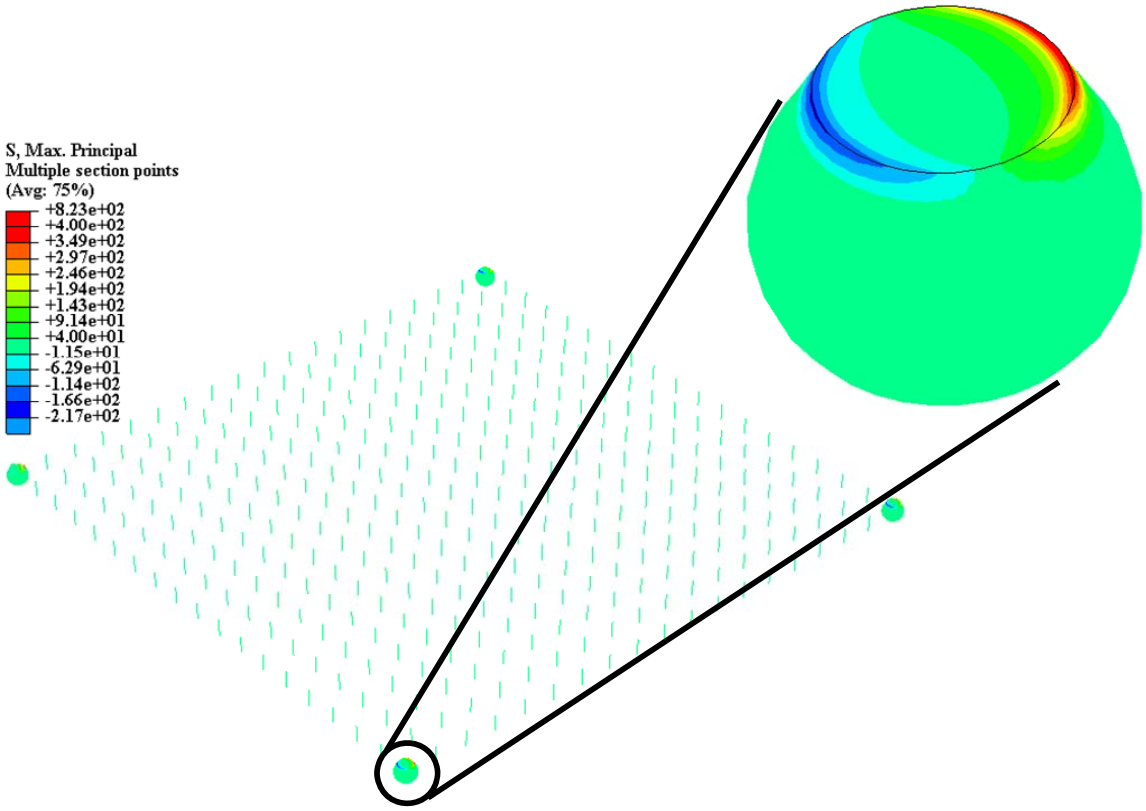

Figure 91: Maximum principle stress distribution in PBGA324 interconnect with Sn1Ag0.5Cu alloy dropped at 12,500 g

In XFEM analysis entire solder region of this corner interconnects is modeled with enriched degrees of freedom. This enrichment domain creates solution dependent region for XFEM analysis. Damage thresholds derived from high strain tests are used to

build constitutive damage model for quasi-static analysis. Damage behavior of this model is governed by traction separation law. When maximum principal stress criterion is met, crack nucleates at the critical location and travels to the adjacent elements. This critical location is recorded and used at flaw region for Line Spring models.

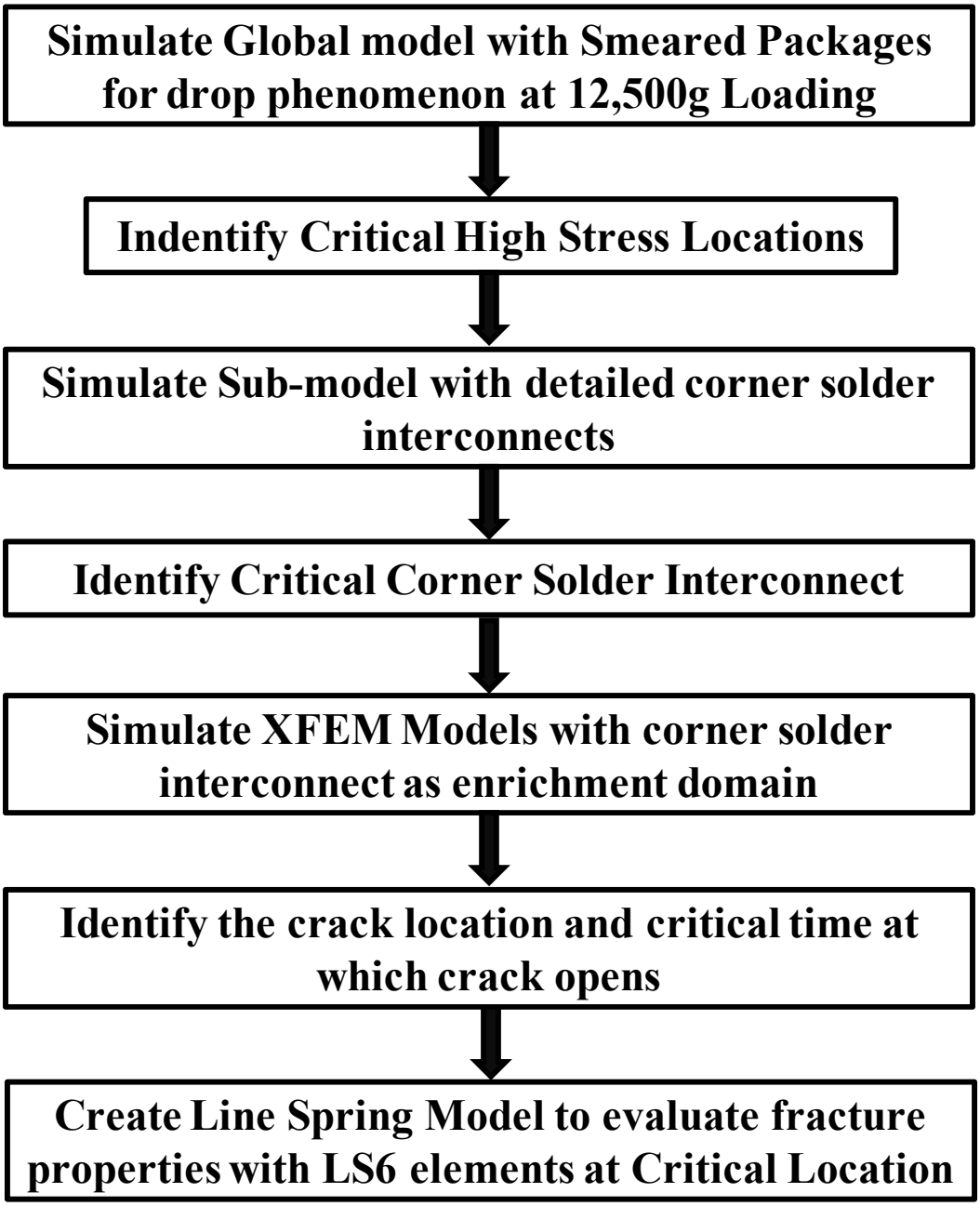

Figure 92: Flowchart of the procedures followed to evaluate fracture properties of most critical region in solder joints of BGA under mechanical shock

In quasi-static analysis of Line Spring model second order elements are used to model all the components of sub-model. Figure 93 shows this 2nd order sub-model for

PBGA324 package on the test board. Four corner interconnects are modeled in detail as spherical solder ball with copper pad. Remaining interconnects are modeled with beam B1 elements.

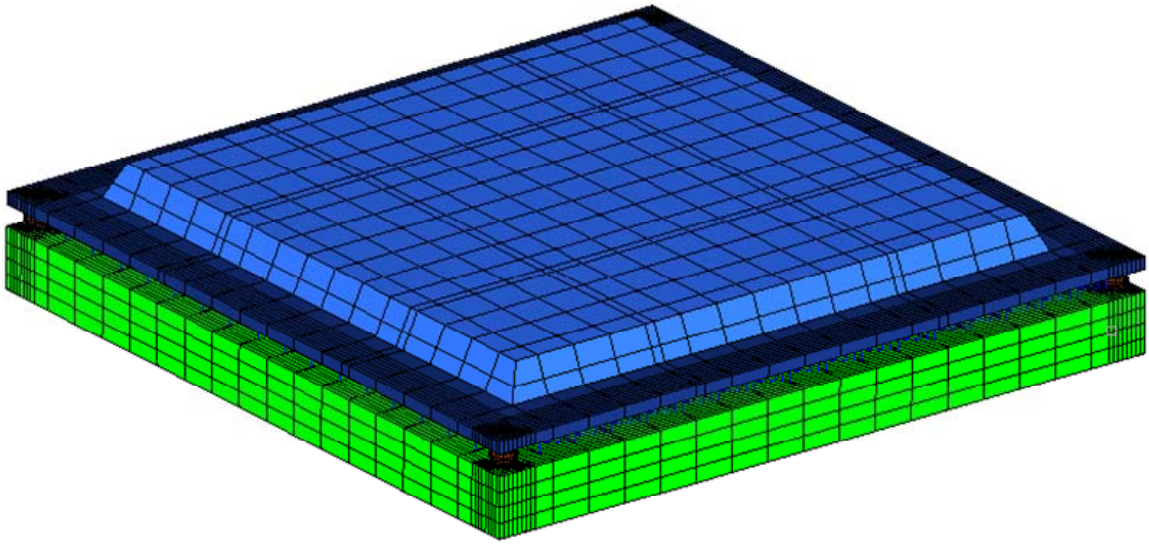

Figure 93: Second order FE model for PBGA324 with line spring elements

All remaining package components such as mold, substrate, PCB, copper pad, bulk solder region of corner interconnects are modeled with 20 node C3D20 solid elements. Cut section view of the package is shown in Figure 94.

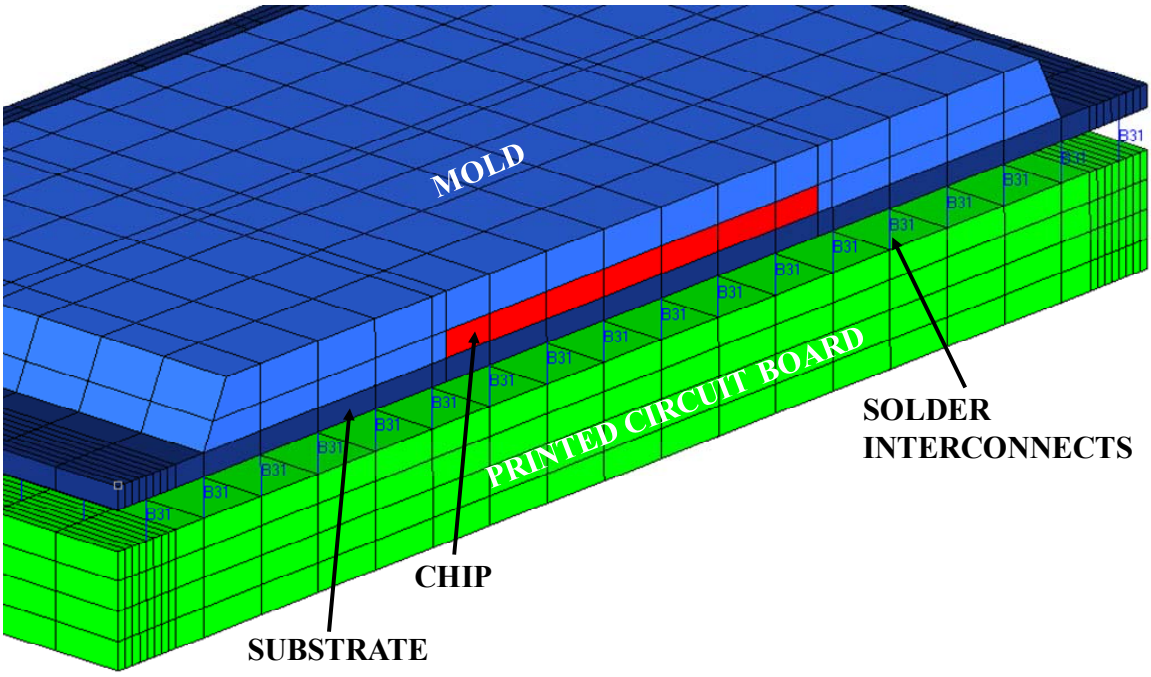

Figure 94: Cut section view of FE model for PBGA324 showing solder interconnects as B31 beam elements

Figure 95 and Figure 96 shows the detailed view of critical region where LS6 elements are inserted. Remaining region of this layer of solder is modeled with small Timoshenko beams with solder properties. Line spring elements are modeled adjacent to 2D shell elements with element type S8R. This 2D shell element and line spring elements are given properties of solder material. Experimentally observed crack thickness is assigned as surface flaw for line spring element.

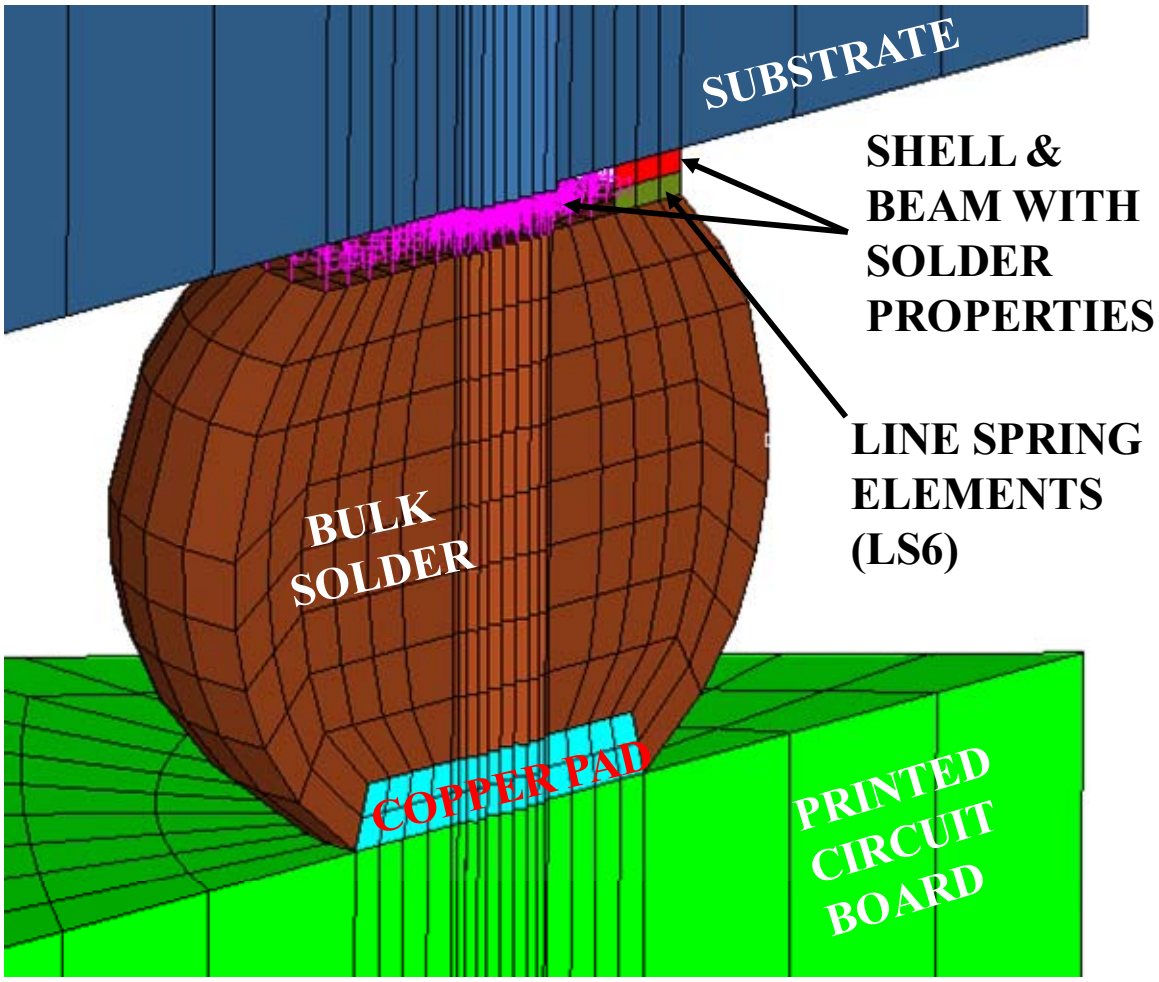

Figure 95: Section view of a critical interconnect showing location of line spring LS6 elements in Line Spring model

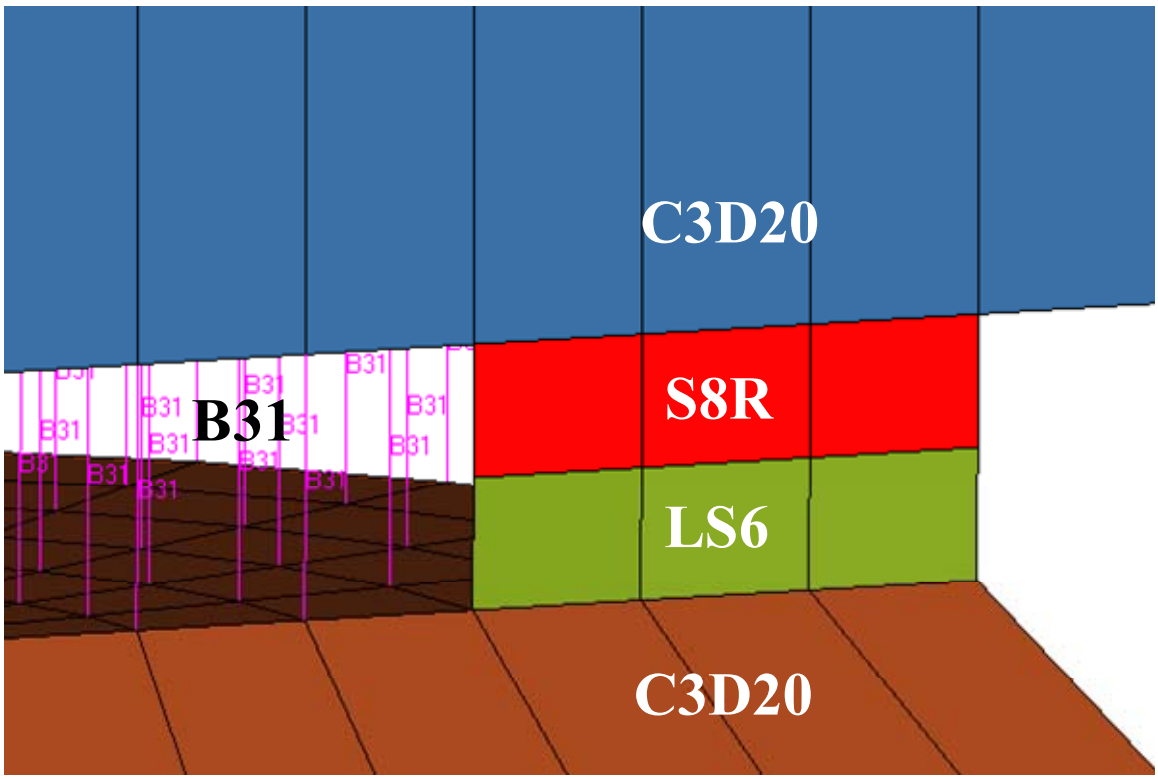

Figure 96: Zoomed-In view of interface showing LS6 line spring and other element types

A 12,500 g mechanical shock in JEDEC configuration was simulated. High stresses are observed in the corner solder joints. Models are simulated for a total of 6ms after the impact in order to capture first few high amplitude peaks of displacement. Stress contours in the solder interconnect is shown in Figure 97. It shows maximum principal stress distribution in critical solder interconnect at critical location at different time intervals after the impact of the test board on a drop table. As expected from XFEM prediction it can be seen that stresses are higher in the interface region and goes on increasing at different time interval after the impact. Total area of small beam elements added together accounts for the area of solder layer at the interface. Failure of solder interconnect is caused due to flexing of the board during drop event. Corner solder interconnect undergoes maximum tensile loading state. As tensile loading is predominant

cause of failure, opening mode stress intensity factor is investigated at critical failure location. Opening mode (Mode 1) SIF variation with respect to time under simulated condition is shown in figure Figure 98. SIF contours on line spring LS6 elements shows maximum value of K_I at crack initiation location predicted using XFEM analysis. It can be seen that K_I goes on increasing from periphery towards the center of interconnect. It indicated that the damage starts at periphery and this crack travels towards center of solder joint. Figure 99 shows stress intensity factor plotted against time. It can be seen that SIF crosses the critical value evaluated by high strain rate tensile testing of bimaterial specimen. This bimaterial specimen has been tested at strain rate of $55s^{-1}$. This critical SIF is reached when package is dropped at 12,500g loading. Figure 100 shows time varying J integral contours of line spring elements at different time intervals after the impact. J integral contours also indicate the trend of damage progression from periphery towards center of the solder.

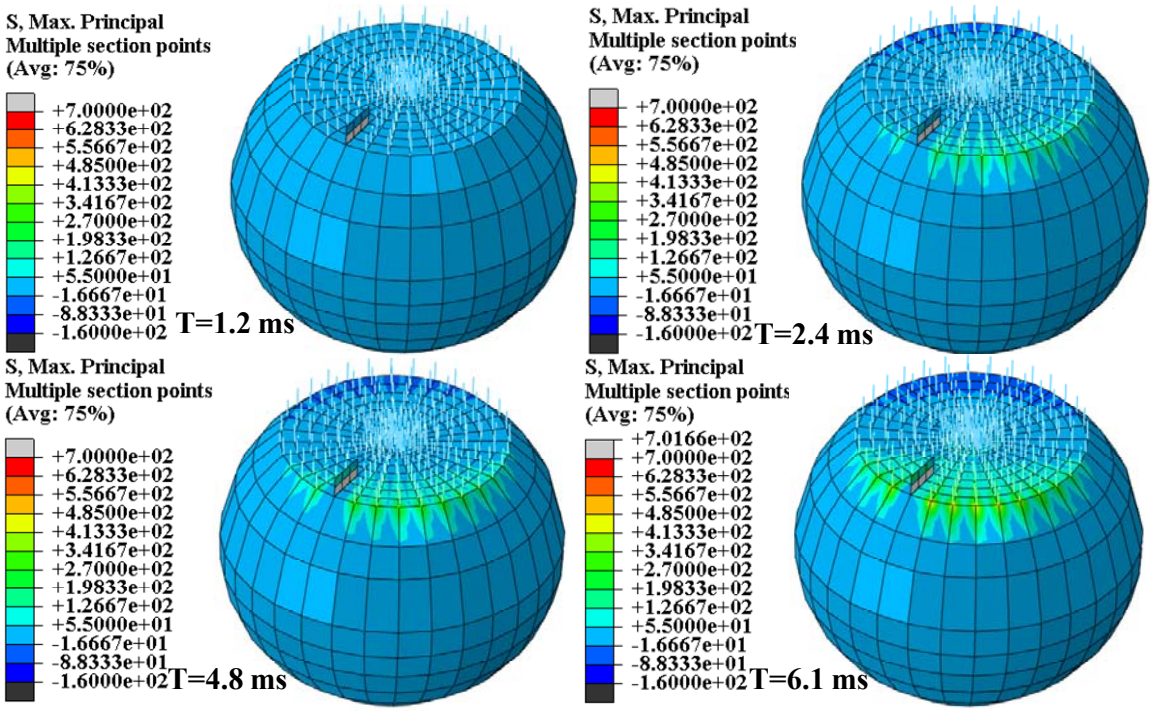

Figure 97: Maximum principle stress contours at critical solder location at different time interval after the impact

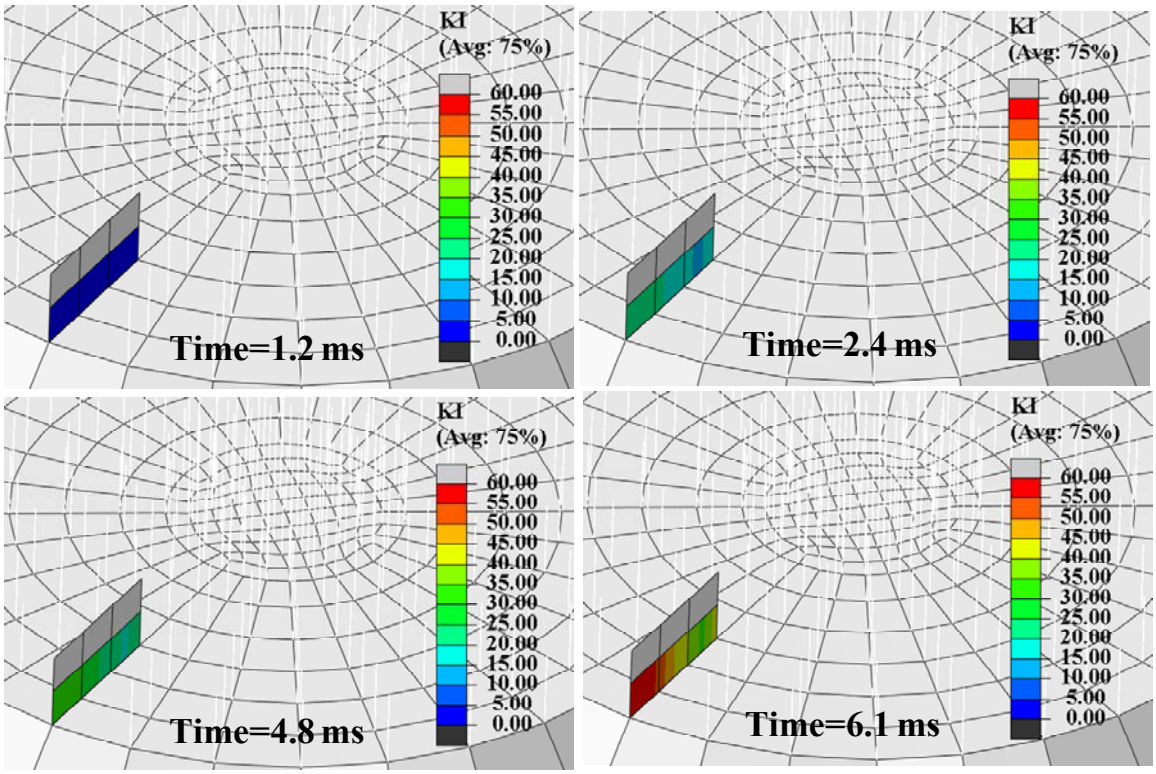

Figure 98: Stress intensity factor in $N/(mm\sqrt{mm})$ in contours in line spring elements at different time intervals after the impact at critical failure location

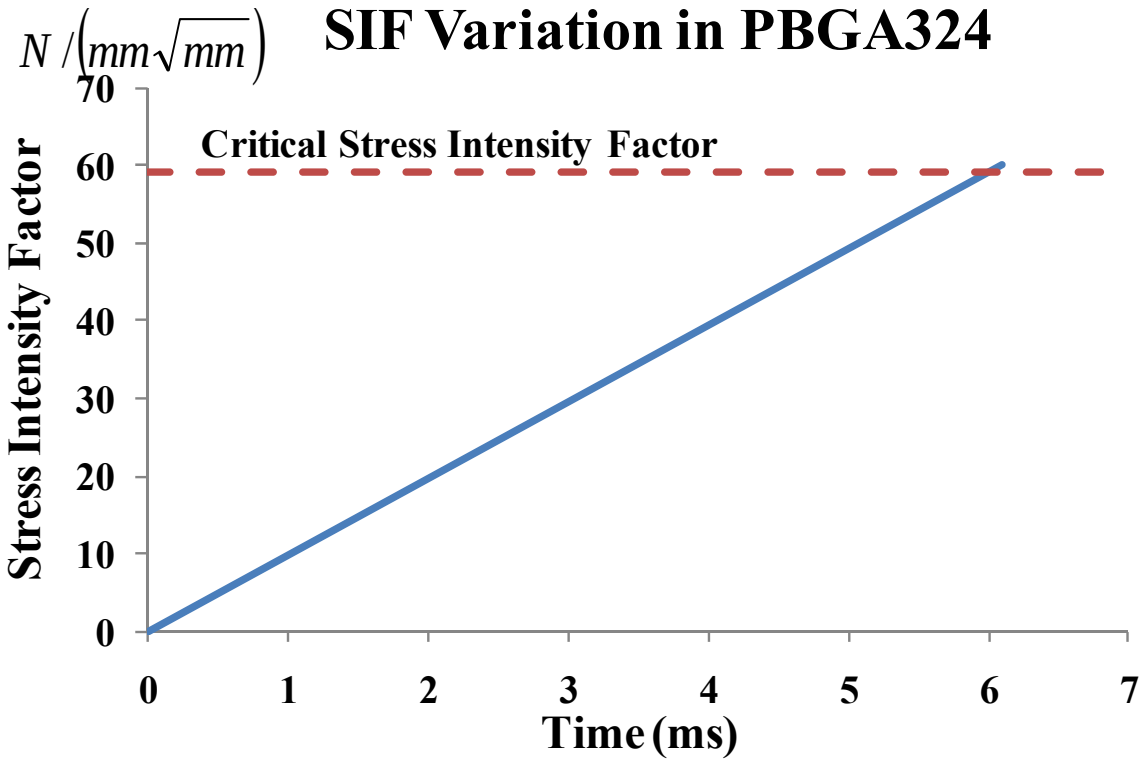

Figure 99: SIF variation for PBGA234 package with Sn1Ag0.5Cu alloy

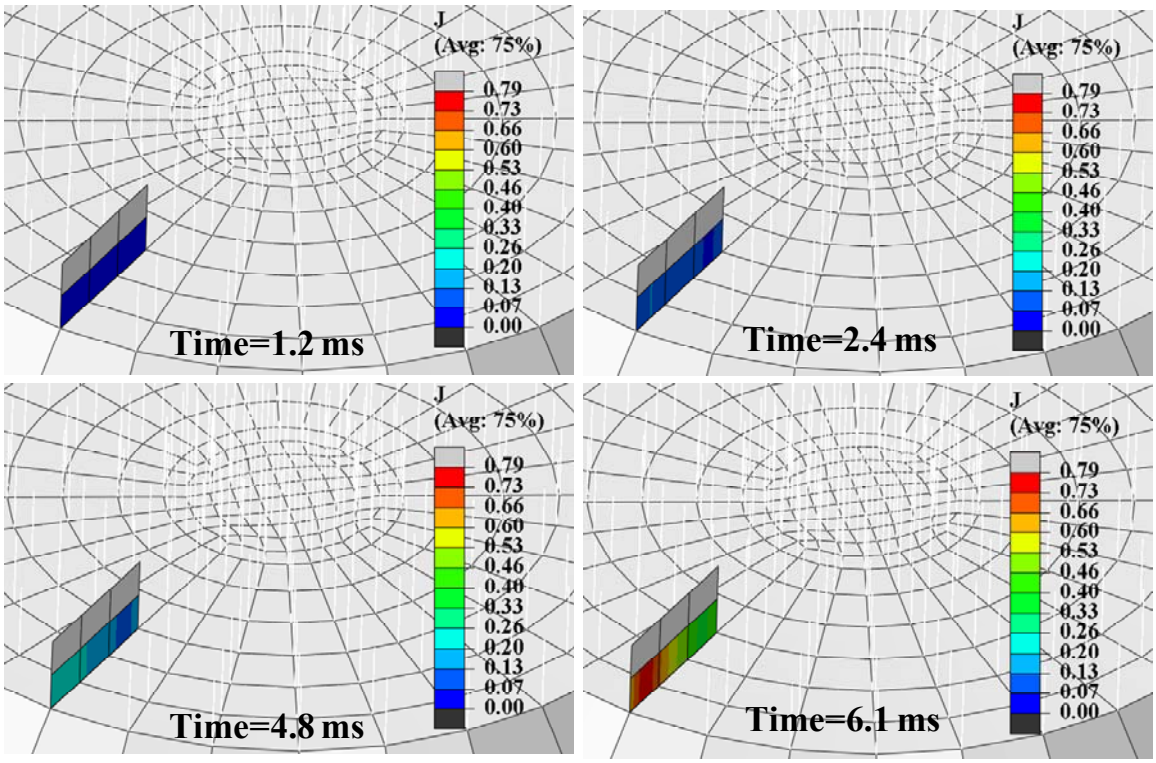

Figure 100: J integral contours in line spring elements at different time intervals after the impact at critical failure location

CHAPTER 6

SUMMARY AND FUTURE WORK

6.1 Reliability Models for Pb-free alloys and Advanced Interconnects

In this work, extended finite element has been used with explicit time integration for transient dynamic reliability prediction of electronic under 1500g and 12,500g shock loads. Several interconnect structures have been studied including Sn3Ag0.5Cu, Cu-reinforced Column, 63Sn37Pb, 90Pb10Sn on Ceramic ball grid array and plastic ball grid array devices. Interface fracture strength for the copper solder interface has been measured from high-strain rate tests of the bi-material specimen. XFEM model predictions based on measured values of interface strength have been correlated for all the interconnect technologies studied. The model predictions correlate well with the observed failure modes.

Using line spring technique critical stress intensity factors have been evaluated based on extended finite element method. Evaluated properties are correlated with experimentally determined SIF values. Crack nucleation and propagation in single and double notched bimaterial specimen has been studied experimentally and analytically. Simulation strain vectors at crack tip and away from crack tip have been correlated with strain extracted using ultra high speed imaging technique. Along with strain contour correlation for bimaterial specimens, strong statistical agreement between experimental

and FE results has been presented. A new approach to address high strain rate events is explained which allows material characterization of leadfree solder alloys over range of strain rates. Method for fabrication of bimaterial copper-solder specimen is described which allows preparation of homogenous test samples with no void formation. In case of ball grid arrays, critical solder interconnect which is located using extended finite element method is simulated for line spring analysis. A technique for determination of fracture properties in this critical solder interconnect is developed using line spring method at high g shock loads.

6.2 Scope for Future Work

Linear elastic finite element models are simulated in this current work. It would be interesting to built material models which are nonlinear in nature. Constitutive models which are elastic-plastic or viscoplastic in behavior can be used to define solder alloy in FE models of drop and tensile tests. New crack propagation techniques similar to extended finite element method, cohesive zone method and line spring method can be implemented to address the issues of bulk solder crack and IMC cracks.

Other failure modes observed in failure of electronics such as pad cratering, chip delamination, underfill cracking, material fracture in capacitors, resisters, lead fracture can be analyzed using these crack propagation techniques XFEM and CZM to find out critical failure region. Cohesive zone modeling can be used to asses the thermomechanical reliability of BGA interconnects also.

Extended finite element analysis presented in this thesis addresses the event as quasistatic dynamic event. It would be a valuable study to carry out explicit dynamic

analysis of leadfree interconnects under drop and shock conditions. Strains fields measured from these global models and submodels can be used in life prediction models based on various higher order learning algorithms.

BIBLIOGRAPHY

Abaqus 6.9-1 Documentation, Section 28.5.3: Modeling with cohesive elements, 2009a.

Abaqus 6.9-1 Documentation, Section 10.6.1: Modeling discontinuities as an enriched feature using the extended finite element method, 2009b.

Abaqus 6.9-1 Documentation, Section 29.10.1: Line spring elements for modeling part-through cracks in shells, 2009c.

Abaqus 6.9-1 Documentation, Section 19.2.1: Classical Metal Plasticity, 2009d.

Abdelaziz, Y., Hamouine, A., A survey of the extended finite element, Computers and Structures, Volume 86, Issues 11-12, June 2008, pp. 1141-1151.

Abdul-Baqi, A., Schreurs, P. J. G., Geers, M. G. D., Fatigue damage modeling in solder interconnects using a cohesive zone approach, International Journal of Solids and Structures, Volume 42, pp. 927-942, 2005.

Alam, M. O., Lu, H., Bailey, C., Chan, Y. C., Fracture Mechanics Analysis of Cracks in Solder Joint Intermetallic Compounds, 2nd Electronics Systemintegration Technology Conference, Greenwich UK, pp. 757 – 762, 2008.

Amodio, D., Broggiato, G., Campana, F., Newaz, G., Digital Speckle Correlation for Strain Measurement by Image Analysis, Experimental Mechanics, Vol. 43, No. 4, pp. 396-402, 2003.

Anderson, T. L., Fracture Mechanics – Fundamentals and Applications, CRC Press, Taylor and Francis Group, 2005

Araki, W., Nemoto, K., Adachi, T., Yamaji, A., Fracture toughness for mixed mode I/II of epoxy resin. Acta Mater, Volume 53, pp. 869–75, 2005.

Belytschko, T., Black, T., Elastic crack growth in finite elements with minimal remeshing, International Journal for Numerical Methods in Engineering Volume 45 Issue 5, pp. 601-620, April 1999.

Benzeggagh, M. L., Kenane, M., Measurement of mixed-mode delamination fracture toughness of unidirectional glass/epoxy composites with mixed-mode bending apparatus, Compos Sci Technol, Volume 56, pp. 439–49, 1996.

Board Level Drop Test Method of Components for Handheld Electronic Products JESD22-B111.

Cirak, F., Deiterding, R., Mauch, S.P., Large-scale fluid structure interaction simulation of viscoplastic and fracturing thin-shells subjected to shocks and detonations, Computers and Structures, Volume 85, Issues 11-14, June-July 2007, pp. 1049-1065.

Cote, K.J., Dadkhah, M.S., Whole field displacement measurement technique using speckle interferometry, Proceedings of the 51st Electronic Component and Technology Conference, pp. 80-84, 2001.

Dally, J., Lall, P., Suhling, J., Mechanical Design of Electronic Systems, Publisher: College House Enterprises, LLC, Number of Pages: 664, ISBN-10: 0976241331, ISBN-13: 978-0976241331, Copyright Year: 2008.

Daux, C., Moe¨ s, N., Dolbow, J., Sukumar, N., Belytschko, T., Arbitrary branched and intersecting cracks with the extended finite element method. Int. J. Numer. Methods Eng., Vol. 48, No. 12, pp. 1741–1760, 2000.

Dollhofer, J., Beckert, W., Lauke, B., Schneider, K., Fracture mechanical characterisation of mixed-mode toughness of thermoplast/glass interfaces, Comput Mater Sci, Volume 19, pp. 223–8, 2000.

Elices, M., Guinea, G.V., Gómez, J. and Planas, J., The cohesive zone model: advantages, limitations and challenges, Engng. Fract. Mech., 69, 137–163, 2002

Falk, M. L., Needleman, A., Rice, J. R., A critical evaluation of cohesive zone models of dynamic fracture. J Phys IV, Volume 11, pp. 43–52, 2001.

Giner, E., Sukumar, N., Tarancón, J. E., Fuenmayor, F. J., An Abaqus Implementation of the Extended Finite Element Method, Engineering Fracture Mechanics, Volume 76, Issue 3, February 2009, Pages 347-368.

Geubelle, P. H., Baylor, J. S., Impact-induced delamination of composites: a 2D simulation, Composites 29B (1998), pp. 589–602.

Gonalves, J. P. M., de Castro, P. M. S. T., Application of the line spring model to some complex geometries, and comparison with three-dimensional results, International Journal of Pressure Vessels and Piping, Volume 76, Issue 8, pp. 551-560, 1999.

Gross, B., Srawley, J. E., Stress-Intensity Factors for Single-Edge-Notch Specimens in Bending or Combined Bending and Tension by Boundary Collocation of a Stress Function, Jan 1965.

Gu, J., Cooreman, S., et al., Full-Field Optical Measurement For Material Parameter Identification With Inverse Methods, WIT Transactions on The Built Environment, Vol. 85, 2006.

Helm, J., McNeill, S., Sutton, M., Improved Three- Dimensional Image Correlation For Surface Displacement Measurement, Society of Photo-Optical Instrumentation Engineers, Vol. 35, No. 7, pp. 1911-1920, July 1996.

Hettich, T., Hund, A., Ramm, E., Modeling of failure in composites by X-FEM and level sets within a multiscale framework, Computer Methods in Applied Mechanics and Engineering, Volume 197, Issue 5, pp 414-424, 2008.

Ho, H.M., Oh, K.E., Wong, E.H., Lim, T.B., Application of moire interferometry in electronics packaging, Proceedings of the Electronic Packaging Technology Conference, pp. 277 – 282, 1997.

Jin, H., Lu, W., Hong, S., Connelly, K., Fracture Behavior of Polyurethane Foams, Proceedings of the SEM Conference, Springfield, MA, June 4-6, 2007.

Kehoe, L., Lynch, P., Guénebaut, V., Measurement of Deformation and Strain in First Level C4 Interconnect and Stacked Die using Optical Digital Image Correlation, 56th ECTC, pp. 1874-1881, May 2006.

Lall, P. Panchagade, D., Liu, Y., Johnson, W., Suhling, J., Smeared Property Models for Shock-Impact Reliability of Area-Array Packages, ASME Journal of Electronic Packaging, Volume 129, pp. 373-381, December 2007[d].

Lall, P., Choudhary, P., Gupte, S., Health Monitoring for Damage Initiation and Progression during Mechanical Shock in Electronic Assemblies, 56th ECTC, San Diego, California, pp.85-94, May 30-June 2, 2006[a].

Lall, P., Choudhary, P., Gupte, S., Suhling, J., Health Monitoring for Damage Initiation and Progression during Mechanical Shock in Electronic Assemblies, IEEE Transactions on Components and Packaging Technologies, Vol. 31, No. 1, pp. 173-183, March 2008[a].

Lall, P., Choudhary, P., Gupte, S., Suhling, J., Hofmeister, J., Statistical Pattern Recognition and Built-In Reliability Test for Feature Extraction and Health Monitoring of Electronics under Shock Loads, 57th Electronics Components and Technology Conference, Reno, Nevada, pp. 1161-1178, May 30-June 1, 2007[a].

Lall, P., Gupta, P., Panchagade, D., Self-organized mapping of failure modes in portable electronics subjected to drop and shock, 60th ECTC, Las Vegas, NV, pp. 1195 – 1208, 2010[c].

Lall, P., Gupte, S., Choudhary, P., Suhling, J., Darveaux, R., Cohesive-Zone Explicit Sub-Modeling for Shock Life- Prediction in Electronics, 57th ECTC, pp. 515-527, Reno, NV, May 29- Jun 1, 2007[e].

Lall, P., Gupte, S., Choudhary, P., Suhling, J., Solder-Joint Reliability in Electronics Under Shock and Vibration using Explicit Finite Element Sub-modeling, IEEE Transactions on Electronic Packaging Manufacturing, Volume 30, No. 1, pp. 74-83, January 2007[b].

Lall, P., Gupte, S., Choudhary, P., Suhling, J., Solder-Joint Reliability in Electronics Under Shock and Vibration using Explicit Finite-Element Sub-modeling, 56th ECTC, pp. 428–435, 2006[b].

Lall, P., Hande, M., Bhat, C., Islam, N., Suhling, J., Lee, J., Feature Extraction and Damage-Precursors for Prognostication of Lead-Free Electronics, Microelectronics Reliability, Vol. 47, pp. 1907–1920, December 2007e.

Lall, P., Iyengar, D., Shantaram, S., Pandher, R., Panchagade, D., Suhling, J., Design Envelopes and Optical Feature Extraction Techniques for Survivability of SnAg Leadfree Packaging Architectures under Shock and Vibration, 58th ECTC, Orlando, FL, pp. 1036-1047, May 27-30, 2008[d].

Lall, P., Iyengar, D., Shantaram, S., S., Gupta, P., Panchagade, D., Suhling, J., KEYNOTE PRESENTATION: Feature Extraction and Health Monitoring using Image Correlation for Survivability of Leadfree Packaging under Shock and Vibration, EuroSIME, Freiburg, Germany, pp. 594-608, April 16-18, 2008[c].

Lall, P., Kulkarni, M., Angral, A., Panchagade, D., Suhling, J., Digital-Image Correlation and XFEM Based Shock-Reliability Models for Leadfree and Advanced Interconnects, Proceedings of the 60th ECTC, pp. 91-105, 2010[a].

Lall, P., Panchagade, D., Choudhary, P., Gupte, S., Suhling, J., Failure-Envelope Approach to Modeling Shock and Vibration Survivability of Electronic and MEMS Packaging, IEEE Transactions on Components and Packaging Technologies, Vol. 31, No. 1, pp. 104-113, March 2008[b].

Lall, P., Panchagade, D., Choudhary, P., Suhling, J., Gupte, S., Failure Envelope Approach to Modeling Shock and Vibration Survivability of Electronic and MEMS Packaging, 55th ECTC, pp. 480-490, 2005.

Lall, P., Panchagade, D., Iyengar, D., Shantaram, S., Suhling, J., Schrier, H., High Speed Digital Image Correlation for Transient-Shock Reliability of Electronics, 57th ECTC, Reno, Nevada, pp. 924-939, May 29 – June 1, 2007[c].

Lall, P., Panchagade, D., Liu, Y., Johnson, R. W., and Suhling, J. C., Smeared-Property Models for Shock-Impact Reliability of Area-Array Packages, Journal of Electronic Packaging, Vol. 129(4), pp. 373-381, 2007.

Lall, P., Panchagade, D., Liu, Y., Johnson, W., Suhling, J., Models for Reliability Prediction of Fine-Pitch BGAs and CSPs in Shock and Drop-Impact, 54th ECTC, pp. 1296-1303, 2004.

Lall, P., Shantaram, S., Kulkarni, M., Limaye, G., Suhling, J., Constitutive Behavior of SnAgCu Leadfree Alloys at High Strain Rates, Proceedings of ASME Pacific Rim Technical Conference and Exhibition on Packaging and Integration of Electronic and Photonic Systems, MEMS and NEMS, Portland, Oregon, 2011.

Lall, P., Shantaram, S., Panchagade, D., Peridynamic- odels using finite elements for shock and vibration reliability of leadfree electronics, 12th Intersociety Conference on Thermal and Thermomechanical Phenomena in Electronic Systems, Las Vegas, NV, pp. 1-12, 2010[b].

Lall, P., Shantaran, S., Angral, A., Kulkarni, M., Explicit Submodeling and Digital Image Correlation Based Life-Prediction of Leadfree Electronics under Shock-Impact, 59th ECTC, San Diego, CA, pp. 542-555, May 25-29, 2009.

Lall, P., Panchagade, D., Choudhary, P., Suhling, J., Gupte, S., "Failure-Envelope Approach to Modeling Shock and Vibration Survivability of Electronic and MEMS Packaging", Proceedings of the 55th Electronic Components and Technology Conference, pp. 522-529, 2005.

Landes, J. D., Begley, J. A., The Effect of Specimen Geometry on JIC, Fracture Toughness, Proceedings of 1971 National Symposium on Fracture Mechanics Part II, ASTM STP 514, American Society for Testing and Materials, pp. 24-39, 1971.

Lau, J. H., Ball Grid Array Technology, McGraw-Hill, Inc., 1995.

Lau, J.H., Chang, C., Lee, S. W. R., Solder joint crack propagation analysis of wafer-level chip scale package on printed circuit board assemblies, IEEE Transactions on Components and Packaging Technologies, Volume 24, Issue 2, pp. 285 – 292, 2002.

Lee, H. T., Chen, M. H., Jao, H. M., Liao, T. L., Influence of interfacial intermetallic compound on fracture behavior of solder joints, Materials Science and Engineering A, Volume 358, Issues 1-2, pp. 134-141, 2003.

Limaye, P., Vandevelde, B., Labie, R., Vandepitte, D., Verlinden, B., Influence of Intermetallic Properties on Reliability of Lead-Free Flip-Chip Solder Joints, IEEE Transactions on advanced packaging, Volume 31, Number 1, 2008.

Limtrakarn, W., Stress Analysis on Crack Tip Using Q8 and Adaptive Meshes, Thammasat International Journal of Science and Technology, Volume 10 (1), pp.19-24, 2005.

Limtrakarn, W., Yodsangkham, A., Namlaow, A., Dechaumphai, P., Determination of KI, KII and trajectory of initial crack by adaptive finite element method and photoelastic technique, Experimental Techniques, Volume 34, Issue 4, pp. 27-35, 2010.

Liu, S., Wang, X., Ma, B., Gan, Z., Zhang, H., Drop Test and Simulation of Portable Electronic Devices, International Conference on Electronic Packaging Technology, pp.701-704, June, 2005

Lu, H., Applications of digital speckle correlation to microscopic strain measurement and materials' property characterization, Journal of Electronic Packaging, Volume 120, Issue 3, 275-279, September 1998.

Lu, H., Yeh, C., Wyatt, K., Experimental evaluation of solder joint thermal strain in a CSP using digital speckle correlation, 1998 InterSociety Conference on Thermal Phenomena, pp. 241–245, 1998.

Luan, J., Tee, T. Y., "Novel Board Level Drop Test Simulation using Implicit Transient Analysis with Input-G Method", Proceedings of the 6th Electronic Packaging Technology Conference, pp. 671-677, 2004.

Miller, T., Schreier, H., Reu, P, High-speed DIC Data Analysis from a Shaking Camera System, Proceedings of the SEM Conference, Springfield, MA, June 4-6, 2007.

Needleman, A., A Continuum Model for Void Nucleation by Inclusion Debonding, Journal of Applied Mechanics, Volume 54, pp. 525-531, 1987.

Nie, X., Bhate, D., Chan, D., Chen, W., Subbarayan, G., Dutta, I., Rate-Dependent Behavior of Sn3.8Ag0.7Cu Solder Over Strain Rates of 10-6 to 102 s-1, Proceedings of the 11th Intersociety Conference on Thermal and Thermomechanical Phenomena in Electronic Systems (Itherm 2008), IEEE, Vol. 1-3, pp. 676-682, 2008.

Ong, K. C., Tan, V. B. C., Lim, C. T., Wong, E. H., Zhang, X. W., Dynamic Materials Testing and Modeling of Solder Interconnects, 54th ECTC, pp. 1075 – 1079, Volume 1, 2004.

Oswald, J., Gracie, R., Khare, R., Belytschko, T., An extended finite element method for dislocations in complex geometries: Thin films and nanotubes, Computer Methods in Applied Mechanics and Engineering, Volume 198, Issues 21-26, 1 May 2009, pp. 1872-1886.

Pang, J. H. L., Xiong, B. S., Neo, C. C., Zhang, X. R., Low, T. H., Bulk Solder and Solder Joint Properties for Lead Free 95.5Sn-3.8Ag-0.7Cu Solder Alloy, 53rd Electronic Components and Technology Conference, pp. 673-679, 2003.

Pang, H. L. J., Mixed mode fracture analysis and toughness of adhesive joints, Engng Fract Mech, Volume 51, pp. 575–83, 1995.

Park, S., Al-Yafawi, A., Yu, D., Kwak, J., Lee, J., Goo, N., Influence of Fastening Methods on the Dynamic Response and Reliability Assessment of PCBS in Cellular Phones Under Free Drop, Proceedings of the ITherm, Intersociety Conference on Thermal and Thermo-mechanical Phenomena, Orlando, Florida, pp.876-882, May 28-May31, 2008.

Park, S., Reichman, A., Kwak, J., Chung, S., Whole Field Analysis of Polymer Film, Proceedings of the SEM Conference, Springfield, Massachusetts, June 4-6, 2007[b].

Park, S., Shah, C., Kwak, J., Jang, C., Pitarresi, J., Transient Dynamic Simulation and Full-Field Test Validation for A Slim-PCB of Mobile Phone under Drop Impact, Proceedings of the 57th ECTC, Reno, Nevada, pp. 914 - 923, May 29 – June 1, 2007[a].

PCB Piezotronics, Introduction to Piezoelectric Force Sensors, http://www.pcb.com/techsupport/, 2009

Petrov, V., Real Time Day Light Holography, Holographic Interferometry and Speckle Photography Well Suited To Medical Enviroment, Lasers and Electro-optics Europe, 1996. CLEO/Europe, pp. 326 –326, Sept 8-13, 1996.

Pratt, R. E., Stromswold, E. I., Quesnel, D. J., Mode I fracture toughness testing of eutectic Sn-Pb solder joints, Journal of Electronic Materials, Volume 23, Number 4, pp. 375-381, 1994.

Rahulkumar, P., Jagota, A., Bennison, S. J., Saigal, S., Cohesive element modeling of viscoelastic fracture: application to peel testing of polymers, Int J Solids Struct, Volume 37, pp. 1873–97, 2000.

Remmers, J. J. C., R. de Borst, Needleman, A. , The Simulation of Dynamic Crack Propagation using the Cohesive Segments Method, Journal of the Mechanics and Physics of Solids, vol. 56, pp. 70–92, 2008.

Rice, J. R., Levy, N., The part-through surface crack in an elastic plate, Journal of Applied Mechanics, Volume 39, pp. 185–194, 1972[b].

Rice, J. R., Some Remarks on Elastic crack-tip stress fields, International Journal of Solids Structures, Volume 8, pp. 751-758, 1972[c].

Rice, J. R., The Line Spring Model for Surface Flaws, The Surface Crack: Physical Problems and Computational Solutions, J. L. Sedlow, Editor, ASME, 1972[a].

Seah, S.K.W., Lim, C.T.,Wong, E.H., Tan, V.B.C., Shim, V.P.W., Mechanical Response of PCBs in Portable Electronic Products During Drop Test, Electronic Packaging Technology Conference, pp. 120-125, May, 2002.

Smith, E. W., North, H., Sunlight speckle photography, Holographic Systems, Components and Applications, Fourth International Conference, pp. :232 – 236, 13-15 Sep 1993.

Song, J. H., P. M. A. Areias, and T. Belytschko, A Method for Dynamic Crack and Shear Band Propagation with Phantom Nodes, International Journal for Numerical Methods in Engineering, Vol. 67, pp. 868–893, 2006.

Srinivasan, V., Radhakrishnan, S., Zhang, X., Subbarayan, G., Baughn, T., Nguyen, L., High Resolution Characterization of Materials Used In Packages through Digital Image Correlation, ASME InterPACK, July 17-22, 2005.

Suha, D., Kimb, D. W., Liu, P., Kima, H., Weninger, J. A., Kumara, C. M., Prasad, A., Grimsley, B, W., Tejada, H. B., Effects of Ag content on fracture resistance of Sn–Ag–Cu lead-free solders under high-strain rate conditions, Materials Science and Engineering: A, Volumes 460-461, pp. 595-603, 2007.

Sukumar, N., Srolovitz, D.J., Baker, T.J., Prévost, J.H., Brittle fracture in polycrystalline microstructures with the extended finite element method, International Journal for Numerical Methods in Engineering, February 2003, Volume 56, Issue 14, pp. 2015-2037.

Sun, Y., Pang, J., Shi, X., Tew, J., Thermal Deformation Measurement by Digital Image Correlation Method, Intersociety Conference on Thermal and Thermomechanical Phenomena in Electronics Systems, pp. 921-927, May 2006.

Sun, X.S., Tan, V.B.C., Liu, G., Tay, T.E., An enriched element-failure method (REFM) for delamination analysis of composite structures, International Journal for Numerical Methods in Engineering, February 2009, Volume 79, Issue 6, pp. 639-666.

Tada, H., C. Paris, and G. R. Irwin, The Stress Analysis of Cracks Handbook, Del Research Corporation, Hellertown, Pennsylvania, 1973.

Tee, T. Y., Ng, H. S., Lim, C. T., Pek, E., Zhong, Z., Board Level Drop Test and Simulation of TFBGA Packages for Telecommunication Applications, Proceedings of the 53rd ECTC, pp. 121-129, 2003.

Thompson, R. J., Hemker, K. J., Thermal Expansion Measurements on Coating Materials by Digital Image Correlation, Proceedings of the SEM Conference, Springfield, Massachusetts, June 4-6, 2007.

Thurner, P., Erickson, B., Schriock, Z., High-Speed Photography of Human Trabecular Bone during Compression, Materials Research Society Symposium Proceedings, Vol 874, 2005.

Unger, J. F., Eckardt, S., Könke, C., Modeling of cohesive crack growth in concrete structures with the extended finite element method, Computer Methods in Applied Mechanics and Engineering, Volume 196, Issues 41-44, pp 4087-4100, September 2007.

Van den Bosch, M. J., Schreurs, P. J. G., Geers, M. G. D., An improved description of the exponential Xu and Needleman cohesive zone law for mixed-mode decohesion. Engng Fract Mech 2006;73(9):1220-34.

Wang, G., Zhao, J., Ding, M., Ho, P.S., Thermal deformation analysis on flip-chip packages using high resolution moiré interferometry, The Eighth Intersociety Conference of Thermal and Thermo-mechanical Phenomena in Electronic Systems, pp. 869 – 875, 30 May-1 June 2002.

Warrior, N. A., Pickett, A. K., Lourenco, N. S. F., Mixed-mode delamination-experimental and numerical studies, Strain 2003, Volume 39, pp.153–9, 2003.

Watanabe, K., Koseki, J., Tateyama, M., Application of High- Speed Digital CCD Cameras to Observe Static and Dynamic Deformation Characteristics of Sand, Geotechnical Testing Journal, Vol. 28, No. 5, 2005.

Williams, M. L., On the Stress Distribution at the Base of a Stationary Crack, Journal of Applied Mechanics, Volume 24, pp. 109-114, 1957.

Wong, E. H., Lim, C. T., Field, J. E., Tan, V. B. C., Shim, V. P. M., Lim, K. T., Seah, S. K. W., Tackling the Drop Impact Reliability of Electronic Packaging, ASME InterPACK, July 6 -11, Maui, pp. 1 – 9, 2003.

Woodgate Ralph. ―Solder Joint Inspection Criteria, Printed Circuit Assembly, pp-6-10, February 1987,

Xu, L., Tan, K. E., Pang, J. H. L., Strain-rate-dependant mechanical properties for Sn-3.8Ag-0.7Cu and SAC-X solder alloy, 11th ITHERM, Orlando, FL, pp. 632 – 637, 2008.

Yang, Q. D., Thouless, M. D0, Ward, S. M., Elastic–plastic mode-II fracture of adhesive joints, Int J Solids Struct, Volume 38, pp.3251–62, 2001.

Yeh, C., Lai, Y., Transient Analysis of Board-level Drop Response of Lead-free Chipscale Packages with Experimental Verifications, Electronic Components and Technology Conference, pp. 695-700, June, 2004.

Yogel, D., Grosser, V., Schubert, A., Michel, B., MicroDAC Strain Measurement for Electronics Packaging Structures, Optics and Lasers in Eng., Vol. 36, pp. 195-211, 2001.

Yuan, H., Chen, J., Computational analysis of thin coating layer failure using a cohesive zone model and gradient plasticity, Engng Fract Mech, Volume 70, pp. 1929–42, 2003.

Zhang, D., Zhang, X., Cheng, G., Compression strain measurement by digital speckle correlation, Experimental Mechanics, Vol. 39, No. 1, March, 1999, pp. 62-65.

Zhang, Q., Dasgupta, A., Haswell, P., Partitioned Viscoplastic-Constitutive Properties of the Pb-Free Sn3.9Ag0.6Cu Solder, Journal of Electronic Materials, Volume 33, Number 11, 2004.

Zhang, Y., Shi, X., Zhou, W., Effect of Hygrothermal Aging on Interfacial Reliability of Flip Chip on Board (FCOB) Assembly, Electronic Packaging Technology Conference, pp. 404-409, 2004a.

Zhang, F., Li, M., Xiong, C., Fang, F., Yi, S., Thermal Deformation Analysis of BGA Package by Digital Image Correlation Technique, Microelectronics International, Vol. 22, No. 1, pp. 34-42, 2005.

Zhao, J., Mutohb, Y., Miyashitab, Y., Wang, L., Fatigue crack growth behavior of Sn–Pb and Sn-based lead-free solders, Engineering Fracture Mechanics, Volume 70, Issue 15, pp. 2187-2197, 2003.

Zhou, P., Goodson, K. E., Sub-pixel Displacement and Deformation Gradient Measurement Using Digital Image-Speckle Correlation (DISC), Optical Engineering, Vol. 40, No. 8, pp 1613-1620, August 2001.

Zhu, L., Marccinkiewicz, W., Drop Impact Reliablity Analysis of CSP Packages at Board and Product System Levels Through Modeling Approaches, Proceedings of the ITherm Conference, pp. 296 – 303, 2004.

Zhu, L., Modeling Technique for Reliability Assessment of Portable Electronic Product Subjected to Drop Impact Loads, Proceedings of the 53rd ECTC, pp. 100-104, 2003.